

# **Climatology of extreme rainfall from rain gauges and weather radar**

**Aart Overeem**

### **Thesis committee**

#### **Thesis supervisor**

Prof. dr. ir. R. Uijlenhoet

Professor of Hydrology and Quantitative Water Management  
Wageningen University, the Netherlands

#### **Thesis co-supervisors**

Dr. I. Holleman

Senior Scientist, KNMI, De Bilt, the Netherlands

Dr. T. A. Buishand

Senior Scientist, KNMI, De Bilt, the Netherlands

#### **Other members**

Prof. dr. A. A. M. Holtslag, Wageningen University, the Netherlands

Prof. dr. ir. M. F. P. Bierkens, Utrecht University, the Netherlands

Prof. C. G. Collier, University of Leeds, United Kingdom

Prof. C. W. Anderson, University of Sheffield, United Kingdom

This research was conducted under the auspices of the SENSE Research School.

# **Climatology of extreme rainfall from rain gauges and weather radar**

**Aart Overeem**

## **Thesis**

submitted in partial fulfilment of the requirements for the degree of doctor  
at Wageningen University  
by the authority of the Rector Magnificus  
Prof. dr. M. J. Kropff,  
in the presence of the  
Thesis Committee appointed by the Doctorate Board  
to be defended in public  
on Friday 4 December 2009  
at 1:30 PM in the Aula

Aart Overeem

Climatology of extreme rainfall from rain gauges and weather radar, xii+132 pages.

In Dutch: Klimatologie van extreme neerslag uit regenmeters en weerradar, xii+132 blz.

Thesis Wageningen University, Wageningen, NL (2009)

With references, with summaries in Dutch and English

ISBN 978-90-8585-517-0



Extreme rainfall events can have a large impact on society and can lead to loss of life and property. Therefore, a reliable climatology of extreme rainfall is of importance, for instance, for the design of hydraulic structures. Such a climatology can be obtained by abstracting maxima from long rainfall records. Subsequently, a probability distribution is fitted to the selected maxima, so that rainfall depths can be estimated for a chosen return period, which can be longer than the rainfall record. In this thesis, the Generalized Extreme Value (GEV) distribution is used to model annual rainfall maxima.

Using a new methodology, rain gauge data from 12 stations in the Netherlands are employed to derive rainfall depth-duration-frequency (DDF) curves, which describe rainfall depth as a function of duration for given return periods. Often, uncertainties are not incorporated in the design of hydraulic structures, which can lead to a risk of under design. Therefore, uncertainties in the DDF curves are estimated as well.

Weather radars are widely used in real-time quantitative precipitation estimation over large areas with high temporal and spatial resolutions not achieved by conventional rain gauge networks. A 10-year radar-based climatology of rainfall depths for durations of 15 min to 24 h is derived for the Netherlands. Since radar data can be vulnerable to a number of errors, they are adjusted using rain gauges. Verification shows that the radar data set has a high quality.

In general, only few digitized time series from rain gauges are available for subdaily durations. This hampers the study of regional variability in extreme rainfall and the estimation of extreme areal rainfall, which can be overcome by using weather radar. The climatological radar rainfall data set is utilized to obtain annual rainfall maxima for durations of 15 min to 24 h and the size of a radar pixel. GEV distributions are fitted to these annual maxima. For most durations, significant regional differences in extreme rainfall in the Netherlands are found. Subsequently, rainfall DDF curves are constructed. The radar-based extreme rainfall statistics are in good agreement with those obtained from rain gauges, although an underestimation is found for short durations. The uncertainties in radar-based DDF curves are small for short durations and become rather large for long durations.

Employing the climatological radar data set, annual maxima are obtained for area sizes ranging from a radar pixel to approximately 1700 km<sup>2</sup>. A single equation is derived from which rainfall depths for a chosen return period and area size can be calculated for different durations: the areal DDF curve. Extreme areal rainfall statistics based on rain gauge data agree well with those derived from radar data.

The main result of this thesis is that, after adjustment with rain gauges, weather radar data can be used to derive a climatology of extreme (areal) rainfall including the uncertainties and can be used to study regional differences in extreme rainfall.

# Samenvatting

Extreme neerslaggebeurtenissen hebben een grote invloed op de maatschappij en kunnen leiden tot materiële schade en slachtoffers. Daarom is een betrouwbare klimatologie van extreme neerslag belangrijk, bijvoorbeeld voor het ontwerp van afvoersystemen. Een dergelijke klimatologie kan worden verkregen door jaarmaxima te selecteren uit lange neerslagreeksen. Vervolgens wordt een kansverdeling aangepast aan de geselecteerde jaarmaxima, zodat neerslaghoeveelheden kunnen worden geschat voor een gekozen herhalingstijd, die langer kan zijn dan de neerslagreeksen. In dit proefschrift worden jaarmaxima gemodelleerd met de Gegeneraliseerde Extreme Waarden (GEV) verdeling.



Met een nieuwe methode worden regenduurlijnen afgeleid op basis van 12 neerslagreeksen uit Nederland. Regenduurlijnen geven de hoeveelheid neerslag weer als functie van de duur voor gegeven herhalingstijden. Vaak worden onzekerheden niet meegenomen in het ontwerp van afvoersystemen, met het risico op een te krap bemeten systeem. Daarom worden ook de onzekerheden in de regenduurlijnen geschat.

Weerradars worden wijd en zijd gebruikt voor directe kwantitatieve neerslagschattingen over grote gebieden met hoge temporele en ruimtelijke resoluties die niet worden gehaald met traditionele regenmeternetwerken. Een 10-jarige op radar gebaseerde klimatologie van neerslaghoeveelheden wordt vervaardigd voor duren van 15 min tot 24 uur voor Nederland. Omdat radardata gevoelig kunnen zijn voor een aantal fouten, worden ze gecorrigeerd met regenmeters. Verificatie toont de goede kwaliteit van de radar dataset aan.

In het algemeen zijn er voor duren korter dan een dag maar weinig gedigitaliseerde tijdreeksen van regenmeters. Dit belemmert de studie naar regionale verschillen in extreme neerslag en het schatten van extreme gebiedsneerslag. Weerradar kan hier uitkomst bieden. Jaarmaxima worden geselecteerd uit de klimatologische radar dataset voor duren van 15 min tot 24 uur en een gebiedsgrootte van een radar pixel. De jaarmaxima worden gemodelleerd met GEV verdelingen. Voor de meeste duren worden significante regionale verschillen in extreme neerslag gevonden voor Nederland. Vervolgens worden regenduurlijnen afgeleid. De op radar gebaseerde extreme neerslagstatistieken zijn in goede overeenstemming met die gebaseerd op regenmeters, alhoewel een onderschatting wordt gevonden voor korte duren. De onzekerheden in de op radar gebaseerde regenduurlijnen zijn klein voor korte duren en worden vrij groot voor lange duren.

Gebruikmakend van de klimatologische radar dataset worden jaarmaxima geselecteerd voor gebiedsgroottes van een radar pixel tot ongeveer 1700 km<sup>2</sup>. De neerslaghoeveelheden kunnen worden berekend uit één vergelijking voor een gekozen herhalingstijd en gebiedsgrootte voor verschillende duren: de gebiedsregenduurlijn. Extreme gebiedsneerslagstatistieken op basis van regenmeterdata komen goed overeen met die uit radardata.

Het belangrijkste resultaat van dit proefschrift is dat, na correctie met regenmeterdata, weerradardata geschikt zijn om een extreme neerslagklimatologie af te leiden, inclusief onzekerheden, en bruikbaar zijn voor de bestudering van regionale verschillen in extreme neerslag.

Na als meteoroloog te zijn afgestudeerd in november 2002, deed de meteorologische sector alsof hij conjunctuurgevoelig was, waardoor er maar weinig vacatures waren. Na een periode van administratief uitzendwerk was het gelukkig mogelijk om verder te studeren in de richting van de hydrologie. De enthousiaste colleges van Bram van Putten (Wageningen Universiteit) over hydrologische statistiek wekten mijn interesse om bij hem een afstudeervak te doen over neerslagstatistiek. En tijdens een afstudeervak over statistische waterstandsverwachtingen van de Rijn en hun onzekerheden bij Paul Torfs (Wageningen Universiteit) kwam ik in aanraking met het statistische programma <sup>1</sup> (nog bedankt Paul!). Van deze extra bagage zou ik later nog veel profijt blijken te hebben en zij is, achteraf gezien, misschien ook wel nodig geweest om gemotiveerd en met voldoende achtergrondkennis aan dit promotieonderzoek te beginnen. Zo konden met  vrijwel alle figuren in dit proefschrift worden gemaakt en de extreme-waarden analyses worden uitgevoerd. In het voorjaar van 2005 kwam dan die vacature bij het KNMI waar ik niet om heen kon. De inhoud van deze promotieplaats zat op het grensvlak van meteorologie en hydrologie en de statistiek speelde (toevallig?) een hoofdrol. Echter, de weerradar was voor mij nog onontgonnen terrein. Het KNMI was mij al in positieve zin bekend van een afstudeervak uit 2002. Wel had ik aanvankelijk nog enige twijfels of een vierjarig programma wat voor mij zou zijn, maar die verdwenen, mede door advies van Bram, als sneeuw voor de zon. Achteraf gezien is het, wat mij betreft (...), de juiste keuze gebleken.

Hoe is dit promotieonderzoek eigenlijk tot stand gekomen? Welnu, dit promotieonderzoek is mogelijk gemaakt door de Staatssecretaris van het Ministerie van Verkeer en Waterstaat. Ter gelegenheid van het 150-jarig bestaan van het KNMI werd financiering gegeven voor vier jubileum onderzoekers in opleiding. Na een interne evaluatieronde werd besloten dat de, statistisch gezien, onafhankelijk van elkaar ingediende voorstellen van Adri Buishand en Iwan Holleman samengevoegd moesten worden. Dit leidde tot een project waarin een brug werd geslagen tussen de “statistiekwereld” en de “radarwereld”, alsmede tussen de afdeling Klimaatdata en -advies van de sector Klimaat en Seismologie en de afdeling Onderzoek van de sector Weer.


De eersten die ik wil bedanken zijn mijn copromotors Adri Buishand en Iwan Holleman en mijn promotor Remko Uijlenhoet. Adri, ik heb veel geleerd van je precisie en kennis en wil je hartelijk bedanken voor je grote inzet. Iwan, je hebt me de afgelopen vier jaar erg weten te motiveren en hield daarbij altijd de grote lijn en het einddoel voor ogen. Ook voor jou geldt dat je veel tijd voor me had en ik wil je dan ook hartelijk bedanken voor alle begeleiding. Uiteindelijk is gebleken dat jullie, Adri en Iwan, elkaar goed aanvulden: door de verschillende expertises kwam ik zelden in een inhoudelijke spagaat te zitten. En Remko, sinds het begin was je betrokken bij dit project. Ik wil je hartelijk bedanken voor

---

<sup>1</sup><http://www.r-project.org/>

je bijdrage en supervisie die onder andere uitmondde in je coauteurschap van hoofdstuk 5. Adri, Iwan en Remko: bedankt voor de plezierige samenwerking! Zonder jullie en het goede onderzoeksplan, was het mij nooit gelukt om alles binnen een redelijke tijd af te ronden.

Een beperkt aantal KNMI collega's wil ik hierbij in het bijzonder noemen. Hans Beekhuis, bedankt voor het uitdragen van je radarkennis en je commentaar op hoofdstuk 1. Rudolf van Westrhenen wil ik hartelijk bedanken voor het archiveren van de radardata op zijn werkstation van 1998 tot medio 2003. Hierdoor was het mogelijk om bruikbare neerslagstatistieken te berekenen op basis van radardata. Siebren de Haan wil ik bedanken voor zijn bestanden die als voorbeeld dienden om dit proefschrift op te maken. Ook wil ik mijn afdelingshoofd Gerrit Burgers bedanken voor zijn interesse en motivatie. Vele andere collega's zijn ook behulpzaam geweest in het beantwoorden van vragen en het leveren van data, waarvoor dank. Verder wil ik ook mijn kamergenoot Hans de Vries bedanken voor de prettige sfeer en je behulpzaamheid bij vragen over Linux en het opmaakstelsel  $\text{\LaTeX}$ . Met dat laatste is dit proefschrift vervaardigd, dat overigens gedrukt is door A-D Druk te Zeist. In het bijzonder nog een dankwoord voor mijn collega's van Weer Onderzoek. De plezierige, ongedwongen sfeer en "lunchcultuur", waarbij het over meer dan weer ging, heb ik altijd erg gewaardeerd.

Verder wil ik Hanneke Schuurmans (voorheen Universiteit Utrecht, nu FutureWater) bedanken voor de -scriptjes die als basis dienden voor de visualisatie van de radarbeelden in dit proefschrift. Ook een woord van dank aan Hidde Leijnse, Pieter Hazenberg en Remco van de Beek (Wageningen Universiteit), Adriaan Dokter (KNMI) en wederom Hanneke voor de uitwisseling van kennis m.b.t. weerradaronderzoek. Ook wil ik Iwan's moeder, M. van Rens, bedanken voor het beschikbaar stellen van de foto van wateroverlast op de omslag van dit proefschrift. Thanks to Markus Peura (Finnish Meteorological Institute) for providing Figure 1.3.

In de privésfeer hebben een aantal familieleden, vrienden & vriendinnen regelmatig een luisterend oor geboden, wat ik altijd erg waardeerde. Het zou me niets verbazen als jullie er weleens moe van werden... Een aantal van hen wil ik hier expliciet noemen. Ten eerste mijn ouders. Bedankt dat jullie me altijd hebben gestimuleerd om te studeren en dat ook mogelijk hebben gemaakt! Verder wil ik mijn broer Edwin, mijn paranimfen Luuc en Stefan, Gert-Jan & Celia en Peter L. bedanken voor hun steun. Evenals een bijzonder persoon die er in het eindtraject pas bij kwam: Annemarie. Ten slotte, dank aan God!

Aart Overeem  
Zeist, oktober 2009

# Contents

1	Introduction	1
1.1	Motivation	2
1.1.1	Importance of a climatology of extreme rainfall	2
1.1.2	Recent studies of extreme rainfall statistics for the Netherlands	3
1.1.3	Potential of weather radar	4
1.1.4	Research questions	7
1.2	Quantitative precipitation estimation from weather radar	8
1.2.1	Pulses, echo powers and sampling	8
1.2.2	The radar equation	11
1.2.3	From radar reflectivity factor to rainfall intensity	13
1.3	Outline	14
2	Rainfall depth-duration-frequency curves and their uncertainties	17
2.1	Introduction	18
2.2	Rainfall data	19
2.2.1	Rain gauge networks	19
2.2.2	Adjustment of automatic gauge data	21
2.3	Regional variability in extreme rainfall statistics	21
2.3.1	Fitting a GEV distribution	22
2.3.2	Regional variability in GEV parameters	24
2.4	Regional estimation and modelling of GEV parameters	25
2.4.1	Estimated GEV parameters for individual durations	25
2.4.2	Correlations of estimated GEV parameters	27
2.4.3	GEV parameters as a function of duration	28
2.5	Construction of rainfall DDF curves and their uncertainties	31
2.5.1	Derivation of DDF curves	31
2.5.2	Modelling uncertainty in DDF curves	31
2.6	Conclusions	33
3	Derivation of a 10-year radar-based climatology of rainfall	35
3.1	Introduction	36
3.2	Radar and rain gauge data	38

3.2.1	Radar data	38
3.2.2	Rain gauge networks	40
3.3	Adjustment of radar-based rainfall accumulations	41
3.3.1	Correction for occultation per radar	41
3.3.2	Daily VPR and bias adjustment per radar (VPR adjustment)	41
3.3.3	Compositing of accumulation images	43
3.3.4	Daily spatial adjustment of composites (S adjustment)	43
3.3.5	Hourly mean-field bias adjustment of composites (MFB adjustment)	44
3.3.6	Spatial adjustment of MFB-adjusted composites (MFBS adjustment)	45
3.4	Characterization and verification of adjusted accumulations	45
3.4.1	Seasonal cycle of the VPR gradient	45
3.4.2	Verification with manual rain gauges	46
3.4.3	Verification with automatic rain gauges	48
3.5	Long-term radar rainfall statistics	50
3.5.1	Empirical exceedance probabilities	50
3.5.2	Rainfall frequency and maximum rainfall depths	52
3.5.3	Spatial correlation	53
3.6	Conclusions and recommendations	55
4	Extreme rainfall analysis and estimation of DDF curves using radar	59
4.1	Introduction	60
4.2	Radar and rain gauge data	61
4.3	Adjustment of radar-based rainfall depths	62
4.3.1	Adjustment method	62
4.3.2	Derivation of adjusted 15-min to 120-min composites	63
4.4	Characteristics of annual maxima	64
4.5	Regional variability in extreme rainfall statistics	67
4.5.1	Fitting a GEV distribution	67
4.5.2	Bootstrap samples	69
4.5.3	Test for regional variability in $\mu$	70
4.6	Comparison of radar and rain gauge extreme rainfall statistics	75
4.7	Regional estimation and modeling of GEV parameters	76
4.7.1	Estimated GEV parameters for individual durations	76
4.7.2	GEV parameters as a function of duration	78
4.8	Construction of DDF curves and modeling their uncertainties	78
4.8.1	Derivation of DDF curves	78
4.8.2	Modeling uncertainty in DDF curves	79
4.8.3	Local DDF curves	80
4.9	Discussion and conclusions	81

5	Extreme-value modeling of areal rainfall from weather radar	85
5.1	Introduction	86
5.2	Radar data	87
5.3	Extreme-value modeling of areal rainfall	88
5.3.1	Abstracting annual maxima	88
5.3.2	Fitting a GEV distribution	88
5.3.3	Bootstrap samples	91
5.4	GEV parameters as a function of duration and area size	91
5.5	Derivation of areal DDF curves and their uncertainties	94
5.6	Areal reduction factors	96
5.7	Discussion and conclusions	98
6	Conclusions and outlook	101
6.1	Summary	102
6.2	Conclusions	102
6.3	Outlook	105
6.3.1	The future of QPE	105
6.3.2	Applications of climatological radar rainfall data sets	107
	Bibliography	109
A	Bootstrap algorithm	121
B	Maximum likelihood versus L-moments	123
C	Influence of missing data on estimated GEV parameters	127
	List of Publications	128
	Curriculum Vitae	131





# Chapter 1

---

## Introduction



*Inundation due to an extreme rainfall event in Nijmegen, the Netherlands  
(Courtesy of M. van Rens)*

## 1.1 Motivation

### 1.1.1 Importance of a climatology of extreme rainfall

Extreme rainfall events have a large impact on society and can lead to loss of life and property, for instance, by causing land slides or flooding due to dike breach or dam failure. Such events may also give rise to an exceedance of the capacity of sewer systems resulting in inundation of streets and basements. To prevent such hazards and nuisance proper design criteria have to be formulated. It is up to society to decide which risk is acceptable, for instance, how often flooding is allowed to occur. Subsequently, scientists can estimate the discharges and rainfalls, which are used to design hydraulic structures according to the criteria as laid down by law or agreement. Thus, accurate estimates of extreme rainfall depths and discharges are of the utmost importance.

In the Netherlands, “Het nationaal bestuursakkoord water”, a covenant between the Dutch government, provincial authorities, municipalities, and water authorities, gives design criteria for the regional water system. Criteria of flooding from water systems differ with respect to type of land use. For example, flooding from surface water is allowed to occur on average from once in 100 years for urbanized areas to once in 10 years for grassland. Because discharge records for regional water systems are often not available, rainfall data have to be used. In the Netherlands, most sewer systems are designed to discharge a design storm corresponding to a return period of approximately 2 years. More extreme events with a return period of 10-25 years lead to inundated streets and underpasses. In addition, events with a return period of 50 years may, for instance, result in buildings suffering water damage. For more information, see Van Luijelaar (2006). Urban areas and sewer systems in the Netherlands are particularly vulnerable to convective rainfall events with a duration shorter than 40 minutes (Zondervan, 1978). For regional water systems events lasting several hours to days are of main concern.

This thesis focuses on the statistics of extreme rainfall for the Netherlands. These statistics are not only relevant for design purposes in water management, such as the construction of sewer systems (Figure 1.1), the determination of the required discharge capacity of waterways or the required pumping capacity of polders. Other uses are important as well, for example, the evaluation of hazardous weather, advice to the general public, insurance of water damage, and, last but not least, scientific understanding. Statistics of extreme rainfall are usually calculated by abstracting annual maxima or maxima above a certain threshold from a long rain gauge record. Next, a probability distribution is fitted to the selected maxima, so that quantiles of rainfall depths can be estimated for a chosen return period from a single equation. Another reason for fitting a probability distribution is that long return periods can be of interest, whereas the relatively short rain gauge records often do not contain the corresponding extreme events. Hence, extrapolation is necessary.



**Figure 1.1:** A sewer system under construction.

### 1.1.2 Recent studies of extreme rainfall statistics for the Netherlands

For many years the work of Buishand and Velds (1980) was considered as the reference climatology of extreme rainfall for the Netherlands for durations of 5 min to 10 days. Annual maxima from the period 1906-1977 were obtained from the automatic rain gauge in De Bilt and were modelled with a Gumbel distribution. Several other studies using extreme rainfall data from the Netherlands have been performed the last decades, the most apparent ones being mentioned below.

The PhD thesis by Witter (1984), "Heterogeneity of Dutch Rainfall", is the predecessor of this thesis at Wageningen University. Witter developed a test for regional variability in rainfall, which is also used in Chapter 4 of this thesis, and studied regional variability in mean annual rainfall and (trends in) seasonal exceedance frequencies of a high threshold (15 and 25 mm) of daily rainfall, based on 140 rain gauge records.

Usually, extreme rainfall statistics are derived for a location, based on point measurements. There is also interest for these statistics for larger areas, which can be computed from the point rainfall statistics using an areal reduction factor (ARF). For example, Witter calculated ARFs from annual maxima series and peak-over-threshold series, without employing an extreme value distribution, for area sizes up to 1000 km<sup>2</sup> and durations of 1 h and 24 h (0800 - 0800 UTC).

Van Montfort and Witter (1986) modelled the exceedances of rainfall depths above a certain threshold using hourly data from De Bilt (1906-1982) and daily data from 32 stations (1932-1979). Buishand (1991) performed a regional frequency analysis using annual 1- to 10-day rainfall maxima from 15 stations, and studied a record of 120 daily rainfall depths of at least 80 mm for the period 1866-1989. Buishand et al. (1991) is one of the few Dutch studies

devoted to extreme rainfall modelling of subhourly maxima: 15-min annual maxima were abstracted from 25-year records of three automatic rain gauges. Buishand (1993) derived rainfall depth-duration-frequency (DDF) curves for durations of 1 to 10 days using daily rainfall depths from De Bilt for the period 1906-1977. Rainfall DDF curves describe the rainfall depth as a function of duration for a given return period. Because of a similar climate, Belgian studies are also of interest for the Netherlands, such as Delbeke (2000), Willems (2000) and Gellens (2003). Delbeke (2000) calculated depth-duration-frequency curves using the Gumbel distribution for durations of 10 min to 7 days based on a 100-year record from Uccle, Belgium, and several shorter records (18-28 years) in Flanders. Gellens (2003) considered the whole of Belgium and applied the Generalized Extreme Value (GEV) distribution.

Smits et al. (2004) derived a climatology for the Netherlands, a new reference, using the time series of the automatic rain gauge in De Bilt for the period 1906-2003. They applied a GEV distribution and a peak-over-threshold method to model rainfall maxima for durations of 4 h to 9 days and briefly investigated whether the statistics for the Bilt are representative of the rest of the country. In addition to this report, Buishand and Wijngaard (2007) performed a new analysis of the 5-min to 120-min annual maxima from De Bilt from 1906-1990 using the GEV distribution. Based on a recommendation from Smits et al. (2004) an extensive regional analysis was undertaken in the framework of the project “Van neerslag tot schade”: Buishand et al. (2009) studied regional differences in extreme rainfall for durations of 1 to 9 days using 55-year records of daily rainfall depths obtained from 141 manual rain gauges, most of them from the same locations as used in Witter (1984). They found that the rainfall statistics from De Bilt are representative of a large part of the country, however, for several parts the extreme value statistics from De Bilt should be multiplied with a correction factor varying from 0.93 to 1.14. Some other recommendations by Smits et al. (2004) are combining records from several stations to reduce the uncertainty in estimated extreme rainfall statistics, which was followed in Buishand et al. (2009), and the calculation of extreme *areal* rainfall statistics, which is particularly important for water authorities. A final recommendation concerns the regional variability of extreme subdaily rainfall, which remains a topic that has hardly been studied.

### 1.1.3 Potential of weather radar

Precipitation is measured operationally using primarily rain gauges, ground-based weather radars and satellites. Quantitative precipitation estimation (QPE) from satellites is considered to be less accurate than from rain gauges and radars, but is particularly valuable over oceans and remote areas, where few ground-based (remote sensing) measurements are available. Weather radars have become an important tool for real-time QPE over large areas and are, for instance, used in water management and nowcasting of precipitation. Current operational weather radars have a spatial resolution of typically 1 km in the horizontal and a temporal resolution of 5 min. Figure 1.2 shows the KNMI radar tower in De Bilt, the Netherlands (left). KNMI radar rainfall products are extensively used by the hydrological commu-





**Figure 1.2:** The radar tower in De Bilt, the Netherlands (left), view from the radar in De Bilt in the direction of a major building which partly blocks the lowest radar beam (middle), the best of two worlds (right): combine the rain gauge (in front) and the weather radar (background). The radome protects the antenna of the radar system.

nity, especially water authorities, and there is even a tendency to start using these products for urban water management. This is the result of the improved quality of radar rainfall products and new commercial hydrological software. A development in the Netherlands is the KNMI warning system for water authorities which uses the precipitation history, and nowcasting of precipitation from weather radar and a numerical weather prediction model to forecast rainfall, and is operational since 2003 (Kok et al., 2009). Taking into account the local discharge and storage capacity, automatic warnings are issued if chosen thresholds of rainfall depths are exceeded with a certain probability. This system is used by about half of the water authorities in the Netherlands. Radar could also be potentially useful for deriving extreme rainfall statistics, particularly for short durations and for different areas.

The number of radars has grown steadily over the years resulting in an almost complete coverage of, among others, the United States and Europe. Nowadays, the general public can freely access real-time radar images of rainfall intensities on the Internet, the most well-known radar product. Another product is the radar echotop, based on reflectivity data from typically 15 scan elevations providing an indication of the maximum height of showers, which is important for aviation meteorology. In addition to QPE, weather radars of the Doppler type can also be used to obtain wind profiles or, by combining output of more radars, horizontal dual-Doppler wind fields if it is raining. A new development is to monitor bird migration using operational weather radars, currently investigated in the framework of the project Flysafe of the European Space Agency (Dekker et al., 2008). This is of importance

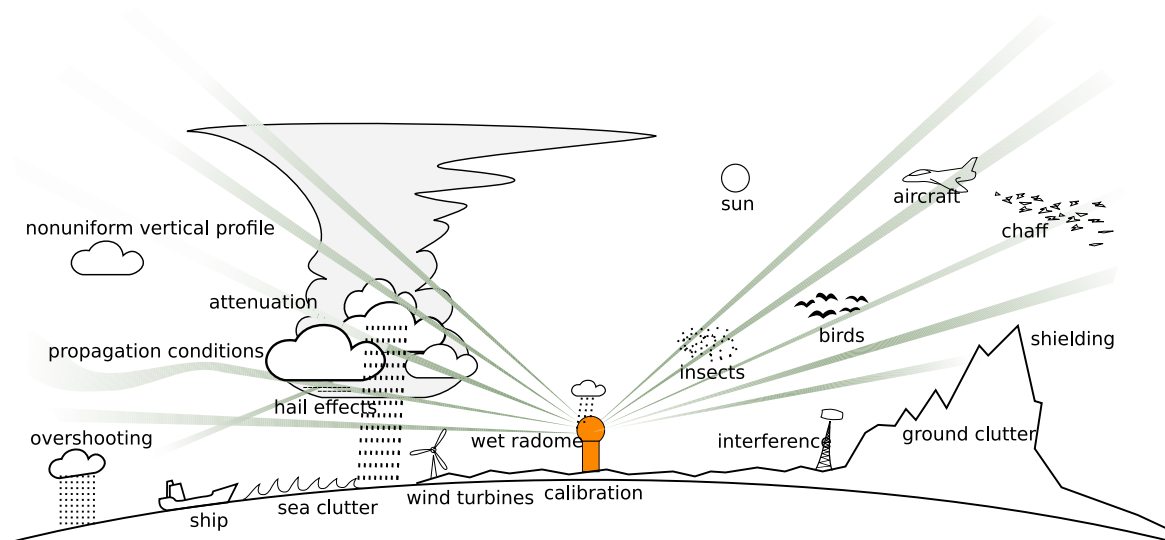


**Figure 1.3:** This figure shows the many errors which may hamper quantitative precipitation estimation using weather radar. Reproduced by permission of Markus Peura (Finnish Meteorological Institute).

for the biological community and for aviation, in order to prevent bird strikes.

Radar can be useful to derive subdaily extreme rainfall depths. Several studies present subdaily extreme rainfall statistics using rain gauges, for instance, Koutsoyiannis et al. (1998), Alila (1999) and Madsen et al. (2002). However, the description of regional variability of extreme rainfall statistics and the study of extreme rainfall over an area have often been hampered by the low density of rain gauge networks and the lack of digitized time series. With the long time series that become available, radar holds a promise to bridge this gap. However, as discussed more extensively in Chapter 3, QPE from weather radar can be hampered by a number of errors. See Figure 1.3 for an overview. One of the errors is beam-blockage: Figure 1.2 (middle) shows a photograph, which was taken from the radar, of a building located 1.9 km from the radar site in De Bilt, which blocks part of the lowest radar beam over an azimuth of  $4^\circ$ . The influence at long range from the radar of this specific building on the monthly accumulated rainfall depth can be seen in the area indicated by the white box in Figure 3.3 (a, page 56).

Radar measures precipitation indirectly, using several assumptions, and at larger altitudes above the earth's surface, whereas for most applications rainfall at the earth's surface is of interest. Therefore, it is necessary to adjust radar rainfall depths before these can be used to derive a rainfall climatology. Volumetric (3-D) radar data can be employed to obtain better precipitation estimates. Unfortunately, long time series (10 years or so) of volumetric radar data will in general not be available up to now, at least not for the Netherlands.



**Figure 1.4:** The manual rain gauge (left) and the automatic rain gauge (right) part of KNMI's rain gauge networks.

The alternative for obtaining high-quality radar rainfall depths is to employ rain gauge data to adjust 2-D radar data, an approach also followed in this thesis. Rain gauge data are assumed to provide accurate point measurements of rainfall, while weather radars give semi-quantitative precipitation estimates. In contrast, radars are capable of revealing the spatial structure of rainfall in detail, whereas this can usually not be obtained from rain gauges. The best of two worlds is to combine weather radar with rain gauge data (Figure 1.2, right). For that purpose, both KNMI rain gauge networks were utilized: an automatic network with 1-h rainfall depths for each clock-hour ( $\approx 1$  station per  $1000 \text{ km}^2$ ) and a manual network with 24-h 0800-0800 UTC rainfall depths ( $\approx 1$  station per  $100 \text{ km}^2$ ). Figure 1.4 shows the manual rain gauge (left) and the automatic rain gauge (right) which is used at most automatic weather stations. The automatic rain gauge is surrounded by a wall with a height of 0.40 m to avoid undercatch due to turbulence.

#### 1.1.4 Research questions

In the overview of recent studies in Section 1.1.2, several recommendations are given for further research, which provided a motivation for the current project. Apart from these recommendations, another important aspect is that uncertainties in extreme rainfall events are often disregarded and are not incorporated in the design of hydraulic structures leading to an increased risk. This shows the importance of estimating the uncertainty in extreme rainfall statistics. This leads to the following research question:

- *How to quantify the uncertainty in rainfall depth-duration-frequency (DDF) curves?*

Section 1.1.3 shows the potential of QPE with radar. Given the large number of possible errors in QPE with radar, one might wonder whether adjustment procedures succeed in removing these errors for extreme rainfall events sufficiently. In addition, an 11-year record could be too short to obtain reliable extreme rainfall depths from an extreme value model, resulting in the next research question:

- *How reliable are the rainfall depths for given return periods based on weather radar?*

The high spatial resolution of radar data and the availability of 12 long rain gauge records of subdaily rainfall provide new opportunities to study regional variation in extreme rainfall in the Netherlands. Often, the extreme rainfall data which are used by the hydrological community, are from the automatic rain gauge in De Bilt, in the middle of the country. This is not appropriate in the case of regional variability in extreme rainfall. Therefore, attention is given to the research question:

- *Are regional differences in extreme rainfall significant for durations of 15 min to 24 h?*

Quite often the actual interest is not in extreme point rainfall statistics but in extreme areal rainfall statistics. Generally, dense rain gauge networks are not available. Because of the large number of observations in space, weather radar holds a promise in deriving DDF curves for larger area sizes. This gives rise to the research question:

- *What is the value of weather radar to obtain areal DDF curves?*

## 1.2 Quantitative precipitation estimation from weather radar

Radar is frequently used for remote sensing of the atmosphere. Radars developed during World War II to detect enemy aircraft also revealed precipitation echoes, which were considered as noise. Since then, radars have been developed which were specifically designed to detect precipitation. In Chapter 3 a description is given of quantitative precipitation estimation from weather radar including possible (sources of) errors. In this section the measurement principle of a typical operational weather radar is discussed in more detail.

### 1.2.1 Pulses, echo powers and sampling

The KNMI weather radars transmit electromagnetic radiation as pulses with a duration  $\tau$  of 0.8 or 2  $\mu$ s and a repetition frequency between 250 Hz and 1200 Hz. These high-frequency signals (5.6 GHz) are generated by a magnetron transmitter and transferred to the antenna by means of a waveguide, which is a hollow, rectangular metal tube matched to wavelength  $\lambda$  shown in Figure 1.5 (left). The antenna feed of the waveguide is located at the focal point of a circular parabolic reflector with a diameter of 4.2 m, see Figures 1.5 (right) and 1.6. Thus,





**Figure 1.5:** Transmitter cabinet, receiver cabinet and waveguide (left), and the circular parabolic reflector of the KNMI weather radar in De Bilt.

the pulse transmitted by the antenna feed is reflected into the atmosphere by the circular parabolic reflector. Since the reflector is directional, most power is captured in the central portion of the beam, the main lobe, in all directions perpendicular to the electromagnetic wave, called the half-power beamwidth  $\phi$  ( $^\circ$ ):

$$\phi = \frac{70\lambda}{d}, \quad (1.1)$$

where  $d$  is the diameter (m) of the circular parabolic reflector. For the KNMI radar this is approximately  $1^\circ$ . A small part of the power is contained in the sidelobes, which occur in every direction. The main lobe has approximately a Gaussian beam pattern. The gain is defined as:

$$g = \frac{p_1}{p_2}, \quad (1.2)$$

with  $p_1$  the power on the axis of the radar antenna and  $p_2$  the power on the same location without an antenna. The KNMI antennas have a gain of approximately  $2.0 \cdot 10^4$  (43 dB). Part of the radiation is backscattered by hydrometeors, such as rain droplets, snow flakes and ice crystals. The receiver of the radar system is capable of measuring the backscattered echoes. Because the reflector is directional, the position of targets can be computed from the range, the beam elevation with respect to the earth's surface and the azimuth, which is the direction of the radar antenna in terms of the  $360^\circ$  compass (Rinehart, 2004). The range of a target  $r$  (km) with respect to the radar can be calculated from the time delay of the echo using:

$$r = \frac{ct}{2}, \quad (1.3)$$

where  $c$  is the speed of light ( $\text{km s}^{-1}$ ) and  $t$  (s) is the time delay between transmission and reception of a pulse.

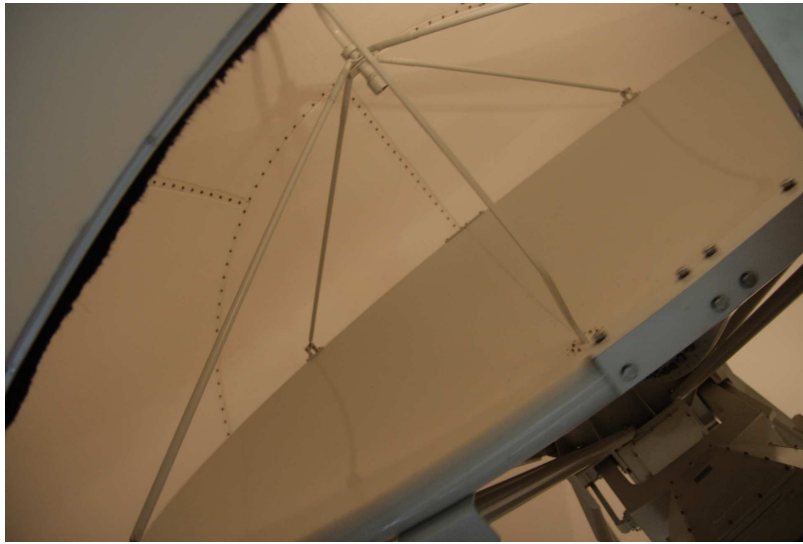


**Figure 1.6:** The circular parabolic reflector with antenna feed, together named antenna, of the KNMI weather radar in De Bilt.

The quality of the observations clearly deteriorates at long ranges and is of limited value beyond ranges of approximately 200 km. This is caused by overshooting of precipitation, due to the larger height of the radar beam above the earth's surface. Moreover, in the derivation of the radar equation it is assumed that a radar sample volume is homogeneously filled with randomly scattered precipitation particles, whereas partial beam filling may occur: since the measurement volume increases with range, the same storm will occupy a relatively small part of the measurement volume at long ranges leading to a reduction in the received echo powers (Rinehart, 2004).

The radar measures echo powers in 360 azimuth sectors of  $1^\circ$ , each of them containing range gates with a size of 125 m. Note that the radar reflectivity factor (see Section 1.2.2) from a single pulse assigned to a certain range gate is a measurement over a distance of 300 m (for  $\tau = 2 \mu\text{s}$ ) in the direction of the radar resulting in a spatially smoothed measurement. The signal processor converts the echo powers to radar reflectivity factors using the radar equation. For the lowest elevation angle of  $0.3^\circ$ , approximately 14 pulses are transmitted for each  $1^\circ$ -azimuth sector from which the corresponding radar reflectivity factors are averaged over each range gate. Since the beam also covers adjacent azimuth sectors, the average radar reflectivity factor of a range gate is influenced somewhat by hydrometeors in those surrounding sectors.

Subsequently, the radar reflectivity factors from the first 8 adjacent range gates are averaged. This is repeated for the next 8 adjacent range gates, and so on. This results in a table with elements of radar reflectivity factors as a function of azimuth and range. The advantage of averaging reflectivity factors is that each element covering  $1^\circ \times 1 \text{ km}$  is based on 112 pulses (for an elevation angle of  $0.3^\circ$ ), so that they become more accurate. These elements can be

projected on a polar stereographic grid with pixels having a spatial resolution of  $2.4 \times 2.4$  km<sup>2</sup> (this thesis). The spatial resolution has been increased to  $1 \times 1$  km<sup>2</sup> from January 2008.

### 1.2.2 The radar equation

In this section the main steps in deriving the radar equation are described. This equation is utilized to convert echo powers measured by the receiver of the radar system to radar reflectivity factors. For an isotropic antenna, the same amount of power is transmitted in all directions. The power is distributed over the surface of a sphere, leading to a power per unit area, a power density  $S$  (W m<sup>-2</sup>) of:

$$S = \frac{p_t}{4\pi r^2}, \quad (1.4)$$

with  $p_t$  the transmitted power (W) and  $r$  the range from the radar (m). For the KNMI weather radars  $p_t$  is approximately 270 kW. Since a weather radar has a directional antenna, Eq. 1.4 has to be multiplied by the gain from Eq. 1.2. A target with cross section  $\sigma$  (m<sup>2</sup>) along the beam axis intercepts a power  $p_\sigma$  (W):

$$p_\sigma = \frac{p_t g \sigma}{4\pi r^2}, \quad (1.5)$$

where  $\sigma$  is not necessarily equal to the physical size of the target.

Hydrometeors have an approximately spherical shape and their diameter  $D$  is usually small with respect to the wavelength of the radar pulse, i.e.,  $D/\lambda < 0.1$ , with  $\lambda$  being approximately 0.053 m for C-band radars. Because of this, the Rayleigh scattering approximation holds, so that the backscattering cross section of an individual target,  $\sigma_i$  (m<sup>2</sup>), is given by:

$$\sigma_i = \frac{\pi^5 |K|^2 D_i^6}{\lambda^4}, \quad (1.6)$$

where  $|K|^2$  is a coefficient related to the dielectric constant of the hydrometeor (0.93 for liquid water and 0.197 for ice). Note that cloud particles can only be detected by operational weather radars at very short ranges.

Because a backscattering cross section is used, targets are assumed to reflect the power isotropically and only part of this radiation,  $p_r$ , is measured by the receiver of the radar system:

$$p_r = \frac{p_\sigma A_e}{4\pi r^2} = \frac{p_t g \sigma_i A_e}{16\pi^2 r^4}, \quad (1.7)$$

where  $A_e$  is the effective area of the antenna, which is given by:

$$A_e = \frac{g \lambda^2}{4\pi}. \quad (1.8)$$

This leads to the following radar equation for the averaged received power from a point target at the centre of a radar beam (Rinehart, 2004).

$$p_r = \frac{p_t g^2 \lambda^2 \sigma_i}{64\pi^3 r^4}. \quad (1.9)$$

The volume a radar samples,  $V$ , may contain many rain droplets or ice particles, which all have an individual backscattering cross section. The radar reflectivity  $\eta$  is given by:

$$\eta = \sum_{vol} \sigma_i = \frac{\sigma_t}{V}, \quad (1.10)$$

where  $\sigma_t$  is the total reflectivity and  $vol$  represents a unit volume of  $1 \text{ m}^3$ . Replacing  $\sigma_i$  in Eq. 1.9 with  $\sigma_i$  and substituting Eq. 1.6 gives:

$$p_r = \frac{p_t g^2 \pi^2 |K|^2 V \eta}{64 \lambda^2 r^4}, \quad (1.11)$$

where  $V$  is the volume of the radar sample. Probert-Jones (1962) developed an expression for  $V$  for circular parabolic reflectors, which takes into account the approximate Gaussian shape of the beam pattern:

$$V = \frac{\pi r^2 \theta \phi c \tau}{16 \log 2}, \quad (1.12)$$

with  $\theta$  and  $\phi$  the horizontal and vertical beamwidths (radians), which are usually equal. This replaced an empirical factor in the radar equation, which was needed to obtain better precipitation estimates (Marshall et al., 1955). Probert-Jones realized that this unknown factor was due to the power distribution in the main lobe which was not taken into account.

Since the diameters of the individual rain droplets are not known, a radar reflectivity factor  $Z$  is defined, which is independent of radar type and wavelength, and therefore a property of the atmosphere:

$$Z = \sum_{vol} D^6. \quad (1.13)$$

Eqs. 1.11 and 1.12 contain a number of properties of the radar:  $p_t$ ,  $g$ ,  $\theta$ ,  $\phi$  and  $\lambda$  and a number of constants, which are combined in the so-called radar constant  $C$ . Now, the radar reflectivity factor  $Z$  ( $\text{mm}^6 \text{ m}^{-3}$ ) can be calculated with the following form of the radar equation:

$$Z = C p_r r^2. \quad (1.14)$$

Because of the large range of measured values of  $Z$ , this quantity is usually expressed on a logarithmic scale:

$$Z_{dB} \equiv 10 \times \log \left[ \frac{Z}{1 \text{ mm}^6 / \text{m}^3} \right] \quad (1.15)$$

where  $Z_{dB}$  is the logarithmic radar reflectivity factor (dBZ). This can also be done for the power  $p_r$  leading to  $P_{dB}^r$ . Then, the following expression is obtained:

$$Z_{dB} = C_{dB} + P_{dB}^r + 20 \times \log r + 2ar, \quad (1.16)$$

where an extra term  $2ar$  is added, which represents losses due to atmospheric attenuation between antenna and target,  $a$  being the gaseous attenuation coefficient. Some other losses

are usually taken into account in the radar constant, such as waveguide, radome and receiver losses. Attenuation losses due to high rainfall intensities or a wet radome are not considered and are difficult to account for in an operational setting for single-polarization radars. In the derivation of the radar equation many assumptions have been made, which have been described more comprehensively in Collier (1989). The derivation of the radar equation was based on Raghavan (2003) and Rinehart (2004).

### 1.2.3 From radar reflectivity factor to rainfall intensity

In this section particular attention is given to the  $Z$ - $R$  relation, which is used to convert radar reflectivity factors  $Z$  to rainfall intensities  $R$ . Using raindrop measurements at the ground, Marshall and Palmer (1948) found that the raindrop size distribution can be approximated by an exponential distribution:

$$N(D) = N_0 e^{-\Lambda D}, \quad (1.17)$$

with  $D$  the drop size diameter (mm) and  $N(D)dD$  the mean number of raindrops with a diameter between  $D$  and  $D + dD$  in a unit volume of air, and  $N_0 = 8 \times 10^3 \text{ mm}^{-1} \text{ m}^{-3}$ . The raindrop size distribution is determined by coalescence and breakup, see, for instance, Doviak and Zrnić (1993). The coefficient  $\Lambda$  ( $\text{mm}^{-1}$ ) was found to depend on the rainfall intensity  $R$  ( $\text{mm h}^{-1}$ ):

$$\Lambda = 41R^{-0.21}. \quad (1.18)$$

Under the assumption of Rayleigh scattering,  $Z$  can be expressed as the sixth moment of the drop size distribution  $N(D)$ :

$$Z = \int_0^\infty N(D) \cdot D^6 dD, \quad (1.19)$$

which is a continuous approximation of Eq. 1.13. Using the gamma function,

$$\Gamma(x) = \int_0^\infty t^{x-1} e^{-t} dt, \quad (1.20)$$

and the Marshall-Palmer drop size distribution (Eq. 1.17), a general expression can be derived for the moments of the drop size distribution  $M(x)$ :

$$M(x) = \int_0^\infty N_0 e^{-\Lambda D} \cdot D^x dD = \frac{N_0 \Gamma(x+1)}{\Lambda^{x+1}}. \quad (1.21)$$

For instance,  $Z$  can now be written as:

$$Z = M(6) = \frac{N_0 \Gamma(7)}{\Lambda^7} = \frac{720 N_0}{\Lambda^7}. \quad (1.22)$$

By substituting Eq. 1.18 into Eq. 1.22 a  $Z$ - $R$  relationship is obtained (Marshall and Palmer, 1948):

$$Z = 296 R^{1.47}. \quad (1.23)$$

Another way to obtain a  $Z$ - $R$  relationship is to develop an expression for the rain rate  $R$ . The volume of water in one  $\text{m}^3$  of air is given by:

$$\int_0^\infty \frac{1}{6} \pi D^3 10^{-9} N(D) dD. \quad (1.24)$$

The rate of precipitation (a flux) is obtained by dividing Eq. 1.24 by an area of one  $\text{m}^2$  and multiplying with the terminal fall speed of drops  $v(D)$  ( $\text{m s}^{-1}$ ):

$$R = \int_0^\infty 10^3 \cdot 3600 \cdot \frac{1}{6} \pi D^3 10^{-9} N(D) v(D) dD, \quad (1.25)$$

with

$$v(D) \simeq \alpha D^\beta. \quad (1.26)$$

Atlas and Ulbrich (1977) found values of 3.778 and 0.67 for respectively the coefficients  $\alpha$  and  $\beta$ . Using Eq. 1.21, the total rate of precipitation  $R$  ( $\text{mm h}^{-1}$ ) can now be expressed as:

$$R = 6 \cdot 10^{-4} \pi \alpha \int_0^\infty N(D) D^{3+\beta} dD \equiv 6 \cdot 10^{-4} \pi \alpha M(3 + \beta) = \frac{6 \cdot 10^{-4} \pi \alpha N_0 \Gamma(4 + \beta)}{\Lambda^{4+\beta}}, \quad (1.27)$$

which is an expression of  $R$  as a moment of the drop size distribution  $N(D)$ . Eliminating  $\Lambda$  using Eqs. 1.22 and 1.27 results in:

$$Z = 237 R^{1.50}. \quad (1.28)$$

This shows inconsistency in the  $Z$ - $R$  relations (compare to Eq. 1.23), which has been investigated in detail by Uijlenhoet and Stricker (1999), who also developed a consistent rainfall parameterization.

The most widely used  $Z$ - $R$  relationship, which is also used for the KNMI radars, is given by:

$$Z = 200 R^{1.6}, \quad (1.29)$$

and was found by Marshall et al. (1955) from raindrop records at the ground. Eq. 1.13 was used to calculate  $Z$ . This relationship is representative for average conditions. However, these values may differ considerably depending on rainfall type, and will lead to errors in the case of snowfall.

### 1.3 Outline

This thesis is organized as follows. Chapter 2 starts with the calculation of extreme rainfall statistics for durations of 1 to 24 h using records from 12 automatic gauges from the Netherlands. Most of these records have not been employed before for this specific application. The regional variability in extreme rainfall is studied. A methodology is presented to derive the regularly used rainfall depth-duration-frequency (DDF) curves, which describe the rainfall depth as a function of duration for a given return period. Attention is given to the estimation of uncertainties in these curves.

The thesis proceeds with the derivation and verification of a 10-year data set of 1- to 24-h radar rainfall depths in Chapter 3 covering the land surface of the Netherlands. Using the climatological data set of rainfall depths from Chapter 3, an extreme value analysis is performed in Chapter 4 for durations of 15 min to 24 h. Rainfall DDF curves are derived and it is studied whether regional variability in extreme rainfall is significant. In Chapter 5

areal reduction factors and areal rainfall DDF curves are obtained from weather radar for areas ranging from a radar pixel to the size of a catchment. The thesis ends with conclusions and an outlook.







## Chapter 2

---

# Rainfall depth-duration-frequency curves and their uncertainties<sup>1</sup>

### Abstract

Rainfall depth-duration-frequency (DDF) curves describe rainfall depth as a function of duration for given return periods and are important for the design of hydraulic structures. This chapter focuses on the effects of dependence between the maximum rainfalls for different durations on the estimation of DDF curves and the modelling of uncertainty of these curves. For this purpose the hourly rainfall depths from 12 stations in the Netherlands are analysed. The records of these stations are concatenated to one station-year record, since no geographical variation in extreme rainfall statistics could be found and the spatial dependence between the maximum rainfalls appears to be small. A Generalized Extreme Value (GEV) distribution is fitted to the 514 annual rainfall maxima from the station-year record for durations of 1, 2, 4, 8, 12 and 24 h. Subsequently, the estimated GEV parameters are modelled as a function of duration to construct DDF curves, using the method of generalized least squares to account for the correlation between GEV parameters for different durations. A bootstrap estimate of the covariance matrix of the estimated GEV parameters is used in the generalized least squares procedure. It turns out that the shape parameter of the GEV distribution does not vary with duration. The bootstrap is also used to obtain 95%-confidence bands of the DDF curves. The bootstrap distribution of the estimated quantiles can be described by a lognormal distribution. The parameter  $\sigma$  of this distribution (standard deviation of the underlying normal distribution) is modelled as a function of duration and return period.

---

<sup>1</sup>*Journal of Hydrology*, 2008, **348**, pp 124-134 by Aart Overeem, Adri Buishand and Iwan Holleman.

## 2.1 Introduction

Statistics of extreme rainfall are important to society for (i) design purposes in water management - such as the construction of sewerage systems, determination of the required discharge capacity of channels and capacity of pumping stations - in order to prevent flooding, thereby reducing the loss of life and property, and pollution of surface waters; (ii) insurance of water damage and evaluation of hazardous weather, e.g. of interest for liability; (iii) advice to the general public. See e.g. Stewart et al. (1999) and Koutsoyiannis and Baloutsos (2000) for more on this subject. Accordingly, reliable calculation of probabilities of extreme rainfall with their uncertainties is of concern. Uncertainties should be taken into account, otherwise risks can be underestimated. Frequently statistics of extreme rainfall are contained in rainfall depth-duration-frequency (DDF) curves, which describe rainfall depth as a function of duration for given return periods or probabilities of exceedance.

In particular for short durations, rainfall intensity has often been considered rather than rainfall depth, leading to intensity-duration-frequency (IDF) curves. The method of derivation of the two types of curves is, however, identical. Koutsoyiannis et al. (1998) present a mathematical framework for studying IDF relationships, which also applies to DDF curves.

The first step in the construction of DDF curves is fitting some theoretical distribution to the extreme rainfall amounts for a number of fixed durations. A logical step to proceed then is to describe the change of the parameters of the distribution with duration by a functional relation. From the fitted relationships the rainfall depths for any duration and return period can be derived. A problem in this approach is that the estimated parameters for different durations are correlated. Standard regression techniques may then not be appropriate to estimate the unknown coefficients in the relationships that determine the DDF curves and the uncertainty of these relationships. Buishand (1993) studied the influence of correlation on the determination of DDF curves for De Bilt (The Netherlands) using the annual maximum amounts for durations between 1 and 10 days. A Gumbel distribution was fitted to these annual maxima. It was demonstrated that ignorance of the correlation between the estimated Gumbel parameters results in an underestimation of the standard deviation of the estimated quantiles from the DDF curves. Confidence bands of these curves and other measures of uncertainty should therefore take this correlation into account.

Though frequently used, the Gumbel distribution may underestimate quantiles for long return periods, see e.g. Buishand (1991), Koutsoyiannis and Baloutsos (2000) and Koutsoyiannis (2004). A widely-used alternative is the Generalized Extreme Value (GEV) distribution, which allows for a better description of the upper tail of the distribution, due to an additional parameter. Large samples are needed to estimate this shape parameter accurately or data from several sites in a region should be pooled assuming that the shape of the distribution does not change over the region.

This chapter deals with the construction of DDF curves for short durations (1-24 h) in the Netherlands using the GEV distribution. The GEV distribution is fitted to the annual maxima of a station-year record of 514 years based on the hourly data of 12 stations. Subsequently, using the method of generalized least squares a relation of the GEV parameters as a function of duration is estimated. The correlations between the parameter estimates for different durations are taken into account.

The bootstrap is used both for the estimation of correlation between estimated GEV parameters and for the confidence bands of the DDF curves. The latter shows similarities with the resampling technique presented by Burn (2003) to calculate confidence intervals for flood quantiles. Innovative aspect of this chapter is that the uncertainty in rainfall DDF curves is described with a lognormal probability distribution.

This chapter is organized as follows. First, the data are described. Next, the construction of the station-year record is justified. Subsequently, the GEV fits to the annual maxima of this record and the modelling of the change of the GEV parameters with duration are addressed. This is followed by a description of the construction of DDF curves and their uncertainties. The chapter closes with a discussion and conclusions.

## 2.2 Rainfall data

### 2.2.1 Rain gauge networks

KNMI maintains two independent rain gauge networks: an automatic network of approximately 35 gauges ( $\approx 1$  station per 1000 km<sup>2</sup>) and a manual network of approximately 325 gauges ( $\approx 1$  station per 100 km<sup>2</sup>). Originally the automatic network was operated using mechanical pluviographs. These have been replaced by electronic rain gauges from the end

**Table 2.1:** Selected stations, their record length, latitude, longitude and elevation.

Station name	Record length (years)	Latitude (N)	Longitude (E)	Elevation (m)
Beek	48	50.92°	5.78°	114
De Bilt	99	52.10°	5.18°	2
De Kooy	49	52.92°	4.79°	0
Eelde	49	53.12°	6.59°	4
Gilze-Rijen	29	51.57°	4.93°	11
Leeuwarden	30	53.22°	5.75°	0
Schiphol	35	52.30°	4.77°	-4
Twente	31	52.27°	6.90°	35
Valkenburg	32	52.18°	4.42°	0
Vlissingen	49	51.44°	3.60°	8
Volkel	31	51.66°	5.71°	20
Zestienhoven	32	51.95°	4.44°	-5



**Figure 2.1:** Map of the Netherlands with the locations of the 12 stations considered in this chapter.

of the 1970s. The electronic rain gauge measures the precipitation depth using the displacement of a float placed in a reservoir. The 24-h precipitation depth from the manual gauges is measured at 0800 UTC. Detailed information on the rain gauge networks of KNMI can be found in KNMI (2000).

To perform a reliable extreme value analysis, only stations with automatic rain gauges were selected for which at least 29 years of hourly precipitation depth data were available from the mid 1970s. It is noted that these depths are clock-hour sums. This selection resulted in a data set with time series from 13 stations distributed over the Netherlands. The 30-year record of one station was removed, since it was located only 7 km from De Bilt, for which a much longer record was available.

The locations of the selected stations are shown in Figure 2.1 and are listed in Table 2.1. The time series, in total 514 station years, all end in 2005. If more than 5 days in a year were missing, the year was removed from the data set. In total only 3 station years were removed. For the automatic gauge in De Bilt, the annual 1-h and 2-h rainfall maxima based on continuous recording, so-called sliding maxima, are available for the period 1906-1990. The data from the manual network were only used for adjustment of the automatic gauge observations (see below). Until the mid 1990s all stations were equipped with a collocated manual gauge. In 2005, the distance between the selected automatic gauges and the nearest manual gauge ranged from 0.3 to 6.1 km.

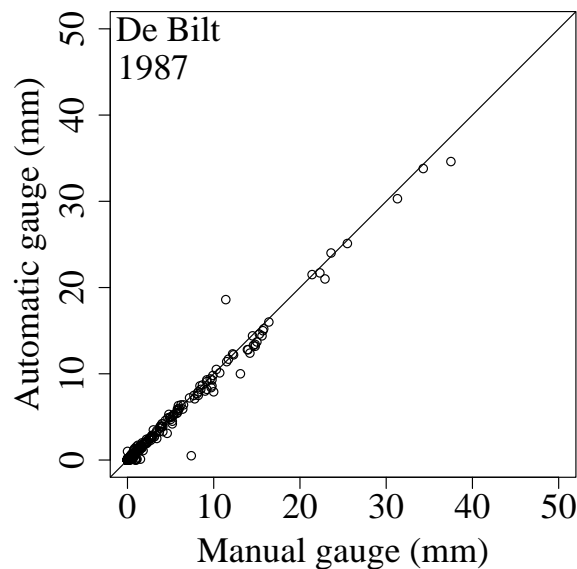


**Figure 2.2:** Daily precipitation depths (mm) of automatic versus manual gauges for De Bilt during 1987. The straight line is the  $y = x$  line.

### 2.2.2 Adjustment of automatic gauge data

The WMO (1981) Guide to Hydrological Practices states that “it was decided that the standard nonrecording rain gauge measurements should be the official rainfall readings at the station, and that a correction factor should be applied to hourly rainfall and maximum intensity data, based on the ratio of the daily total by standard gauge to the total by recording gauge.” Before 1982 the archived hourly sums from the automatic gauges were adjusted by default with the daily sums from the collocated manual gauge. From 1982 the annual rainfall sums from the manual gauges are on average 5% larger than those from the automatic gauges. To promote the homogeneity of the data set it was decided to adjust the remaining 56% of automatic gauge data (1982-2005) by the same procedure, so also the data from the mid 1990s using the readings from the nearest manual gauge.

Figure 2.2 shows a typical scatter plot of the daily precipitation depths from the automatic and the manual gauges in De Bilt during one year. Evidently the two gauges correspond rather well and the adjustment factors are generally close to unity. The extreme value analysis presented in the remainder of this chapter has been carried out using the adjusted data set. When the same analysis is performed on the (partly) unadjusted data set the differences are small.

## 2.3 Regional variability in extreme rainfall statistics

The Netherlands has a temperate climate with mean annual rainfall varying from 768 to 848 mm for the 12 selected stations. This low variation is due to the absence of significant orography. Most daily (0800-0800 UTC) annual maxima occur in the period May to Decem-

ber, whereas most annual 1-h maxima occur from May to September, caused by the larger influence of convective rainfall in summer. In this section regional variability in extreme rainfall statistics is investigated. First the GEV distribution is introduced. Then the regional variability of its parameters is studied.

### 2.3.1 Fitting a GEV distribution

The GEV distribution has been used worldwide to model rainfall maxima, see e.g. Schaefer (1990), Alila (1999), Gellens (2002), Fowler and Kilsby (2003) and Koutsoyiannis (2004). Applications to rainfall maxima in the Netherlands are given by Buishand (1991) and Smits et al. (2004). The GEV cumulative distribution function  $F(x)$  is given by (Jenkinson, 1955):

$$F(x) = \exp\left\{-\left[1 - \frac{\kappa}{\alpha}(x - \mu)\right]^{1/\kappa}\right\} \text{ for } \kappa \neq 0, \quad (2.1)$$

$$F(x) = \exp\left\{-\exp\left[-\frac{1}{\alpha}(x - \mu)\right]\right\} \equiv \exp\{-\exp[-y]\} \text{ for } \kappa = 0, \quad (2.2)$$

with  $\mu$  the location,  $\alpha$  the scale and  $\kappa$  the shape parameter of the distribution and  $y$  the Gumbel reduced variate,  $y = -\ln(-\ln F)$ . The GEV distribution combines the three asymptotic extreme value distributions into a single distribution. The type of extreme value distribution is determined by  $\kappa$ : EV1 (Gumbel distribution) if  $\kappa = 0$ ; EV2 (Fréchet type) if  $\kappa < 0$ ; and EV3 (Weibull type) if  $\kappa > 0$ . The Fréchet type has a longer upper tail than the Gumbel distribution and the Weibull type a shorter tail. Using L-moments diagrams Schaefer (1990), Alila (1999) and Kysely and Picek (2007) show that the GEV distribution describes the distribution of the annual maximum rainfall amounts much better than the Pearson type III distribution and that the GEV distribution is generally also preferable to the generalized logistic distribution. Besides, the GEV distribution is based on asymptotic theory about the distribution of maxima.

The quantile function, the inverse of Eqs. (2.1) and (2.2), is given by:

$$x(T) = \mu + \frac{\alpha \{1 - [-\ln(1 - T^{-1})]^\kappa\}}{\kappa} = \mu + \alpha \frac{1 - \exp(-\kappa y)}{\kappa} \text{ for } \kappa \neq 0, \quad (2.3)$$

$$x(T) = \mu - \alpha \ln[-\ln(1 - T^{-1})] = \mu + \alpha y \text{ for } \kappa = 0, \quad (2.4)$$

where  $T = 1/(1 - F)$  is the return period.

Running annual maxima are abstracted for each of the 12 time series from the selected stations for durations  $D$  of 1, 2, 4, 8, 12 and 24 h. Running implies here that the  $D$ -hour rainfall amounts are calculated for each clock-hour of the year. A GEV distribution is fitted to the annual maxima for each station and duration separately.

Both L-moments (Hosking and Wallis, 1997) and maximum likelihood (Coles, 2001) have been used frequently to fit the GEV distribution to annual maxima. For small samples the estimates based on L-moments generally have lower standard deviation than those based

on maximum likelihood if  $-0.2 < \kappa < 0.2$  (Hosking et al., 1985). Use of maximum likelihood with a Bayesian prior distribution for  $\kappa$  (Martins and Stedinger, 2000) or with a penalty function (Coles and Dixon, 1999) performs equally well, but is computationally more difficult. Because of this and the fact that 11 stations have a record length shorter than 50 years, the method of L-moments is chosen.

L-moments are based on linear combinations of the order statistics of the annual maximum rainfall amounts. First, the probability weighted moments are estimated by:

$$b_0 = n^{-1} \sum_{j=1}^n x_{j:n}, \quad (2.5)$$

$$b_1 = n^{-1} \sum_{j=2}^n \frac{j-1}{n-1} x_{j:n}, \quad (2.6)$$

$$b_2 = n^{-1} \sum_{j=3}^n \frac{(j-1)(j-2)}{(n-1)(n-2)} x_{j:n}, \quad (2.7)$$

where  $x_{1:n} \leq x_{2:n} \leq \dots \leq x_{n:n}$  is the ordered sample of annual maxima. The sample L-moments are then obtained as:

$$\ell_1 = b_0, \quad (2.8)$$

$$\ell_2 = 2b_1 - b_0, \quad (2.9)$$

$$\ell_3 = 6b_2 - 6b_1 + b_0. \quad (2.10)$$

The estimate  $\hat{\kappa}$  of the shape parameter  $\kappa$  follows from:

$$\hat{\kappa} = 7.8590 c + 2.9554 c^2, \quad (2.11)$$

where

$$c = \frac{2}{3 + \ell_3/\ell_2} - \frac{\ln 2}{\ln 3}. \quad (2.12)$$

The estimates  $\hat{\alpha}$  and  $\hat{\mu}$  of  $\alpha$  and  $\mu$  are subsequently obtained as:

$$\hat{\alpha} = \frac{\ell_2 \hat{\kappa}}{(1 - 2^{-\hat{\kappa}}) \Gamma(1 + \hat{\kappa})}, \quad (2.13)$$

$$\hat{\mu} = \ell_1 - \hat{\alpha} \frac{1 - \Gamma(1 + \hat{\kappa})}{\hat{\kappa}}, \quad (2.14)$$

with  $\Gamma(\cdot)$  the gamma function.

In this chapter  $\hat{\gamma} = \hat{\alpha}/\hat{\mu}$  is considered instead of  $\hat{\alpha}$ . The advantage of using  $\hat{\gamma}$  is that its correlation with  $\hat{\mu}$  and  $\hat{\kappa}$  is weak. The shape parameter  $\kappa$  is often assumed to be constant over a region and can then be estimated by combining all station records in that region. For the index flood method  $\gamma$  is also considered to be constant in a region. This assumption has often been made in rainfall frequency analysis (Gellens, 2002; Fowler and Kilsby, 2003; Mora et al., 2005).

### 2.3.2 Regional variability in GEV parameters

In this section the equality of GEV parameters is tested. The tests below assume that spatial dependence of the annual maxima can be neglected. Figure 2.3, which is representative of all six durations, shows that the cross correlations between the annual maxima of the 12 stations are small. Data for the common period 1977-2005 were used to estimate these cross correlations. For annual maxima of daily rainfall it is further shown by Buishand (1984), using data from 140 stations located in the Netherlands, that the degree of association decreases with event magnitude. There is almost no association between the occurrence of large values if the interstation distance is larger than 30 km.

Let  $\theta_i$  be the value of a GEV parameter ( $\mu$ ,  $\gamma$  or  $\kappa$ ) at station  $i$ . The equality of the  $\theta_i$ 's can be tested with the statistic:

$$X^2 = \sum_{i=1}^{12} (\hat{\theta}_i - \hat{\theta}_w)^2 / \sigma^2(\hat{\theta}_i), \quad (2.15)$$

with  $\hat{\theta}_i$  the L-moments estimate of  $\theta_i$  and  $\hat{\theta}_w$  the weighted average of the  $\hat{\theta}_i$ 's defined as:

$$\hat{\theta}_w = \sum_{i=1}^{12} n_i \hat{\theta}_i / \sum_{i=1}^{12} n_i, \quad (2.16)$$

where  $n_i$  is the record length at station  $i$ . The variance  $\sigma^2(\hat{\theta}_i)$  in Eq. (2.15) was based on the asymptotic covariance matrix of the L-moments estimators of the GEV parameters as given by Hosking et al. (1985). The variance of  $\hat{\gamma}$  was obtained from the variances and covariance of  $\hat{\alpha}$  and  $\hat{\mu}$  using the delta method (Efron and Tibshirani, 1993; Coles, 2001):

$$\text{var} \hat{\gamma} \approx [\text{var} \hat{\alpha} + \gamma^2 \text{var} \hat{\mu} - 2\gamma \text{cov}(\hat{\alpha}, \hat{\mu})] / \mu^2. \quad (2.17)$$

The unknown population parameters in the expressions for the variances were replaced by the weighted average  $\hat{\theta}_w$  of the at-site estimates.  $X^2$  was calculated for  $D = 1, 2, 4, 8, 12$  and 24 h.  $X^2$  has an asymptotic chi-square distribution under the null hypothesis  $\theta_1 = \theta_2 = \dots = \theta_{12}$  with 11 degrees of freedom, if there is no spatial dependence between the annual maxima. The asymptotic distribution has been verified in a Monte Carlo experiment with constant GEV parameters. From Table 2.2 it can be seen that the values of the  $X^2$ -statistic vary between 5.12 and 12.64, which is far below the critical value 19.68 for a test at the 5% level.

For each duration  $D$  the  $\hat{\theta}_i$ 's were also regressed on mean annual rainfall using weighted least squares (weights proportional to  $n_i$ ). Only for the location parameter of the 8- and 12-h annual maxima, the slope of the regression line was significant at the 5% level (Student's t-test, one-sided for  $\mu$ , two-sided for  $\gamma$  and  $\kappa$ ).

Since no geographical variation in the GEV parameters could be found and the spatial dependence between the stations' annual maxima is small, the time series from the 12 stations are concatenated to a single record of 514 years according to the station-year method.



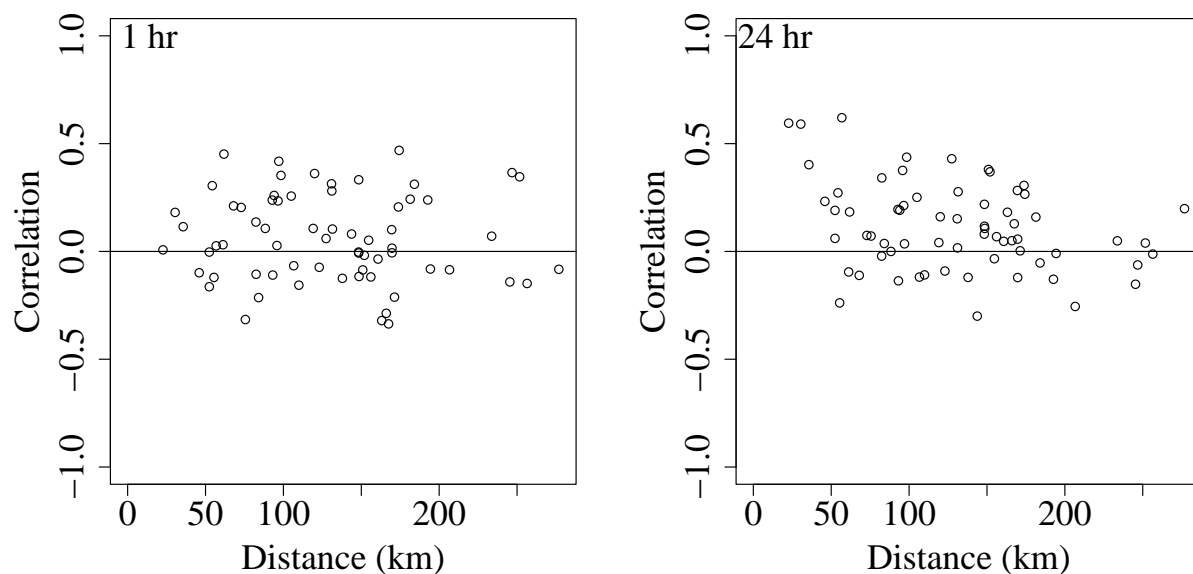


**Figure 2.3:** Cross correlations between the annual maxima of the 12 stations plotted against distance for durations of 1 (left) and 24 (right) hour.

## 2.4 Regional estimation and modelling of GEV parameters

### 2.4.1 Estimated GEV parameters for individual durations

For the time series of 514 years a GEV distribution (Eq. (2.1)) was fitted to the running annual maxima for durations of 1, 2, 4, 8, 12 and 24 h separately. Figure 2.4 shows that the GEV distribution gives a good fit for the 1-h annual maxima and that there is a weak tendency to overestimate large quantiles of the 24-h annual maxima. A GEV distribution fitted to 514 annual maxima should give a rather good estimate of large quantiles, particularly because  $\sigma^2(\hat{\kappa})$  is strongly reduced.

Running annual maxima, based on clock-hour rainfall sums, tend to be smaller than sliding annual maxima, defined as maxima obtained from continuous recording. Because clock-hour sums are used, the underestimation is small for durations of 4-24 h, however a conver-

**Table 2.2:** Values of the statistic  $X^2$  for testing equality of the GEV parameters  $\mu$ ,  $\gamma$  and  $\kappa$ .

$D$ (h)	$\mu$	$\gamma$	$\kappa$
1	9.82	10.32	8.82
2	7.45	9.44	10.18
4	5.51	8.98	10.93
8	7.83	7.07	11.61
12	9.35	7.36	9.16
24	12.64	9.01	5.12

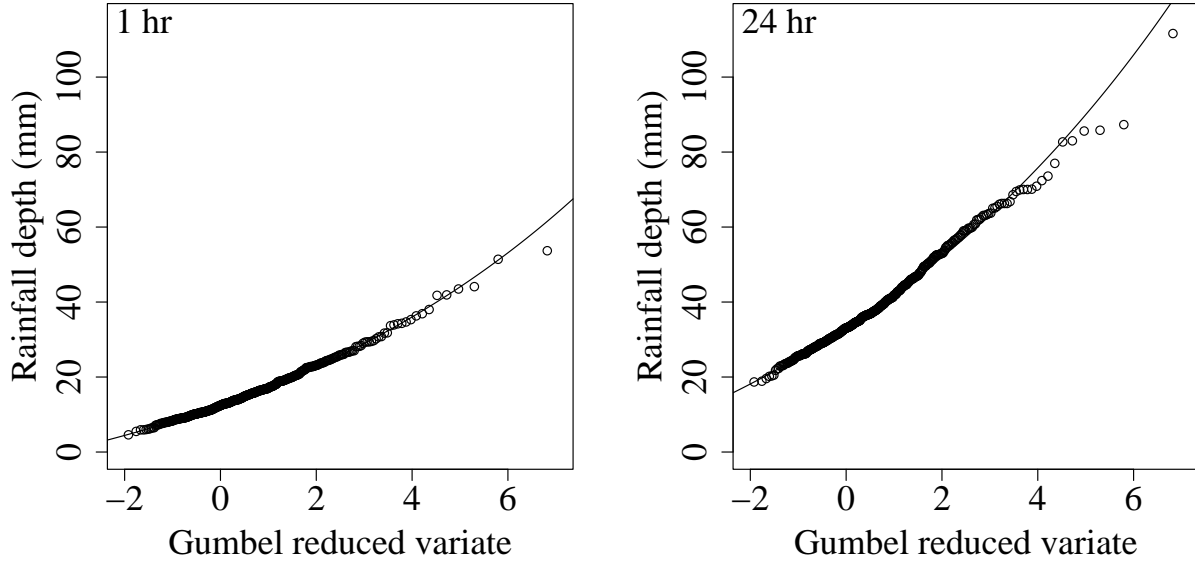


**Figure 2.4:** Gumbel probability plots with the GEV distribution fitted to annual 1-h (left) and 24-h (right) maxima. Dots are ordered annual maxima plotted with the Gringorten plotting position (Gringorten, 1963); lines represent GEV fits.

sion has to be applied for 1- and 2-h maxima. The sliding and running annual maxima of the 84-year record of De Bilt 1906-1990 (1945 excluded) were used for this conversion. For  $\mu$  and  $\gamma$  the estimates  $\hat{\mu}(D, 514)$  and  $\hat{\gamma}(D, 514)$  from the 514-year record were multiplied by the ratio of their estimates from the sliding and running annual maxima in the 84-year De Bilt record:

$$\hat{\mu}_{sl}(D, 514) = \frac{\hat{\mu}_{sl}(D, 84)}{\hat{\mu}(D, 84)} \hat{\mu}(D, 514) \text{ for } D = 1, 2 \text{ h}, \quad (2.18)$$

$$\hat{\gamma}_{sl}(D, 514) = \frac{\hat{\gamma}_{sl}(D, 84)}{\hat{\gamma}(D, 84)} \hat{\gamma}(D, 514) \text{ for } D = 1, 2 \text{ h}. \quad (2.19)$$

Parameter estimates with subscript *sl* refer to sliding annual maxima, the other estimates to running annual maxima. For the shape parameter  $\kappa$  no conversion was applied:

$$\hat{\kappa}_{sl}(D, 514) = \hat{\kappa}(D, 514) \text{ for } D = 1, 2 \text{ h}. \quad (2.20)$$

Eqs. (2.18) and (2.19) involve three separate GEV fits. Assuming a constant  $\kappa$  in these fits did not result in a satisfactory reduction of the standard deviations of  $\hat{\mu}_{sl}(D, 514)$  and  $\hat{\gamma}_{sl}(D, 514)$ . For  $\hat{\gamma}_{sl}(1, 514)$  there was even a small increase in standard deviation due to a change of sign of the correlation between  $\hat{\gamma}_{sl}(1, 84)/\hat{\gamma}(1, 84)$  and  $\hat{\gamma}(1, 514)$ .

For  $\hat{\mu}(D, 514)$  a conversion factor of 1.13 was found for  $D = 1$  and 1.04 for  $D = 2$  h. The value of 1.13 for  $D = 1$  h corresponds quite well with the correction factors (known as the Hershfield factor) 1.15 in the UK Flood Studies Report (NERC, 1975) and 1.13 in Hershfield (1961) for quantiles of clock-hour maxima. The conversion factors for  $\hat{\gamma}(D, 514)$  were

0.94 and 0.98 for  $D = 1$  and  $D = 2$  h, respectively. This implies that the correction factor for quantiles decreases with increasing return period. A disadvantage of the conversion of  $\hat{\gamma}(D, 514)$  is that it leads to a considerable increase in the standard deviation (see below).

Table 2.3 gives the estimated GEV parameters and their standard deviations. As expected  $\mu$  increases with increasing  $D$ . The parameter  $\gamma$  increases with decreasing duration. For this parameter the standard deviation is relatively high for  $D = 1$  and 2 h as a result of the use of a short record to adjust the estimate from the 514-year record. There seems to be no systematic variation of  $\kappa$  with  $D$ . This is in line with results of Gellens (2003) for Belgium. The values of  $\hat{\kappa}$  deviate 3.5 to 4 times their standard deviation from 0, so the Gumbel distribution would not be appropriate in modelling the annual rainfall maxima. Negative values of  $\kappa$  have been found in many other studies for  $D \leq 24$  h. E.g. Koutsoyiannis (2004) observed that  $\kappa = -0.15$  for daily annual maximum rainfall in different climatic zones of the USA, the UK and the Mediterranean.

In contrast to the use of asymptotic expressions as in Section 2.3.2, the standard deviations in Table 2.3 were based on the bootstrap. In the bootstrap method new samples (bootstrap samples) are generated by sampling with replacement from the original sample (Diaconis and Efron, 1983; Efron and Tibshirani, 1993). The standard deviations in Table 2.3 were derived from  $10^4$  bootstrap samples of 514 years. The algorithm is described in Appendix A. An advantage of the bootstrap is that it also applies to the estimated GEV parameters for sliding maxima in Eqs. (2.18) and (2.19). Zucchini and Adamson (1989) were the first who used the bootstrap to determine the uncertainty of design storms.

#### 2.4.2 Correlations of estimated GEV parameters

The bootstrap also provides for each GEV parameter the correlation coefficients between the estimates for different durations, which are needed for the assessment of the change of the parameter with duration. Table 2.4 shows correlation matrices of  $\hat{\mu}$ ,  $\hat{\gamma}$ , and  $\hat{\kappa}$  based on the same  $10^4$  bootstrap samples as in Section 2.4.1. Each correlation matrix consists of the correlations between the parameter estimates for different durations. These correlations are due to the dependence between the annual rainfall maxima for different durations. As a

**Table 2.3:** Estimated GEV parameters for  $D = 1$  (sl), 2 (sl), 4, 8, 12 and 24 h. Standard deviations are estimated with the bootstrap and given between brackets.

$D$ (h)	$\hat{\mu}$ (mm)	$\hat{\gamma}$	$\hat{\kappa}$
1	14.04 (0.34)	0.343 (0.019)	-0.127 (0.033)
2	16.79 (0.31)	0.325 (0.016)	-0.112 (0.032)
4	20.08 (0.30)	0.300 (0.011)	-0.102 (0.029)
8	24.27 (0.33)	0.271 (0.010)	-0.132 (0.033)
12	27.33 (0.36)	0.268 (0.010)	-0.121 (0.033)
24	33.08 (0.43)	0.253 (0.010)	-0.117 (0.030)

result correlations between neighbouring durations are quite large. Correlation coefficients for  $\hat{\kappa}$  and  $\hat{\gamma}$  are in general lower than for  $\hat{\mu}$ . Table 2.4 also provides the correlations between the estimates of different GEV parameters for the same duration and shows that especially  $\widehat{\text{corr}}(\hat{\mu}, \hat{\gamma})$  and  $\widehat{\text{corr}}(\hat{\kappa}, \hat{\gamma})$  are rather small.

### 2.4.3 GEV parameters as a function of duration

Relations of GEV parameters as a function of duration  $D$  (hour) are used to construct rainfall DDF curves. In Figure 2.5 GEV parameters are plotted against  $D$  for 1, 2, 4, 8, 12 and 24 h. For  $D = 1, 2$  h GEV parameters are calculated with Eqs. (2.18)-(2.20). It is shown that  $\gamma$  and the logarithm of  $\mu$  have a linear relationship with the logarithm of  $D$  for  $D = 1$ -24 h. There appears to be no systematic variation of  $\kappa$  with duration.

Figure 2.5 suggests the following regression model for the GEV parameters:

$$\hat{\theta} = \mathbf{X}\beta + \mathbf{e}, \quad (2.21)$$

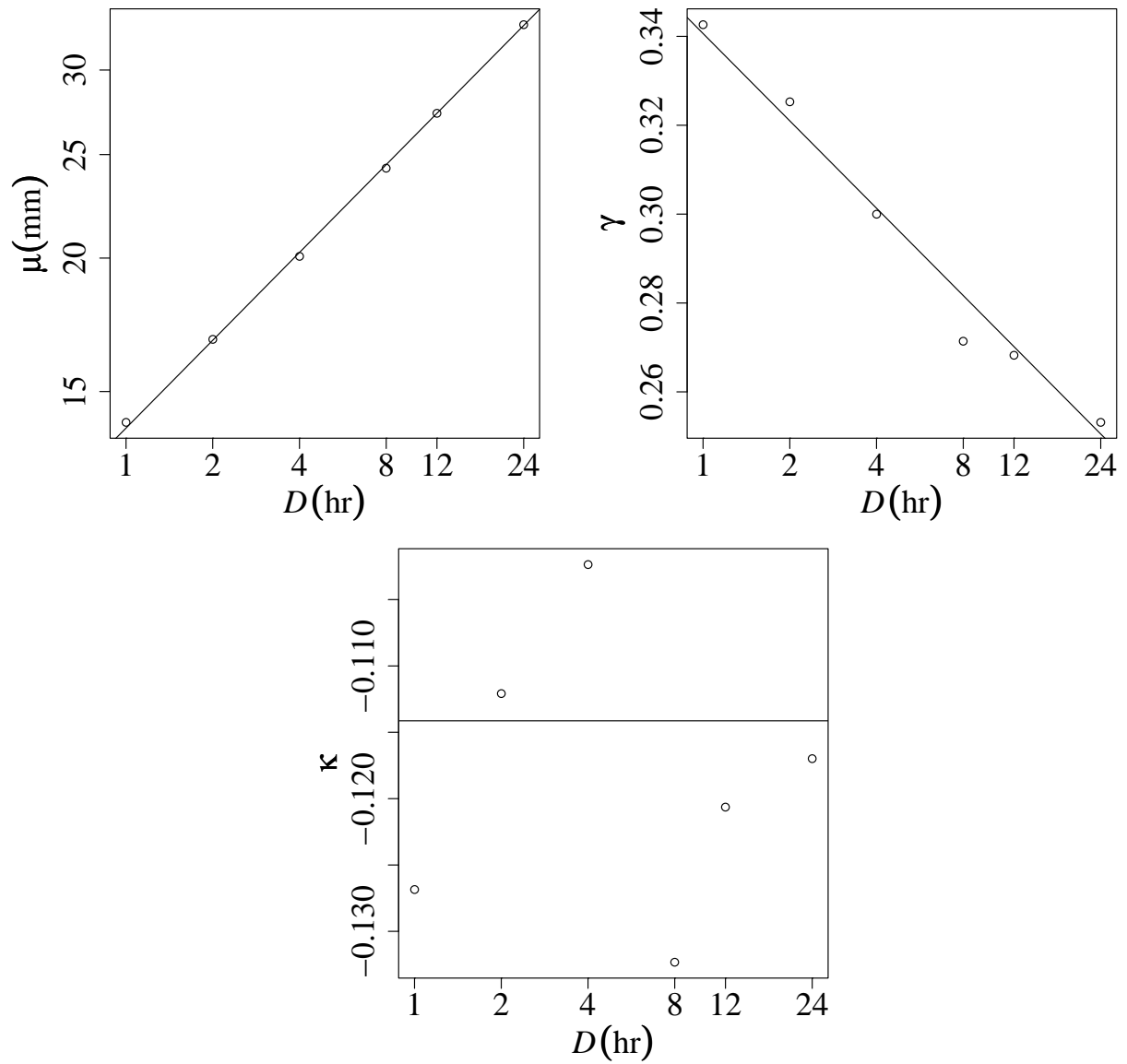
with  $\hat{\theta}$  the vector containing the estimated values of the GEV parameter  $\theta$  (or its logarithm) for the six durations  $D_1, \dots, D_6$ ,

**Table 2.4:** Correlation matrices of  $\hat{\mu}$ ,  $\hat{\gamma}$  and  $\hat{\kappa}$  for  $D$ -hour annual maximum rainfall depths and correlations between the estimates of different GEV parameters for the same duration, both estimated with the bootstrap.

$\hat{\mu}$							$\hat{\gamma}$						
$D$ (h)	1	2	4	8	12	24	$D$ (h)	1	2	4	8	12	24
1	1.00						1	1.00					
2	0.52	1.00					2	0.49	1.00				
4	0.47	0.79	1.00				4	0.39	0.62	1.00			
8	0.36	0.62	0.85	1.00			8	0.33	0.41	0.77	1.00		
12	0.30	0.52	0.72	0.91	1.00		12	0.22	0.35	0.63	0.86	1.00	
24	0.20	0.40	0.58	0.72	0.84	1.00	24	0.15	0.23	0.46	0.56	0.70	1.00

$\hat{\kappa}$									
$D$ (h)	1	2	4	8	12	24	$D$ (h)	$\hat{\mu}, \hat{\kappa}$	$\hat{\mu}, \hat{\gamma}$
1	1.00						1	0.22	-0.12
2	0.73	1.00					2	0.28	0.08
4	0.49	0.75	1.00				4	0.36	0.18
8	0.26	0.35	0.61	1.00			8	0.32	0.20
12	0.21	0.25	0.46	0.88	1.00		12	0.27	0.13
24	0.08	0.09	0.25	0.62	0.76	1.00	24	0.38	0.31



**Figure 2.5:** GEV parameters plotted against duration  $D$ . The solid lines represent the generalized least squares fits to the estimated GEV parameters.

$$\mathbf{X} = \begin{pmatrix} 1 & \ln D_1 \\ \cdot & \cdot \\ 1 & \ln D_6 \end{pmatrix},$$

$$\boldsymbol{\beta} = \begin{pmatrix} a \\ b \end{pmatrix},$$

and  $\mathbf{e}$  a vector of random disturbances. The components of  $\mathbf{e}$  are correlated because of the correlation between the estimated GEV parameters for different durations. To account for

this correlation, the method of generalized least squares was chosen to estimate the regression coefficients  $a$  and  $b$ . The generalized least squares estimate  $\hat{\beta}_{GLS}$  of  $\beta$  is given by:

$$\hat{\beta}_{GLS} = (\mathbf{X}^T \mathbf{C}^{-1} \mathbf{X})^{-1} \mathbf{X}^T \mathbf{C}^{-1} \hat{\theta} = \begin{pmatrix} \hat{a} \\ \hat{b} \end{pmatrix}, \quad (2.22)$$

with  $\mathbf{C}$  the covariance matrix of  $\hat{\theta}$ . For  $\hat{\gamma}$  and  $\hat{\kappa}$  the estimated correlation coefficients are given in Table 2.4; for  $\ln \hat{\mu}$  the estimated correlation coefficients are almost the same as those for  $\hat{\mu}$ . Because of the long time series, these correlation estimates are relatively accurate. Steindinger and Tasker (1985) compared generalized least squares regression with ordinary and weighted least squares in a regional analysis of streamflow statistics. Madsen et al. (2002) applied generalized least squares in a regional frequency analysis of rainfall to account for intersite dependence. The covariance matrix of  $\hat{\beta}_{GLS}$  is given by:

$$\text{cov}(\hat{\beta}_{GLS}) = (\mathbf{X}^T \mathbf{C}^{-1} \mathbf{X})^{-1}. \quad (2.23)$$

This can be compared with the covariance matrix of the ordinary least squares estimate  $\hat{\beta}_{OLS}$ :

$$\text{cov}(\hat{\beta}_{OLS}) = (\mathbf{X}^T \mathbf{X})^{-1} \mathbf{X}^T \mathbf{C} \mathbf{X} (\mathbf{X}^T \mathbf{X})^{-1}. \quad (2.24)$$

The goodness-of-fit can be tested with the statistic:

$$X^2 = (\hat{\theta} - \hat{\theta}_{GLS})^T \mathbf{C}^{-1} (\hat{\theta} - \hat{\theta}_{GLS}), \quad (2.25)$$

where  $\hat{\theta}_{GLS} = \mathbf{X} \hat{\beta}_{GLS}$ . In the case of an adequate fit,  $X^2$  is approximately chi-square distributed with  $n - p$  degrees of freedom, with  $n = 6$  the number of durations and  $p$  the number of regression coefficients. Eq. (2.25) generalizes Eq. (2.15) in two directions: it allows for dependence between the estimated GEV parameters, and it allows for the inclusion of covariates.

Table 2.5 shows the estimated regression coefficients with their standard deviations. For  $\kappa$  the estimate of the slope  $b$  differs no more from zero than  $0.46\sigma(\hat{b})$ . This confirms that  $\kappa$  may be considered to be constant. Re-estimating  $a$  yielded  $\hat{\kappa}_{GLS} = \hat{a} = -0.114$ , which is given by the solid line in Figure 2.5. For the other two GEV parameters there is a significant dependence on duration. The values of the  $X^2$ -statistic in Table 2.5 are well below the critical values for a test at the 5% level. So there is no evidence of lack-of-fit.

**Table 2.5:** Results of the regression of GEV parameters.

GEV parameter	$\hat{a}$	$\sigma(\hat{a})$	$\hat{b}$	$\sigma(\hat{b})$	$X^2$
$\ln \mu$	2.629	0.019	0.273	0.006	3.10
$\gamma$	0.341	0.015	-0.028	0.005	4.07
$\kappa$	-0.125	0.032	0.006	0.013	2.38
$\kappa$	-0.114	0.021	-	-	2.60

For  $\sigma(\hat{\kappa}_{GLS})$  a value of 0.021 was found, which is considerably smaller than the standard deviation of the  $\hat{\kappa}$ 's for the individual durations in Table 2.3. The ordinary least squares estimate of  $\kappa$  is simply the average -0.119 of the six estimates for the individual durations. The standard deviation of this average, 0.023, is somewhat larger than  $\sigma(\hat{\kappa}_{GLS})$ . This confirms the conclusion in Buishand (1993) that the reduction in standard deviation due to the use of generalized least squares is small in the case of rainfall depth-duration-frequency analysis. The correlation between the estimated GEV parameters may, however, not be ignored if standard deviations or goodness-of-fit are of interest.

The systematic change of  $\gamma$  with duration implies that the dependence of quantiles on  $T$  and  $D$  cannot be separated in a function of  $D$  and a function of  $T$ , as was done in Koutsoyiannis et al. (1998). Another consequence is that simple scaling does not apply as observed by Menabde et al. (1999) for Melbourne (Australia) and Warmbaths (South Africa) and Borga et al. (2005) for the Trentino province (Italy). Both require that the coefficient of variation is constant, which is not the case if  $\gamma$  varies with duration.

## 2.5 Construction of rainfall DDF curves and their uncertainties

### 2.5.1 Derivation of DDF curves

Now that the GEV parameters are described as a function of  $D$ , rainfall DDF curves are constructed by substituting these relationships into Eq. (2.3), so that the DDF curves are given by:

$$\hat{x}(T) = \exp(\hat{a}_\mu + \hat{b}_\mu \ln D) \times \left( 1 + (\hat{a}_\gamma + \hat{b}_\gamma \ln D) \frac{\{1 - [-\ln(1 - T^{-1})]^{\hat{\kappa}_{GLS}}\}}{\hat{\kappa}_{GLS}} \right), \quad (2.26)$$

where  $\hat{a}_\mu = 2.629$ ,  $\hat{b}_\mu = 0.273$ ,  $\hat{a}_\gamma = 0.341$ ,  $\hat{b}_\gamma = -0.028$  and  $\hat{\kappa}_{GLS} = -0.114$ .

By choosing a return period  $T$ , the rainfall depth  $x$  (mm) can be plotted as a function of duration  $D$  using Eq. (2.26). In Section 2.4.3 it was noticed that  $\sigma(\hat{\kappa})$  is considerably reduced if  $\hat{\kappa}$  is based on the maxima for all six durations. Large quantiles are then more accurately estimated compared to fitting a GEV distribution only to the maxima for the duration of interest. Figure 2.6 presents the DDF curves for  $T = 100$  and 1000 years. The curves show a strong increase of  $x$  with  $D$ , e.g. for  $T = 1000$  years rainfall depths range from 64 to 120 mm for  $D = 1$ -24 h.

### 2.5.2 Modelling uncertainty in DDF curves

Uncertainty in DDF curves is usually disregarded, while it should be considered, e.g. in the design of hydraulic structures. Here the bootstrap was applied to assess this uncertainty. This method considers only the uncertainty due to the estimation of the GEV parameters, i.e. sampling errors. For each of the  $10^4$  bootstrap samples from Section 2.4.1 the relations between the GEV parameters and duration were re-estimated using generalized least squares, so that  $10^4$  DDF curves could be constructed. For each DDF curve the rainfall depths were

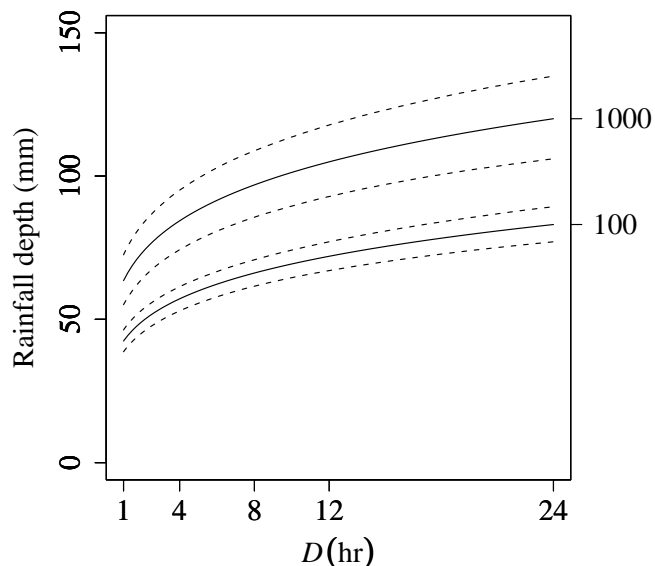


**Figure 2.6:** Rainfall DDF curves (solid lines) and 95%-confidence bands (dashed lines) for return periods of 100 and 1000 years (indicated on the right axis).

derived for durations between 1 and 24 h in steps of 1 min. Subsequently, for each of these durations the  $10^4$  depths were ranked in increasing order and the 250th and 9750th values were determined. Next, these values were plotted and formed the 95%-confidence bands. For return periods of 100 and 1000 years, Figure 2.6 shows the DDF curves and their 95%-confidence bands. For  $T = 1000$  years the confidence interval ranges from 55-73 mm for  $D = 1$  h to 106-135 mm for  $D = 24$  h, thus showing a rather large uncertainty, despite the fact that the DDF curves are based on a 514-year record. For longer  $T$  uncertainty increases substantially.

It is found that the bootstrap distribution of the estimated quantiles can be described by a lognormal distribution. The parameters  $\xi$  and  $\sigma$  of the lognormal distribution, i.e. the mean and standard deviation of the underlying normal distribution, are modelled as a function of  $D$  and  $T$ . The parameter  $\xi$  is well described by the natural logarithm of the estimated quantiles from the DDF curve. Using  $10^4$  bootstrap samples for six durations and seven return periods, namely from every combination of  $D = 1, 2, 4, 8, 12$  and 24 h and  $T = 10, 20, 50, 100, 200, 500$  and 1000 years, the parameter  $\sigma$  is modelled as:

$$\sigma = -0.0042 + 0.0103D^{-1} + 0.0091 \ln T. \quad (2.27)$$

The regression coefficients were estimated with ordinary least squares. Figure 2.7 shows the DDF curves for  $T = 100$  and 1000 years. The lognormal probability density functions which describe the uncertainties in these curves are plotted for  $D = 1$  and 12 h.



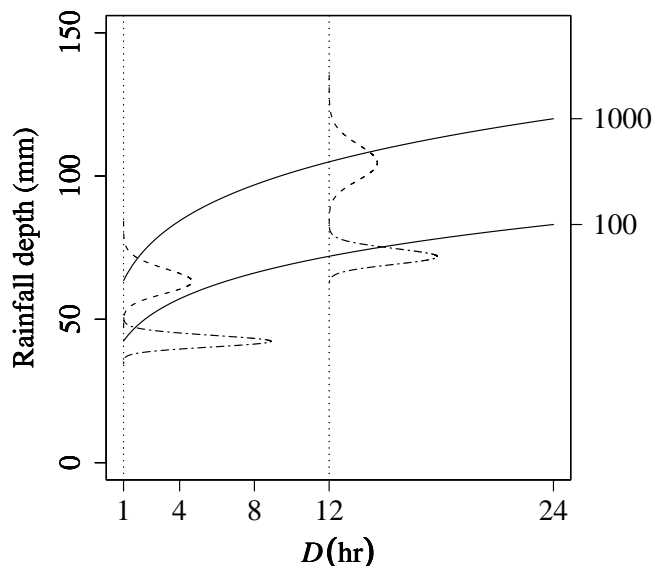


**Figure 2.7:** Rainfall DDF curves (solid lines) for  $T = 100$  and  $1000$  years and lognormal probability density functions (dashed lines) which describe the uncertainties in the DDF curves for  $D = 1$  and  $12$  h.

## 2.6 Conclusions

Extreme rainfall in the Netherlands for durations between 1 h and 24 h was studied. Since regional variability in extreme rainfall statistics could not be found and spatial dependence between extreme rainfall amounts appeared to be small, a record of 514 annual maxima was constructed according to the station-year method. GEV parameters of this time series were estimated with the method of L-moments. Standard deviations and correlations of estimated GEV parameters were obtained with the bootstrap. To take into account the correlation between estimated GEV parameters for different durations, the generalized least squares method was used to describe the variation of these parameters as a function of duration. The relations were used to construct rainfall DDF curves. Finally, uncertainties in DDF curves, due to sampling variability, were quantified with the bootstrap and described with a lognormal distribution.

It was found that the shape parameter  $\kappa$  of the GEV distribution does not change with duration. For the parameter  $\gamma$  there is a significant increase with decreasing duration. As a consequence, the coefficient of variation increases with decreasing duration. This implies that simple scaling does not hold.

A 84-year record of sliding 1- and 2-h annual maxima from De Bilt was used to convert the estimated GEV parameters from the 514-year hourly station-year record. For the parameter  $\gamma$  a correction factor  $< 1$  was found which implies that the correction for quantiles depends on return period. This may be related to the change of  $\gamma$  with duration.

In the generalized least squares method used in this chapter to fit relationships between GEV parameters and duration, the fit for one GEV parameter does not affect the fit for the other two parameters. This may be justified by the fact that the correlation between the estimated GEV parameters is small. As an alternative, re-estimation of the parameters  $\mu$  and  $\gamma$  in the 514-year record was explored assuming  $\kappa = \hat{\kappa}_{GLS}$ . The changes were very small.

Possible inhomogeneities in the rainfall records due to changed measurement methods, gauge types or locations were not considered. Further, annual maxima were assumed to be stationary. Smits et al. (2004) found for De Bilt that the trends in the extremes are relatively small.

Usually uncertainties in rainfall DDF curves are disregarded, so that risks can be underestimated. An innovative aspect of this chapter is that uncertainty in DDF curves due to sampling variability is taken into account. Other sources of uncertainty were not considered, such as measurement errors and uncertainty about the choice of the distribution.

A situation that there is no regional variability in all GEV parameters will seldom be met in other parts of the world. In addition, there might be spatial correlation between annual maximum rainfalls. The methods used here can be adapted if regional variability in GEV parameters is present. Resampling from the  $N$  years providing rainfall data, as e.g. in Faulkner and Jones (1999), rather than resampling from all station-years, should be considered. Some care is needed in situations where the covariance matrices of the estimated GEV parameters vary over the region of interest.

## Acknowledgements

The authors acknowledge the comments given by Demetris Koutsoyiannis and an anonymous reviewer, which certainly improved the chapter.

## Chapter 3

---

# Derivation of a 10-year radar-based climatology of rainfall<sup>1</sup>

### Abstract

Weather radars give quantitative precipitation estimates over large areas with high spatial and temporal resolutions not achieved by conventional rain gauge networks. Therefore, the derivation and analysis of a radar-based precipitation climatology are highly relevant. For that purpose, radar reflectivity data were obtained from two C-band Doppler weather radars covering the land surface of the Netherlands ( $\approx 3.55 \times 10^4 \text{ km}^2$ ). From these reflectivities, 10 yr of radar rainfall depths were constructed for durations  $D$  of 1, 2, 4, 8, 12 and 24 h with a spatial resolution of 2.4 km and a data availability of approximately 80%. Different methods are compared for adjusting the bias in the radar precipitation depths. Using a dense manual gauge network, a vertical profile of reflectivity (VPR) and a spatial adjustment are applied separately to 24-h (0800-0800 UTC) unadjusted radar-based precipitation depths. Further, an automatic rain gauge network is employed to perform a mean-field bias adjustment to unadjusted 1-h rainfall depths. A new adjustment method is developed (referred to as MFBS) that combines the hourly mean-field bias and the daily spatial adjustment methods. The record of VPR gradients, obtained from the VPR adjustment, reveals a seasonal cycle that can be related to the type of precipitation. A verification with automatic ( $D \leq 24 \text{ h}$ ) and manual ( $D = 24 \text{ h}$ ) rain gauge networks demonstrates that the adjustments remove the systematic underestimation of precipitation by radar. The MFBS adjustment gives the best verification results and reduces the residual (radar minus rain gauge depth) standard deviation considerably. The adjusted radar data set is used to obtain exceedance probabilities, maximum rainfall depths, mean annual rainfall frequencies and spatial correlations. Such a radar rainfall climatology is potentially valuable for the improvement of rainfall parameterization in weather and climate models and the design of hydraulic structures.

---

<sup>1</sup>*Journal of Applied Meteorology and Climatology*, 2009, **48**, pp 1448-1463 by Aart Overeem, Iwan Holleman and Adri Buishand.

### 3.1 Introduction

Weather radars are widely used in real-time quantitative precipitation estimation (QPE) over large areas. For example, in Europe over 170 weather radars (mainly C band) are operational. A weather radar transmits electromagnetic waves into the atmosphere and receives the backscattered waves from precipitation particles as echo powers, which are converted into rainfall intensities. A detailed discussion of QPE with radar is given by Rinehart (2004). In contrast to most rain gauge networks, weather radars measure rainfall intensities with high spatial and temporal resolutions. In addition to the operational use of radar data in nowcasting of precipitation, numerical weather prediction models and water management, radar data also become valuable for climatological applications. For example, a radar rainfall climatology could be employed to calculate the probabilities of extreme rainfall used for design purposes in water management.

However, QPE with radar is hampered by a variety of errors, of which the most important for C-band radar at midlatitudes are attenuation of the radar beam as a result of strong precipitation or a wet radome and those errors caused by a nonuniform vertical profile of reflectivity (VPR) or variability of the drop size distribution. Especially at long ranges from the radar, rainfall intensity can be underestimated because of incomplete beam filling or partial overshooting. Overshooting is caused by the increasing height of observation, which is owing to the earth's curvature and the beam elevation angle. In this case precipitation is underestimated if the radar reflectivity decreases with height. Some other errors related to QPE with radar are occultation, bright band effects, hardware calibration errors and anomalous propagation ground clutter. For more details on these and other errors, see, for example, Joss and Waldvogel (1990), Doviak and Zrnić (1993) or Michelson et al. (2005a).

Radars usually provide a detailed description of the spatial distribution of rainfall intensity whereas rain gauges are considered to produce accurate point measurements; therefore, rain gauges have been used frequently to improve the quality of QPE with radar by using, for instance, a mean-field bias adjustment (Steiner et al., 1999; Borga et al., 2002; Holleman, 2007), a spatial adjustment (Brandes, 1975; Michelson and Koistinen, 2000), or a probability-matching method (Rosenfeld et al., 1993; Rosenfeld and Amitai, 1998). To improve the quality of QPE at long ranges, Gabella et al. (2001) used a multiple regression with rain gauges and Vignal and Krajewski (2001) applied a VPR correction by estimating a mean VPR from reflectivity profiles close to the radar. Germann and Joss (2002) utilized a profile-correction scheme for operational use to extrapolate radar-based precipitation to the surface. Furthermore, Michelson et al. (2005b) describe a physically based procedure, called "Down-to-Earth", that combines radar measurements with data from a numerical weather prediction model and an analysis system.

Because of the possible errors involved in QPE with radar, an independent verification with rain gauges or disdrometers is necessary to assess the quality of a radar data set. Studies

such as Germann et al. (2006) and Holleman (2007) show that adjustment with rain gauges considerably improves the quality of long-term radar-based rainfall accumulations. For Switzerland, Germann et al. (2006) pursued an extensive 8-yr verification of radar-derived precipitation using rain gauges. Holleman (2007) conducted a verification of radar-based precipitation estimates for the Netherlands, applying a 6-yr data set.

Some other studies utilizing long-term radar data sets are Croft and Shulman (1989), Baeck and Smith (1995), Joss and Lee (1995), Young et al. (2000), Vignal and Krajewski (2001), Borga et al. (2002), Nzeukou et al. (2006) and Xie et al. (2006). Nelson et al. (2003) constructed a 5-yr data set of hourly rainfall accumulations for the Mississippi River Basin. Allen and DeGaetano (2005a) estimated return intervals for extreme areal precipitation amounts using a 5-yr data set of 24-h accumulated rainfall for New Jersey and North Carolina. Notwithstanding these efforts, the number of studies employing at least a few years of subdaily radar rainfall accumulations remains relatively limited. Furthermore, radar rainfall intensities are comparatively often obtained from a small number of reflectivity classes. Also, little research has been pursued in the field of radar-based rainfall climatologies of, for instance, exceedance probabilities or spatial correlations.

This chapter addresses the adjustment, verification, and climatological analysis of a 10-yr radar data set for the Netherlands of accumulated precipitation for durations of 1, 2, 4, 8, 12, and 24 h. Precipitation depths are derived from radar reflectivities quantized in levels of 0.5 dBZ, resulting in a high-resolution data set unmatched by many other studies. The whole radar data set was reprocessed using the same adjustment procedures, in contrast to several other studies that used adjusted radar data from an operational archive. The data set is corrected for occultation and anomalous-propagation ground clutter. Different adjustment methods are applied to the radar data and compared. Using daily (0800-0800 UTC) rainfall accumulations from manual rain gauges, a VPR adjustment (which includes a bias adjustment) and a spatial adjustment are conducted separately. The daily spatial adjustment factor fields are also applied to the 1-h unadjusted accumulations. Automatic rain gauges are utilized to apply a mean-field bias adjustment to unadjusted 1-h rainfall depths. Finally, a new adjustment method is developed that merges the daily spatial and the hourly mean-field bias adjustment methods. An elaborate verification with a manual and an automatic rain gauge network assesses the quality of the adjusted accumulations. Based on these accumulations, rainfall climatologies of exceedance probabilities, maximum rainfall depths, mean annual rainfall frequencies, and spatial correlations are derived.

This chapter is organized as follows. Section 3.2 gives a description of the radar and rain gauge data. In Section 3.3, a data set of adjusted radar-derived rainfall accumulations is constructed, which is then verified against rain gauges in Section 3.4. Section 3.5 gives long-term radar rainfall statistics based on the adjusted radar accumulations. The chapter ends with a discussion and conclusions.

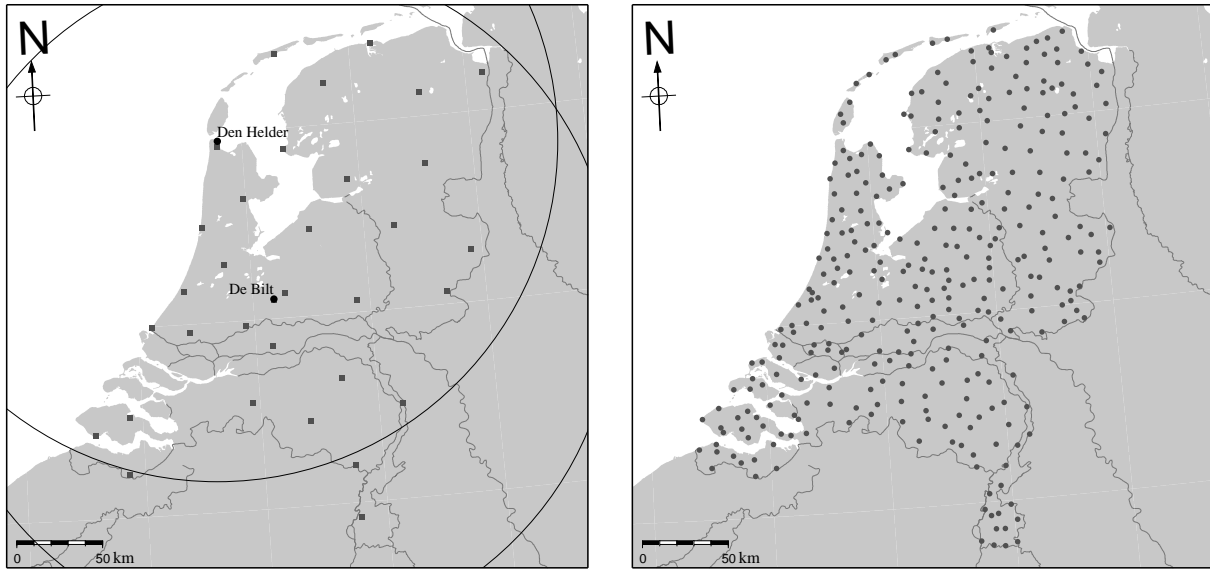


**Figure 3.1:** Maps of the Netherlands with (left) the locations of the weather radars in De Bilt and Den Helder, their 200-km range (circles), the 33 automatic rain gauges (squares), and (right) the locations of the 326 manual rain gauges.

## 3.2 Radar and rain gauge data

### 3.2.1 Radar data

Radar reflectivity data were obtained from the two C-band Doppler weather radars in the Netherlands, which are operated by KNMI and located in De Bilt ( $52.10^{\circ}$  N,  $5.18^{\circ}$  E, 44 m MSL) and Den Helder ( $52.96^{\circ}$  N,  $4.79^{\circ}$  E, 51 m MSL) (see Figure 3.1). Every 5 min the radars, which have a 3-dB beamwidth of  $1^{\circ}$ , performed four azimuthal scans of  $360^{\circ}$  around a vertical axis at beam elevation angles of  $0.3^{\circ}$ ,  $1.1^{\circ}$ ,  $2.0^{\circ}$  and  $3.0^{\circ}$ . More technical characteristics of the radars are listed in Table 3.1.

From 1998 to 2007, horizontal cross sections of radar reflectivity at constant altitude, called

**Table 3.1:** Technical characteristics of the single-polarization Selex (Gematronik) METEOR 360 AC radars.

Characteristic	De Bilt	Den Helder
Wavelength (cm)	5.293	5.163
Pulse repetition frequency (Hz)	250	250
Peak power (kW)	268	264
Pulse duration ( $\mu$ s)	2.02	2.04
3-dB beamwidth ( $^{\circ}$ )	1	1
Antenna rotation speed ( $^{\circ}$ s $^{-1}$ )	18	18
No. of samples per range (km $^{-1}$ )	4	4

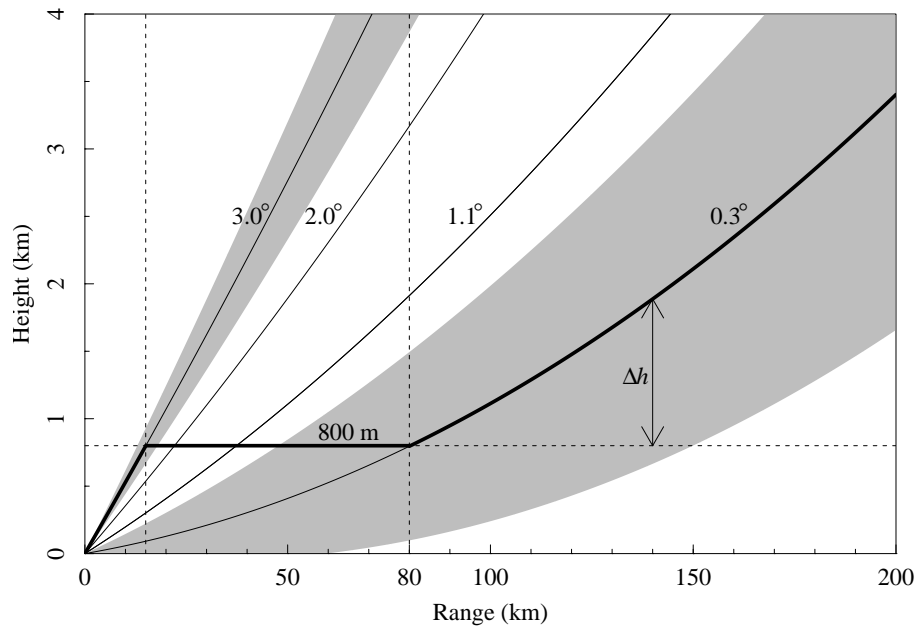


**Figure 3.2:** Volume coverage pattern displaying the height of the four beam elevations with respect to antenna level as a function of range from the radar. The thick line denotes the pseudo CAPPI image, the gray-shaded areas indicate the 1°-beam for the lowest and highest elevation.

pseudo constant-altitude plan position indicators (pseudo CAPPI), are available with a temporal resolution of 5 min. These pseudo CAPPI images contain 8-bit reflectivity values, quantized in levels of 0.5 dBZ, at a 2.4-km horizontal resolution. Figure 3.2 displays the volume coverage pattern with the height of the four elevations as a function of range from the radar, where the thick line denotes the pseudo CAPPI. The figure demonstrates that for the lowest elevation the 3-dB beam (shown as a gray-shaded area) partially intersects the surface for distances up to 60 km from the radar, whereas this does not occur for the highest elevation. Therefore, at short range the highest elevation was used to reduce the risk of ground clutter and beam blockage near the radar. For the domain 15-80 km from the radar, the pseudo CAPPI was constructed by bilinear interpolation of the reflectivity values (dBZ) of the nearest elevations below and above the 800-m height. Only the reflectivity values of the lowest elevation were used for the area located 80-200 km from the radar. As appears from Figure 3.2, the 800-m level is within the 3-dB beamwidth of the lowest elevation up to a range of 150 km.

Ground clutter and anomalous-propagation ground clutter were subsequently removed from the pseudo CAPPI images using the procedure of Wessels and Beekhuis (1995), also described in Holleman and Beekhuis (2005). Reflectivities below 7 dBZ ( $\approx 0.1 \text{ mm h}^{-1}$ ) were not converted to rainfall intensities to avoid the accumulation of noise. Reflectivities above 55 dBZ ( $\approx 100 \text{ mm h}^{-1}$ ) were set to 55 dBZ to suppress the influence of echoes induced by

hail or strong residual clutter. Next, the reflectivities  $Z$  ( $\text{mm}^6 \text{m}^{-3}$ ) of the pseudo CAPPI images were converted to rainfall intensities  $R$  ( $\text{mm h}^{-1}$ ) with the fixed  $Z$ - $R$  relationship (Marshall et al., 1955), independent of season or type of rain,

$$Z = 200R^{1.6}, \quad (3.1)$$

assuming an exponential drop size distribution, Rayleigh scattering and a power law for the terminal fall speed of drops as a function of diameter. With 0.5-dBZ classes this resulted in 97 possible levels of rainfall intensities ranging from 0.1 to 100  $\text{mm h}^{-1}$ . One-hour rainfall accumulations were constructed from the 5-min rainfall intensities if at least 10 images (minimum availability of 83.3%) were available. Local outliers caused by accumulated residual clutter were removed from the accumulations using a five-pixel median filter on nearest-neighbor pixels. If one or two images were missing, the 1-hour accumulated rainfall was scaled by the fraction of available images. Because the quality of QPE with radar diminishes considerably at long ranges from the radar, the range of the radar accumulation images was limited to 200 km. Furthermore, spurious echoes within a radius of 15 km from the radar, which mainly originate from transmitter noise and sidelobe clutter, were reduced by following the truncation procedure described in Holleman (2007). The radar in Den Helder overestimated rainfall intensities for the period from 1998 to January 2001 due to an elevation bias. Because of this, the data set of the Den Helder radar was restricted to the period from February 2001 to 2007. Note that the De Bilt radar already covers the entire land surface of the Netherlands ( $\approx 3.55 \times 10^4 \text{ km}^2$ ), as is indicated by the 200-km-range circle in Figure 3.1.

The 1-h depths of the Den Helder radar were only selected if the corresponding 1-h accumulations of the De Bilt radar were available. Next, only those 1-h depths were selected for which the data availability of the corresponding 24-h (0800-0800 UTC) period was at least 83.3%. This resulted in a data set with a mean annual data availability of 5-min composites ranging from 61% to 95%, on average 82% (Table 3.2). Before 2003, the archiving was not performed on a routine basis, causing a lower data availability. The percentage of available images varies from 82% for the 1-h to 79% for the 24-h composited depths. Thus, the effective length of the data set of composites is approximately 8 yr, of which 5.5 yr are also based on the data set from the Den Helder radar.

### 3.2.2 Rain gauge networks

The Royal Netherlands Meteorological Institute (KNMI) maintains two rain gauge networks: an automatic network of 33 rain gauges ( $\approx 1$  station per 1000  $\text{km}^2$ ) and a manual network of 326 rain gauges ( $\approx 1$  station per 100  $\text{km}^2$ ). Figure 3.1 shows the locations of the stations of the two networks. The electronic rain gauges measure the precipitation depth using the displacement of a float placed in a reservoir, and most of them are surrounded by a wall to prevent measurement errors induced by turbulence. Volunteers measure the 24-h precipitation depth from the manual rain gauges at 0800 UTC. The manual gauge has a height



of 0.40 m. The gauges are not particularly suited to measure solid precipitation, although the automatic gauges have a heating device. However, this type of precipitation constitutes a very small part of mean annual precipitation in the Netherlands. Missing values in the gauge records have been routinely supplemented as much as possible, resulting in a 100% data availability for most gauges. All data have been quality controlled by KNMI staff. Detailed information on the rain gauge networks can be found in KNMI (2000) and Wauben (2006).

### 3.3 Adjustment of radar-based rainfall accumulations

#### 3.3.1 Correction for occultation per radar

Although the Netherlands is a flat country, with only small areas that are 50 m above MSL, beam blockage is a serious problem because of the presence of tall buildings in the vicinity of the radars. This results in an underestimation of rainfall intensities for certain azimuth sectors, as is illustrated by the January 2004 precipitation sum for the De Bilt radar in Figure 3.3 (a, page 56) in, for example, the area indicated by the white box. A correction for this occultation is performed on the data set of 1-h radar accumulations. First, the accumulated rainfall is averaged over the 200-km range for each 1°-azimuth sector for every year and radar separately. The azimuth sectors that show a strong decrease in annual rainfall sums with respect to adjacent azimuth sectors are identified. Most of these sectors can be related to the location of major buildings. Next, the azimuth sectors are divided into 200 range bins of 1 km, which contain values of 1-h rainfall depths. For an occulted azimuth sector, each range bin value is replaced by the linearly interpolated value of the range bins at the same range from the nearest left and right nonblocked azimuth sectors. On average, 9 (Den Helder radar) and 24 (De Bilt radar) out of 360 azimuth sectors were corrected. Figure 3.3 (b, page 56) shows the January 2004 precipitation depth, corrected for occultation. The decrease in accumulated precipitation near the radars is caused by the truncation procedure used to reduce spurious echoes close to the radar.

#### 3.3.2 Daily VPR and bias adjustment per radar (VPR adjustment)

For the Netherlands, Holleman (2007) found that a mean-field bias adjustment considerably increases the quality of QPE from radar observations; however, it is less successful at long

**Table 3.2:** Average annual data availability (%) of 5-min composites that passed certain selection criteria for data availability.

Year	Data availability (%)	Year	Data availability (%)
1998	79.2	2003	78.0
1999	85.3	2004	95.3
2000	74.6	2005	90.8
2001	84.8	2006	87.1
2002	61.4	2007	86.3

ranges. In this section, a VPR adjustment is proposed that also improves the quality of rainfall accumulations far from the radar. The starting point is the unadjusted (raw) radar data. For example, Figure 3.3 (page 56) shows a clear underestimation of the January 2004 precipitation depth for the raw radar composite (d) relative to the interpolated depths from the manual rain gauge network (c), especially near the borders of the Netherlands. This is typical for the months November - March, when shallow stratiform precipitation dominates, so that partial overshooting occurs frequently. The depths from the manual rain gauge network were interpolated with continuous curvature splines in tension (Smith and Wessel, 1990).

The VPR adjustment method uses manual rain gauges to remove the bias and to adjust for reflectivity values that change with height. For each radar-gauge pair with sufficient rainfall, the ratio of the accumulated daily (0800-0800 UTC) rainfall from the rain gauge and radar pixel is calculated. An adjustment “factor”  $f_{raw}$  in decibels is defined as

$$f_{raw}(i_n, j_n) = 10 \times 10 \log \frac{G(i_n, j_n)}{R_{raw}(i_n, j_n)}, \quad (3.2)$$

where  $G(i_n, j_n)$  is the amount of rain for gauge  $n$ ,  $R_{raw}(i_n, j_n)$  is the amount of rain for the corresponding radar pixel, and  $(i_n, j_n)$  are the image coordinates of rain gauge  $n$ . The logarithm is used here because the distribution of  $f_{raw}$  is closer to the normal distribution than that of the ratio  $G/R_{raw}$  (Koistinen and Puhakka, 1981). Further, a linear regression on the logarithms leads to a multiplicative adjustment factor on the original scale. Only pairs within 15-200 km of the radar and for which  $R_{raw}$  and  $G$  are at least 0.5 mm are taken into account and called “valid”. The following linear regression equation is used to model  $f_{raw}$  as a function of the height  $\Delta h$  of the lowest beam elevation above the 800-m pseudo CAPPI height:

$$f_{raw}(i_n, j_n) = -b - a \times \Delta h(i_n, j_n) + e(i_n, j_n), \quad (3.3)$$

where  $e(i_n, j_n)$  denotes a residual. The VPR gradient  $a$  (dBR km<sup>-1</sup>) and the bias  $b$  (dBR) are estimated by ordinary least squares, see, e.g., Chapter 15 in Press et al. (1992). The VPR adjustment factor (dBR) is defined as

$$F_{VPR}(i, j) = -b - a \times \Delta h(i, j), \quad (3.4)$$

where  $(i, j)$  are the pixel-image coordinates. The lowest elevation reaches the 800-m height ( $\Delta h = 0$ ) at a range of 80 km, as shown in Figure 3.2. If the number of valid pairs in the region where  $\Delta h > 0$  is less than 20, then only a constant bias adjustment is conducted. In that case,  $a$  is set a priori to zero, so that only  $b$  is estimated. If the region 15-200 km from the radar contains less than 10 valid pairs,  $F_{VPR}$  is set to zero.

Next, for each pixel in the radar domain the  $F_{VPR}$  relation (Eq. (3.4)) is applied to the raw 24-h (0800-0800 UTC) radar rainfall depths from 1998 to 2007 for every day and radar separately:

$$R_{VPR}(i, j) = R_{raw}(i, j) \times 10^{F_{VPR}(i, j)/10}. \quad (3.5)$$

For ranges shorter than 15 km,  $\Delta h$  is set to 0. This backtransformation from logarithmic values to 24-h rainfall depths causes a bias that is on the order of -0.10 mm (Table 3.3), implying an underestimation of the mean 24-h manual rain gauge depth (2.55 mm).

### 3.3.3 Compositing of accumulation images

Accumulation images from the individual radars are combined into one composite using a weighting factor as a function of range  $r$  (km) from the radar:

$$W(r) = \begin{cases} \left(\frac{r}{70}\right)^2 & \text{if } r \leq 70 \text{ km,} \\ 1 - \left(\frac{r-70}{200-70}\right)^2 & \text{if } r > 70 \text{ km} \wedge r < 200 \text{ km,} \\ 0 & \text{if } r \geq 200 \text{ km,} \end{cases} \quad (3.6)$$

with 200 km as the maximum quantitative range and 70 km as the range with the maximum weight. This works well because the distance between the two radars is less than 100 km. The quadratic decrease of the weighting factor with increasing range for  $r > 70$  km reflects the decreasing data quality at long range. Accumulations close to the radar are assigned lower weights to limit the impact of bright bands and spurious echoes. A composited accumulation is calculated both for the raw and the VPR-adjusted images as

$$R_{raw}^c(i, j) = \frac{\sum_{m=1}^M W[r^m(i, j)] \times R_{raw}^m(i, j)}{\sum_{m=1}^M W[r^m(i, j)]} \text{ and} \quad (3.7)$$

$$R_{VPR}^c(i, j) = \frac{\sum_{m=1}^M W[r^m(i, j)] \times R_{VPR}^m(i, j)}{\sum_{m=1}^M W[r^m(i, j)]}, \quad (3.8)$$

where  $M$  is the number of radars (here  $M = 2$ ),  $c$  denotes the composite, and  $r^m(i, j)$  is the range between radar  $m$  and the pixel at  $(i, j)$ . This compositing method prevents the occurrence of discontinuities in the radar-derived rainfall images in the vicinity of the radar and at the edge of the coverage of a radar.

Figure 3.3 (page 56) shows that the January 2004 precipitation depth from the VPR-adjusted radar data (e) is clearly in better agreement with the interpolated monthly sum from the manual rain gauges (c) than that from the raw radar data (d). The distinct underestimation near the borders of the Netherlands has largely disappeared and has changed into an overestimation for the southwestern and southeastern part of the country and most islands in the north. To account for such biases, a spatial adjustment (Brandes, 1975; Michelson and Koistinen, 2000) on the unadjusted rainfall accumulation composites is described in the next section.

### 3.3.4 Daily spatial adjustment of composites (S adjustment)

The spatial adjustment factor  $F_S^c$  follows from the ratio of a distance-weighted interpolation (Barnes, 1964) of the manual gauge precipitation depths and the interpolation of the corre-

sponding raw radar daily precipitation depths:

$$F_S^c(i, j) = \frac{\sum_{n=1}^N w_n(i, j) \times G(i_n, j_n)}{\sum_{n=1}^N w_n(i, j) \times R_{raw}^c(i_n, j_n)}, \quad (3.9)$$

where the subscript  $S$  denotes the spatial adjustment method,  $N$  is the number of radar-gauge pairs, and  $w_n(i, j)$  is a weighting function, given by

$$w_n(i, j) = \exp[-d_n^2(i, j)/\sigma^2], \quad (3.10)$$

where  $\sigma$  determines the smoothness of the  $F_S^c$  field and  $d_n(i, j)$  is the distance between manual rain gauge  $n$  and pixel  $(i, j)$ . The denominator of Eq. (3.9) is set to 0.75 mm if it becomes smaller than that value; the same holds for the numerator. The value of  $\sigma$ , 12 km, is comparable to the average gauge spacing of 10 km. This value is large enough to prevent the removal of the small-scale spatial rainfall variability that radar data reveal. If  $\sigma$  tends to infinity, a mean-field bias adjustment method is obtained. Because the adjustment factor is derived on the original scale, there is no retransformation bias. The interpolation of  $G$  and  $R^c$  rather than  $G/R^c$  or its logarithm avoids the situation in which relatively large weight is given to small rainfall amounts. The daily composite of raw accumulated precipitation from the radars is adjusted for each day as:

$$R_S^c(i, j) = R_{raw}^c(i, j) \times F_S^c(i, j). \quad (3.11)$$

Using Eq. (3.11), the spatial adjustment factor fields of the daily composites are also employed to calculate spatially adjusted 1-h composites.

Figure 3.3 (f, page 56) shows that the spatially adjusted monthly precipitation sum is in good agreement with the interpolated monthly sum based on the manual gauge data. In contrast to the VPR adjustment, the overestimation near the borders of the Netherlands has disappeared. The radar reveals the monthly depths in more detail than does the network of manual rain gauges ( $\approx 1$  station per 100 km<sup>2</sup>).

### 3.3.5 Hourly mean-field bias adjustment of composites (MFB adjustment)

Using automatic rain gauges a mean-field bias adjustment (Holleman, 2007) is applied to the 1-h unadjusted composited radar rainfall accumulations. The adjustment is only pursued if at least 1.0 mm of precipitation has been measured over all rain gauges and also over their corresponding radar pixels. The bias adjustment factor  $F_{MFB}^c$  is given by

$$F_{MFB}^c = \frac{\sum_{n=1}^N G(i_n, j_n)}{\sum_{n=1}^N R_{raw}^c(i_n, j_n)}, \quad (3.12)$$

where  $G(i_n, j_n)$  is the amount of rain for automatic rain gauge  $n$ ,  $R_{raw}^c(i_n, j_n)$  is the amount of rain for the corresponding radar pixel, and  $(i_n, j_n)$  are the image coordinates of rain gauge  $n$ , and MFB denotes mean-field bias. The hourly composite of raw accumulated precipitation from the radars is subsequently adjusted for each hour as

$$R_{MFB}^c(i, j) = R_{raw}^c(i, j) \times F_{MFB}^c. \quad (3.13)$$

### 3.3.6 Spatial adjustment of MFB-adjusted composites (MFBS adjustment)

The 1-h MFB-adjusted rainfall depths are accumulated to 24-h 0800 UTC rainfall depths. At each pixel, the spatially adjusted 24-h 0800 UTC depth is subsequently divided by the corresponding MFB-adjusted depth, which implies an adjustment factor field:

$$F_{MFBS}^c(i, j) = R_S^c(i, j) / R_{MFB}^c(i, j). \quad (3.14)$$

Next, the 1-h MFB-adjusted rainfall depths are multiplied with this adjustment factor field to obtain both mean-field bias and spatially adjusted 1-h rainfall depths, denoted by  $R_{MFBS}^c$ :

$$R_{MFBS}^c(i, j) = R_{MFB}^c(i, j) \times F_{MFBS}^c(i, j). \quad (3.15)$$

These 1-h composites of accumulated rainfall are used to construct depths for durations of 2, 4, 8, 12, and 24 h for each clock-hour.

## 3.4 Characterization and verification of adjusted accumulations

### 3.4.1 Seasonal cycle of the VPR gradient

Although the VPR radar-gauge adjustment is statistical, the estimated VPR gradients can be related to the type of rainfall. Figure 3.4 shows the daily VPR gradient  $a$  and bias  $b$  from Eq. (3.4) as a function of the date for the radar in De Bilt. The VPR gradient displays a clear seasonal cycle with mainly negative values in winter and clearly higher ones in summer. For every year, the dashed vertical line represents 1 July. In contrast, no seasonal cycle is found for the bias, which is systematically lower from the middle of 2004. This result is caused by a sudden change in the calibration of the radar receiver. The change is attributed to failures in the signal generator used to calibrate the radar receiver. For most days, the bias is negative, indicating that the radar underestimates precipitation with respect to rain gauges most of the time after VPR adjustment. A negative (positive) VPR gradient implies that the radar reflectivity on average decreases (increases) with height. The negative gradients in winter are notably attributed to partial overshooting of precipitation due to the dominance of stratiform rainfall, which is shallow. In summer, convective rainfall occurs more frequently, which has a larger vertical extent and strong reflectivity cores aloft causing positive VPR gradients. For the United Kingdom, Hand (1996) shows idealized vertical reflectivity profiles for the cell stages of cumulonimbus clouds. For most stages reflectivities between the cloud base and the midcloud level are considerably larger than those below the cloud base. The VPR gradient ( $\text{dBR km}^{-1}$ ) can be converted to a gradient in reflectivity decibels per kilometer using Eq. (3.1); thus, the values differ by a factor of 1.6. Typical values from  $-8$  to  $0 \text{ dBZ km}^{-1}$  in winter and from  $-2$  to  $4 \text{ dBZ km}^{-1}$  in summer are found in Figure 3.4. Most days have a VPR gradient above  $-8 \text{ dBZ km}^{-1}$  ( $-5 \text{ dBR km}^{-1}$ ). This corresponds well to results in Joss and Waldvogel (1990), who state that a VPR gradient of  $-7.5 \text{ dBZ km}^{-1}$  would only occur for a flat country in the case of snow or significant low-level growth of raindrops. In the Netherlands, rainfall is by far the most dominant type of precipitation.

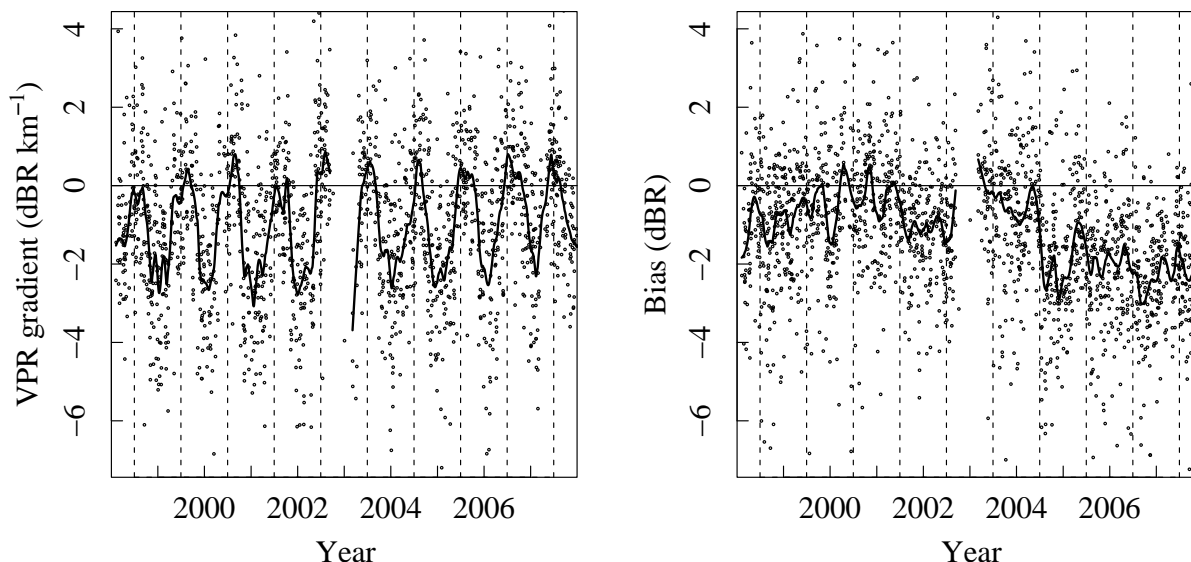


**Figure 3.4:** Daily VPR gradient  $a$  ( $\text{dBR km}^{-1}$ ) and bias  $b$  after VPR adjustment ( $\text{dBR}$ ) as a function of the date for the De Bilt radar (dots). VPR gradients of  $0 \text{ dBR km}^{-1}$  and biases of  $0 \text{ dBR}$  have been omitted. For each year, 1 Jul is indicated by a dashed vertical line. Seasonality and trend are highlighted by a “loess” (Cleveland, 1979) smooth (lines). 2002 contains a large gap in the available radar data.

For the Finnish climate, Koistinen et al. (2003) present an annual average of the difference between the radar reflectivities just above the surface and those at the 500-m pseudo CAPPI level. For rainfall near the surface the reflectivity gradient varies typically between  $-6$  and  $3 \text{ dBZ km}^{-1}$ . These gradients are in reasonable agreement with the range of values shown in Figure 3.4.

### 3.4.2 Verification with manual rain gauges

The manual rain gauge network is used to verify 24-h (0800 UTC) raw, MFB-adjusted (Eqs. (3.12)-(3.13)), VPR-adjusted (Eqs. (3.2)-(3.5)), S-adjusted (Eqs. (3.9)-(3.11)), and MFBS -adjusted (Eqs. (3.14)-(3.15)) radar rainfall accumulations. The residuals, that is, the differences between the radar-derived and rain gauge-derived rainfall, are calculated for each radar-gauge pair. Table 3.3 shows a clear underestimation of precipitation for the raw radar data. Note that the results of the methods S and MFBS for the 24-h (0800 UTC) depths are equal by definition and are therefore combined in one column. The adjustments considerably decrease the residual standard deviation, especially the spatial adjustment, and reduce the bias in the mean to 1%-6% of the average 24-h manual rain gauge depth of 2.55 mm. The spatial adjustment methods clearly outperform the MFB and VPR methods. The remaining bias of  $-0.10 \text{ mm}$  for the VPR adjustment method is mainly due to the backtransformation from logarithmic adjustment factors to 24-h rainfall depths.

Residual standard deviation and bias in the mean are also calculated for days with rain gauge and/or radar rainfall depths larger than 10 and 20 mm, based on, respectively, from 70 293 to 81 697 and from 14 769 to 18 610 radar-gauge pairs. The bias in the mean daily rainfall reduces significantly for all adjustments. Even after the spatial adjustment there remains, however, a negative bias, which may be caused by radome and rainfall attenuation. The residual standard deviation decreases for the spatial adjustment method. For the MFB and VPR adjustments, the changes in the residual standard deviation are much less pronounced.

Whether combining the VPR and spatial adjustment would lead to better results was also investigated. However, it appeared that the bias in the mean and the residual standard deviation for the cases in Table 3.3 are almost the same as those of the spatially adjusted data.

To investigate the spatial quality of rainfall accumulations, bias in the mean daily rainfall and residual standard deviation are calculated for each radar-gauge pair for the MFB, VPR, and MFBS (or S) adjustments. For the MFB adjustment, Figure 3.5 (page 57) shows very negative biases near the borders of the Netherlands and positive ones in the middle of the country, as was also found by Holleman (2007). The VPR adjustment removes an important part of the range dependency in the bias, although the southeastern part of the country exhibits rather positive values. For the MFB and VPR methods, the residual standard deviation ranges from, respectively, 1.52 to 3.88 and from 1.41 to 2.82 mm. Therefore, the spatial variation in residual standard deviation is diminished by the VPR method. The spatial adjustment considerably reduces the bias in the mean and the residual standard deviation. The latter ranges from 0.52-1.61 mm.

In conclusion, only the spatial adjustment method effectively removes range dependencies in radar rainfall depths, and it has the smallest bias in the mean and the smallest residual

**Table 3.3:** Verification of 24-h 0800 UTC rainfall accumulations of radar composites. Results are shown for the unadjusted data (raw), mean-field bias (MFB) adjusted data, VPR-adjusted data, and spatially (S/MFBS) adjusted data. Number of radar-gauge pairs, mean daily rainfall depth of the manual rain gauges, bias in the mean daily rainfall, and residual std dev are given for the verification with the manual rain gauge network.

No.	Mean (mm)	Bias (mm)				Std dev (mm)			
	Rain gauge	Raw	MFB	VPR	S/MFBS	Raw	MFB	VPR	S/MFBS
978 068	2.55	-0.88	-0.15	-0.10	-0.03	2.71	2.14	1.88	1.03
Rain gauge and/or radar rainfall depth > 10 mm:									
		-6.70	-0.74	-0.87	-0.37	6.56	6.40	5.65	3.02
Rain gauge and/or radar rainfall depth > 20 mm:									
		-12.61	-1.13	-2.15	-0.98	9.32	10.40	9.25	4.77

standard deviation. The VPR adjustment is not employed in the remainder of this chapter, given that it performs worse than the spatial adjustment method. The hourly MFB adjustment is considered further because this method is expected to show good results in the verification of short-duration rainfall.

### 3.4.3 Verification with automatic rain gauges

The 10-yr data set of radar-derived composited rainfall accumulations is verified with the automatic rain gauge network for durations  $D$  of 1, 2, 4, 8, 12, and 24 h, where the accumulations are obtained for every clock-hour. Again, the residuals are calculated for each radar-gauge pair. Raw, MFB-adjusted, S-adjusted, and MFBS-adjusted radar rainfall accumulations are verified.

As seen in Table 3.4, the bias in the mean 1-h rainfall depth is reduced from -0.03 mm for the raw data to 0.00 and 0.01 mm for, respectively, the MFB and both spatial adjustment methods, the mean 1-h gauge rainfall depth being 0.10 mm. The adjustments reduce the residual standard deviation. Residual standard deviation and bias in the mean are also calculated for hours with rain gauge and/or radar rainfall depths larger than 5 and 10 mm, based on, respectively, 4414 to 5454 and 749 to 909 radar-gauge pairs. The adjustments clearly diminish the bias in the mean; however, the reduction in the residual standard deviation is less pronounced. The daily adjustment method S results in less-negative biases than the hourly adjustment method MFB, which is, however, more successful in reducing the residual standard deviations. Because of the variable temporal distribution of rainfall amounts over a day and the possible alternation of convective and stratiform rainfall, a daily adjustment factor field will not always result in properly adjusted 1-h rainfall depths. The combined hourly and daily adjustment (MFBS) method gives the smallest bias in the mean and the smallest residual standard deviation. This implies that a daily adjustment using a dense gauge network, which improves the spatial quality of the rainfall depths, has added value if applied to 1-h rainfall depths that are already MFB adjusted.

The negative bias in the mean daily rainfall for the verification with manual gauges (Table 3.3) changes into 0.12 mm for both spatial adjustment methods (Table 3.4). This is probably due to the bias in the automatic rain gauge measurements with respect to those from the manual rain gauges. To investigate the validity of this, the differences between the 24-h accumulations from manual and automatic rain gauges within a 2.4-km radius are calculated for the entire period 1998-2007 using, on average, 21 pairs per day. These differences are, on average, 0.14 mm, which implies that manual rain gauge depths are systematically higher relative to the automatic rain gauge depths. According to Chapter 2, where 12 stations from the two rain gauge networks were utilized, annual rainfall sums from manual rain gauges are, on average, 5% larger than those from collocated automatic rain gauges. This corresponds to the change in bias between the verification with manual and automatic gauges of 6% of the mean daily gauge rainfall depth, and this change can therefore be attributed to the automatic rain gauges having a different measurement technique than the manual



ones. The standard deviation of the differences between manual and automatic gauges is 1.06 mm. This indicates that an important part of the standard deviation of the differences between the 24-h MFBS radar and automatic rain gauge accumulations (1.32 mm) is caused by subpixel rainfall variations.

Next, for each duration the residuals are ranked in increasing order and the values belonging to the 2.5th, 50th (median), and 97.5th percentiles are determined and plotted in Figure 3.6. For the raw radar data, the interval between the 2.5th and 97.5th percentiles of the residuals is wide, 9.4 mm for  $D = 24$  h, and the distribution is negatively skewed, implying that with respect to rain gauges the underestimates are more severe than the overestimates. Note that also values of (near) zero rainfall, which occur so frequently that the median is close to zero, are used to construct Figure 3.6.

For  $D = 24$  h, the percentile interval decreases to 4.9 mm for the MFBS adjustment method and the asymmetry of the distribution of the residuals has disappeared. Similar results are obtained for durations that are less than 24 h, although the percentile interval is reduced only slightly for  $D = 1$ -4 h. Germann et al. (2006) also find an underestimation for raw daily radar precipitation depths that is considerably reduced if, among other things, a real-time VPR adjustment and a global bias correction are applied.

For  $D = 24$  h, the residual standard deviation decreases from 2.58 (raw) to 1.81 (MFB), 1.38 (S), and 1.32 (MFBS) mm; see Table 3.4. If the residuals were normally distributed, the interval between the 2.5th and 97.5th percentiles would be equal to 4 times the standard deviation. This would result in a percentile interval of 10.3 (raw) or 5.3 (MFBS) mm. These

**Table 3.4:** Verification of 1-h and 24-h composited rainfall accumulations for every clock-hour. Results are shown for the unadjusted data (raw), MFB-adjusted data, S-adjusted data, and MFBS-adjusted data. Number of radar-gauge pairs, mean rainfall depth of the automatic rain gauges, bias in the mean rainfall, and residual std dev are given for the verification with the automatic rain gauge network.

	Mean (mm)	Bias (mm)				Std dev (mm)			
No.	Rain gauge	Raw	MFB	S	MFBS	Raw	MFB	S	MFBS
<i>1-h rainfall depths</i>									
2 336 315	0.10	-0.03	0.00	0.01	0.01	0.35	0.29	0.30	0.27
Rain gauge and/or radar rainfall depth > 5 mm:									
		-3.81	-0.82	-0.80	-0.51	4.60	3.96	4.32	3.80
Rain gauge and/or radar rainfall depth > 10 mm:									
		-8.59	-3.16	-2.69	-2.06	6.98	6.63	7.58	6.55
<i>24-h rainfall depths</i>									
2 250 878	2.41	-0.75	-0.04	0.12	0.12	2.58	1.81	1.38	1.32

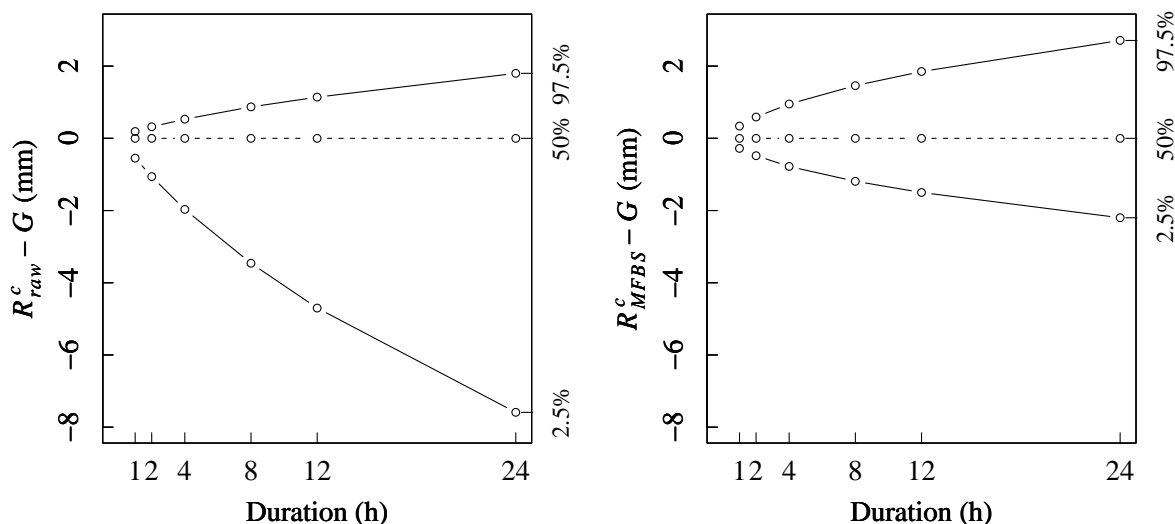


**Figure 3.6:** The 2.5th, 50th (median), and 97.5th percentiles of the residuals (mm) in the verification with automatic rain gauges plotted against duration for the composited (left) raw and (right) MFBS-adjusted radar data.

values are higher than those given above, implying that the residuals are not well approximated by the normal distribution, which situation is caused by the frequent occurrence of (near) zero rainfall and, for the raw radar data, also by the asymmetry.

From the verification with automatic gauges, it appears that the MFBS adjustment performs well on both daily and subdaily accumulations and generally removes the systematic underestimation of precipitation by radar more effectively than do the other adjustments.

### 3.5 Long-term radar rainfall statistics

The Netherlands, which is located in the midlatitudes, has a temperate climate with prevailing westerly winds. The mean annual rainfall varies spatially from 675 to 925 mm. In this section, the MFBS-adjusted radar rainfall climatology is analyzed to derive exceedance probabilities, mean annual rainfall frequencies, maximum rainfall depths, and spatial correlations. In comparisons with climatologies from gauge data, these data were only used if the corresponding radar data were available, except for exceedance probabilities.

#### 3.5.1 Empirical exceedance probabilities

Based on the radar data set, empirical exceedance probabilities of rainfall are calculated. Only the radar data above the land surface of the Netherlands are selected. Using the rainfall depths from all radar pixels (6190), rainfall frequencies are computed for classes of 1 mm.

Exceedance frequencies are subsequently calculated and are scaled with the sum of all frequencies, so that empirical exceedance probabilities of rainfall depths are obtained, which are shown in Figure 3.7 for different durations. For example, the left panel demonstrates for the spatially adjusted radar data that a 24-h 0800-0800 UTC rainfall depth of 100 mm has

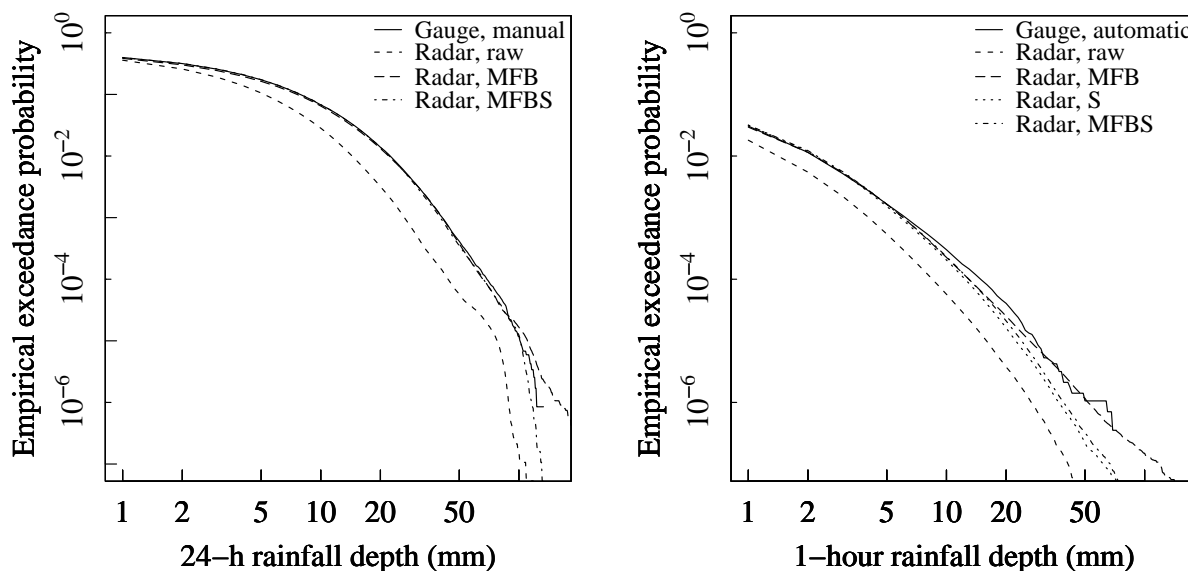
an exceedance probability of approximately  $1.2 \times 10^{-5}$ , implying that on average this rainfall depth is exceeded approximately once in  $8.1 \times 10^4$  days ( $\approx 223$  yr) in an arbitrary radar pixel. These exceedance probabilities are spatial averages over the Netherlands and are assumed to be independent of season. Deviations from these averages are probably limited, because the Netherlands is a relatively small and flat country.

Figure 3.7 shows that the exceedance probabilities of 24-h 0800-0800 UTC rainfall from the adjusted radar data (MFB and MFBS) are, in general, in good correspondence with those based on the manual rain gauges, whereas the use of raw radar data results in much lower exceedance probabilities. Therefore, adjustment of radar data with rain gauges is a prerequisite to obtain reliable exceedance probabilities of rainfall. Even the MFB adjustment method removes the systematic underestimation of exceedance probabilities; however, large exceedance probabilities are found at high rainfall depths.

To explain the good correspondence between the exceedance probabilities from the adjusted radar data and the manual rain gauge data, the standard deviations of the 24-h 0800-0800 UTC rainfall depths are calculated. These are 4.81, 4.71, and 4.77 mm for, respectively, the rain gauge data, the MFB-adjusted, and the MFBS-adjusted radar data. The differences among these standard deviations are small, even though the standard deviations of the residuals in Tables 3.3 and 3.4 are still substantial in the case of MFB and MFBS adjustments (about 38%-44% and 21%-27% of the standard deviation of the daily manual rain gauge depths). These residuals contain a component representing the subpixel rainfall variation and a remaining bias of radar rainfall (Ciach and Krajewski, 1999). Because of the first component the variance of the rain gauge rainfall is larger than that of the true area-averaged rainfall, whereas because of the second component the variance of the radar rainfall is larger than that of the true area-averaged rainfall. However, the increase in standard deviation due to adding a random component to the true area-averaged rainfall is usually limited. For instance, if the standard deviation of the random component is 20% of the standard deviation of the true area-averaged rainfall, the increase is only 2%. This explains the small differences between the radar and gauge standard deviations.

Figure 3.7 also gives the exceedance probabilities for the 1-h rainfall depths. Again the MFB adjustment is successful in removing the systematic underestimation of exceedance probabilities in the raw radar data. However, an important shortcoming of the MFB method is the large exceedance probabilities at high rainfall depths. It appears that the MFB adjustment creates a number of outliers. Therefore, it is important to apply a daily spatial adjustment after the mean-field bias adjustment. Then, the number of outliers is limited. The exceedance probabilities after the spatial adjustments are in good correspondence with those from the automatic rain gauge data up to a rainfall amount of 20 mm.

Figure 3.8 gives the exceedance probabilities for 1-, 2-, 4-, 8-, 12-, and 24-h accumulated rainfall for the MFBS-adjusted radar data. For instance, a 1-h rainfall depth of 5 mm is exceeded



**Figure 3.7:** Exceedance probabilities of (left) 24-h 0800-0800 UTC and (right) 1-h rainfall sums over the period 1998-2007.

on average approximately once in 610 clock-hours ( $\approx 25$  days). These exceedance probabilities are based on the  $D$ -hour accumulations for every clock-hour. This provides more accurate estimates than the use of nonoverlapping  $D$ -hour accumulations. In the latter case, there is even a risk that the line of, for instance, the 8-h exceedance probabilities crosses that of the 12-h exceedance probabilities because the amount in the 1600-0000 UTC interval can exceed the amounts in the 0800-2000 and 2000-0800 UTC intervals. Therefore, exceedance probabilities are calculated using accumulations for every clock-hour.

### 3.5.2 Rainfall frequency and maximum rainfall depths

Now that the exceedance probabilities have shown a reasonable correspondence with those from rain gauges, the spatial distribution of extreme rainfall is investigated in this section. Figure 3.9 displays the maximum daily (0800-0800 UTC) rainfall sums from manual rain gauge data (a) and MFBS-adjusted radar data from the corresponding pixel (b) for the period 1998-2007 and demonstrates a good resemblance between both. Differences can partly be attributed to spatial representativeness errors, since the radar image has a 2.4-km spatial resolution and the rain gauge is a point measurement (Kitchen and Blackall, 1992).

For the radar data also the maximum 1-h rainfall sums are plotted (c), which is, at an acceptable spatial resolution, not possible for the rain gauge data. The maximum 1-h rainfall sum shows a strong spatial variation, with values ranging from 12 to 127 mm (only five values exceed 100 mm). This is mainly due to the long upper tail of the distribution of the hourly precipitation amounts and some artificially large values. Figure 3.9 also gives the mean annual number of days with more than 10 mm and hours with more than 5 mm of rain. The radar-based mean annual number of days (e) corresponds well to that from the

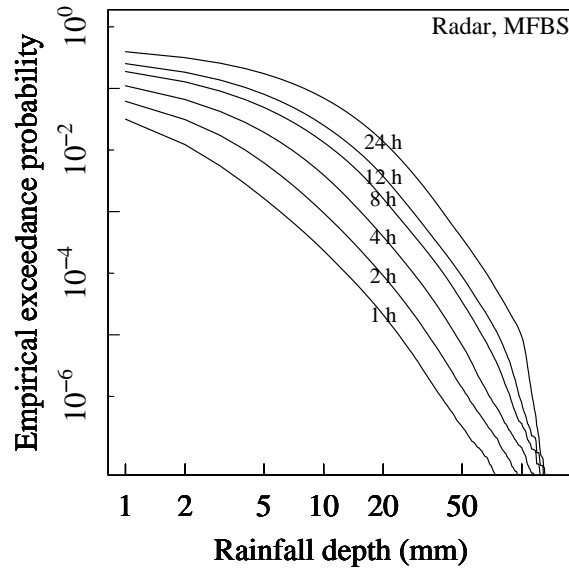


**Figure 3.8:** Exceedance probabilities of 1-, 2-, 4-, 8-, 12-, and 24-h rainfall sums over the period 1998-2007 for the MFBS adjustment method.

rain gauges (d). The mean annual number of clock-hours with more than 5 mm (f) displays a large spatial variability and ranges from 8 to a value as high as 22 (not shown: one outlier of 28). This is mainly a consequence of the large year-to-year variation and weak spatial correlation of such events. For only 5.4% of the pixels, the mean annual number of hours with more than 5 mm of rain differs by more than 2 times its standard deviation from the countrywide mean annual number of exceedances, implying that the spatial variability can be attributed to randomness. This percentage is larger for, respectively, the 24-h radar (17%) and rain gauge (22%) depths. Earlier studies that show the spatial distribution of rainfall frequencies are Croft and Shulman (1989) and Baeck and Smith (1995).

### 3.5.3 Spatial correlation

The spatial correlation of precipitation is investigated for different timescales. In Figure 3.10 cross correlations between precipitation depths are plotted against distance for MFBS-adjusted radar data ( $D = 1$  and  $24$  h) and automatic rain gauges ( $D = 24$  h). Only radar data at the location of the automatic rain gauges are selected. The exponential decay of precipitation depths with interpixel or intergauge distance can be described reasonably with

$$\rho(x) = \exp \left[ - \left( \frac{x}{x_0} \right)^{s_0} \right], \quad (3.16)$$

where  $\rho(x)$  is the correlation at distance  $x$  (km),  $x_0$  a scale parameter (km) and  $s_0$  is a shape parameter. The influence of anisotropy is not considered. The correlation coefficients were estimated with the method of nonlinear least squares. Ciach and Krajewski (2006) employed a similar model for spatial correlations in small-scale rainfall. A rain gauge depth is only

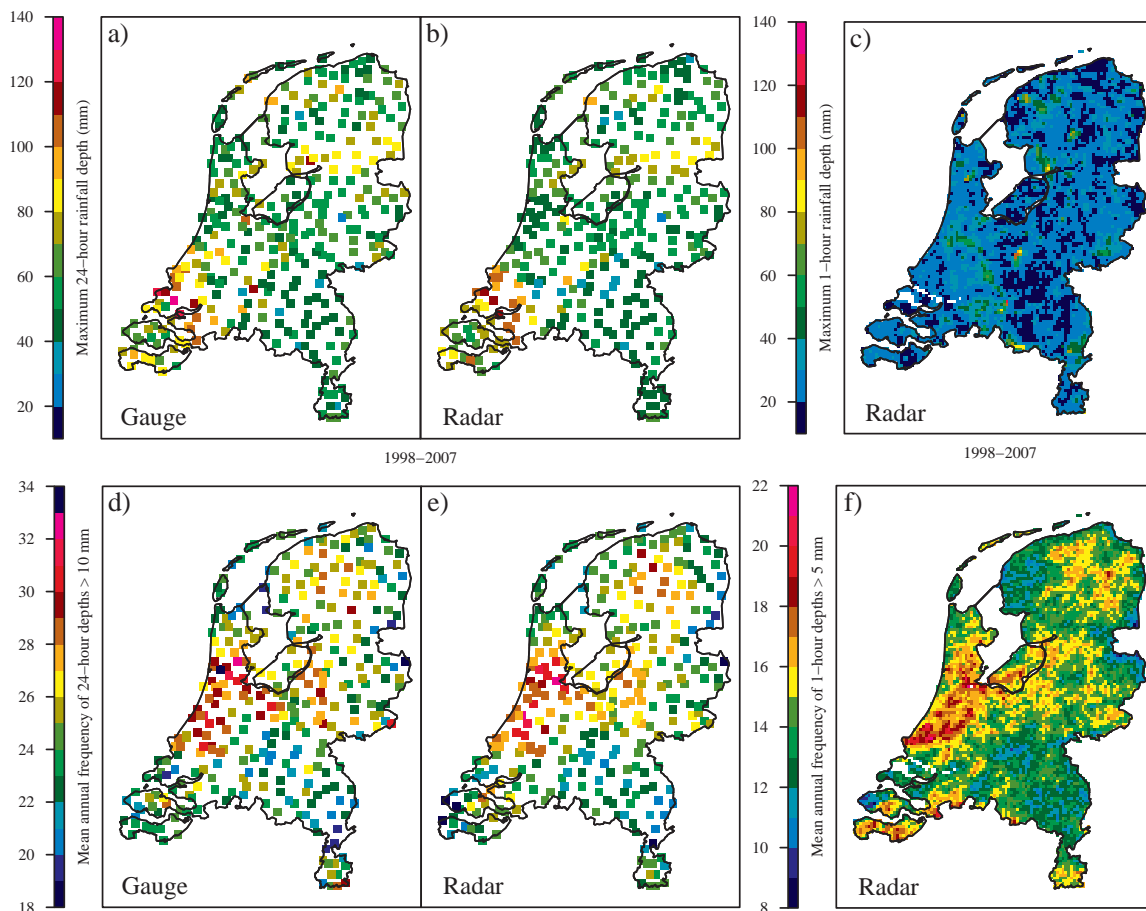


**Figure 3.9:** (top) Maximum rainfall depths over the period 1998-2007 and (bottom) mean annual number of days with more than 10 mm and hours with more than 5 mm, based on the 24-h accumulations (0800-0800 UTC) from (a),(d) manual rain gauges and (b),(e) radar (MFBS adjusted) and on (c),(f) the 1-h MFBS-adjusted radar accumulations.

taken into account if the radar depth is available and vice versa. Further, only precipitation depths of at least 0.5 mm in 1 or 24 h are used in the estimation of the correlation. The radar measures over  $5.7\text{-km}^2$  areas, and the rain gauge produces point measurements in space. Because of this, rain gauge measurements are more influenced by small-scale events and have therefore a slightly lower spatial correlation than the radar-based accumulations. Further, the correlations for  $D = 24$  h are much higher than those for  $D = 1$  h. This is related to the spatial-temporal correlation structure of rainfall fields. For instance, the spatial correlation between the 1- and 24-h accumulations would be the same if there were no temporal correlation, which is obviously not the case.

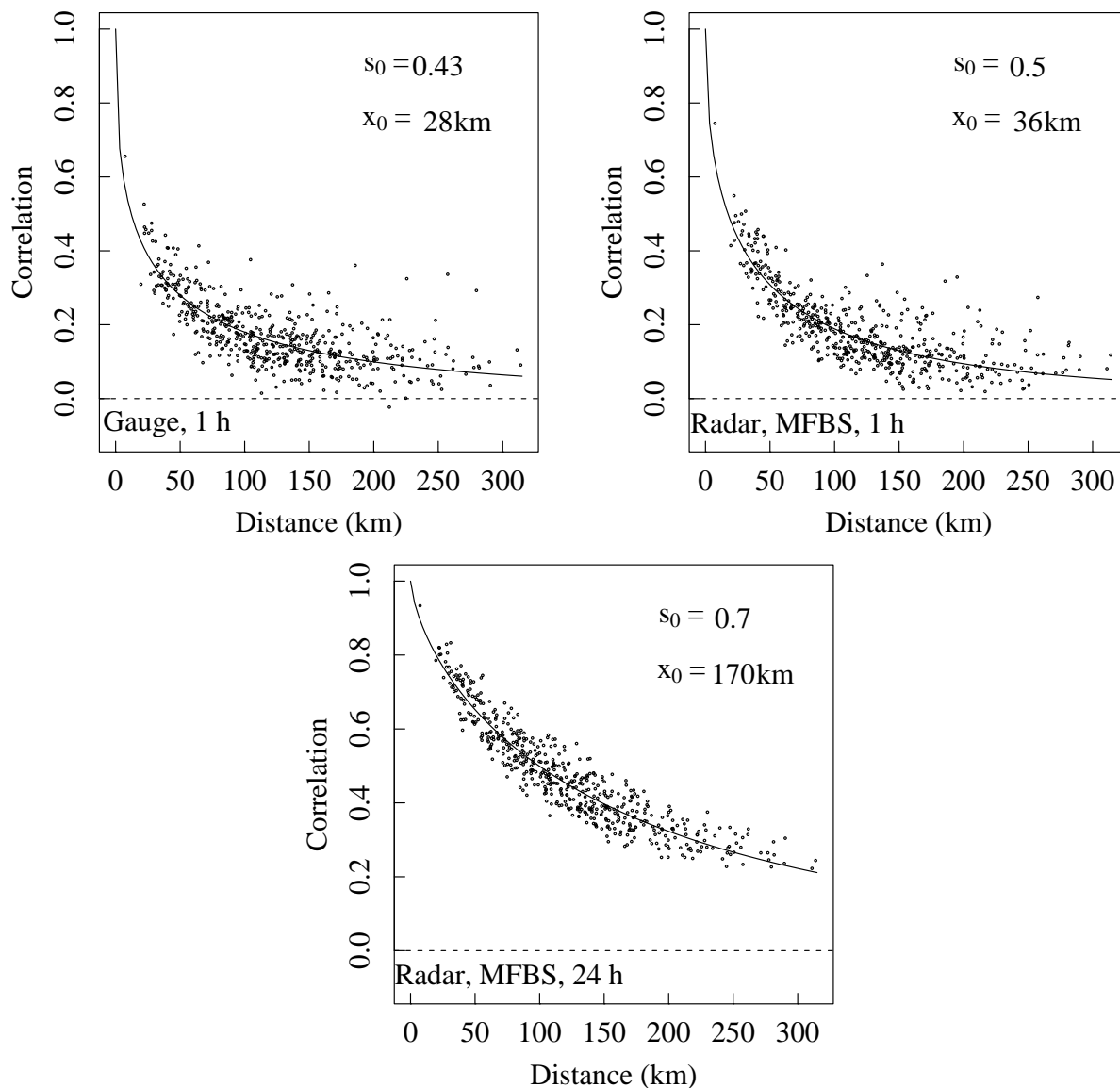


**Figure 3.10:** Correlation between (left) 1-h rain gauge, (right) 1-h radar, and (bottom) 24-h radar precipitation depths as a function of distance.

### 3.6 Conclusions and recommendations

Based on data from two weather radars, a 10-yr rainfall climatology was constructed for the Netherlands. The radar data were corrected for occultation and anomalous-propagation ground clutter. Using manual rain gauges, two daily adjustment methods were applied separately and verified: 1) a VPR and bias adjustment and 2) a spatial adjustment. The 24-h (0800-0800 UTC) spatial adjustment field was also applied to the 1-h unadjusted radar data. Automatic rain gauges were employed to derive MFB-adjusted 1-h precipitation depths. The spatial and MFB adjustment methods were combined to derive 1-h rainfall depths. For

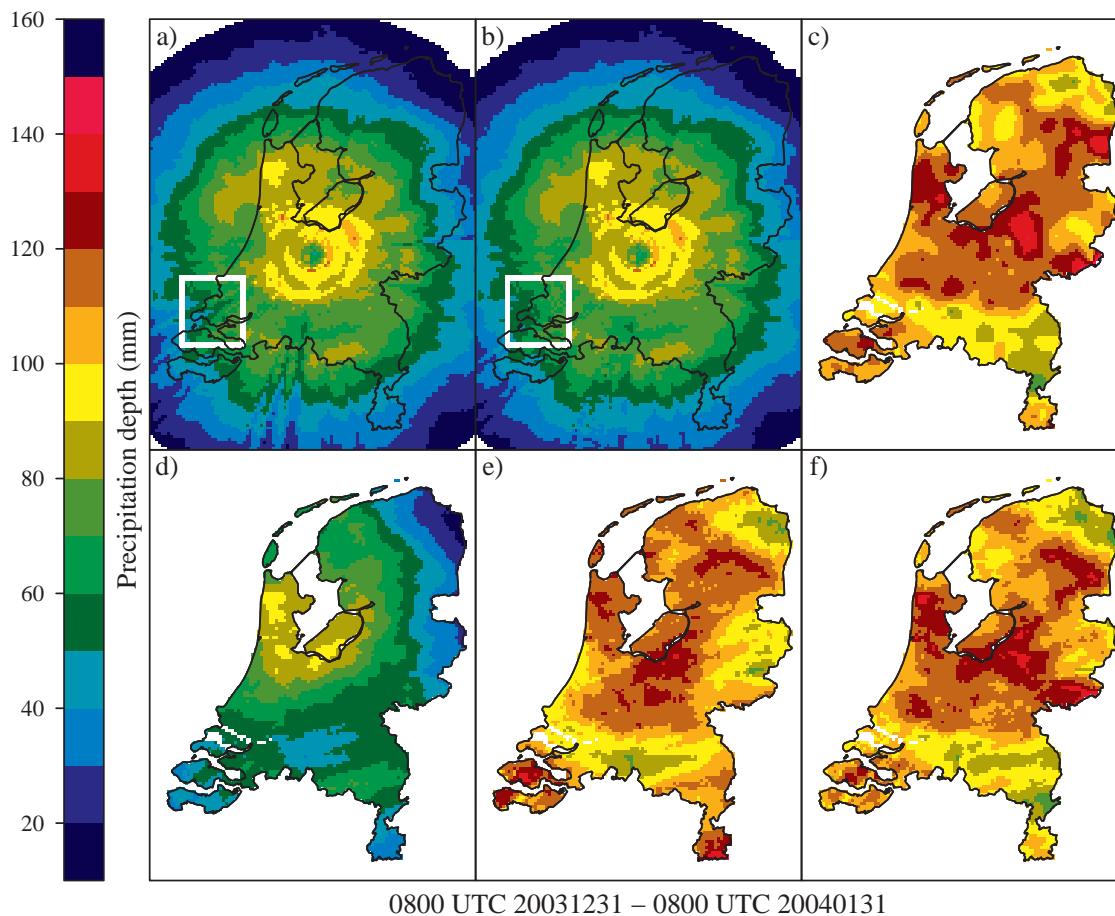


**Figure 3.3:** Monthly rainfall depths for January 2004 for a) the raw De Bilt radar data, b) the raw De Bilt radar data corrected for occultation, c) the manual rain gauges (interpolated), d) the raw radar composite corrected for occultation, e) the VPR-adjusted radar composite, and f) the spatially (S/MFBS) adjusted composite. For this month both radars have a data availability of 100%.

each clock-hour, 2-, 4-, 8-, 12-, and 24-h accumulations were derived from the 1-h rainfall composites. The accumulations were verified with rainfall depths from automatic ( $D \leq 24$  h) and manual ( $D = 24$  h) rain gauge networks. The newly developed combination of an hourly mean-field bias and a daily spatial adjustment method gave the best verification results. Therefore, this data set was used to derive exceedance probabilities, mean annual frequencies, maximum rainfall depths, and spatial correlations.

This chapter contains a description and an analysis of one of the longest radar data sets described in the literature. The data set has a high resolution, which is a prerequisite to derive accurate rainfall climatologies. Also, subdaily rainfall depths are obtained. The combination of an hourly mean-field bias adjustment and a daily spatial adjustment is a novel approach that improves the quality of subdaily radar rainfall depths considerably. An improved spa-



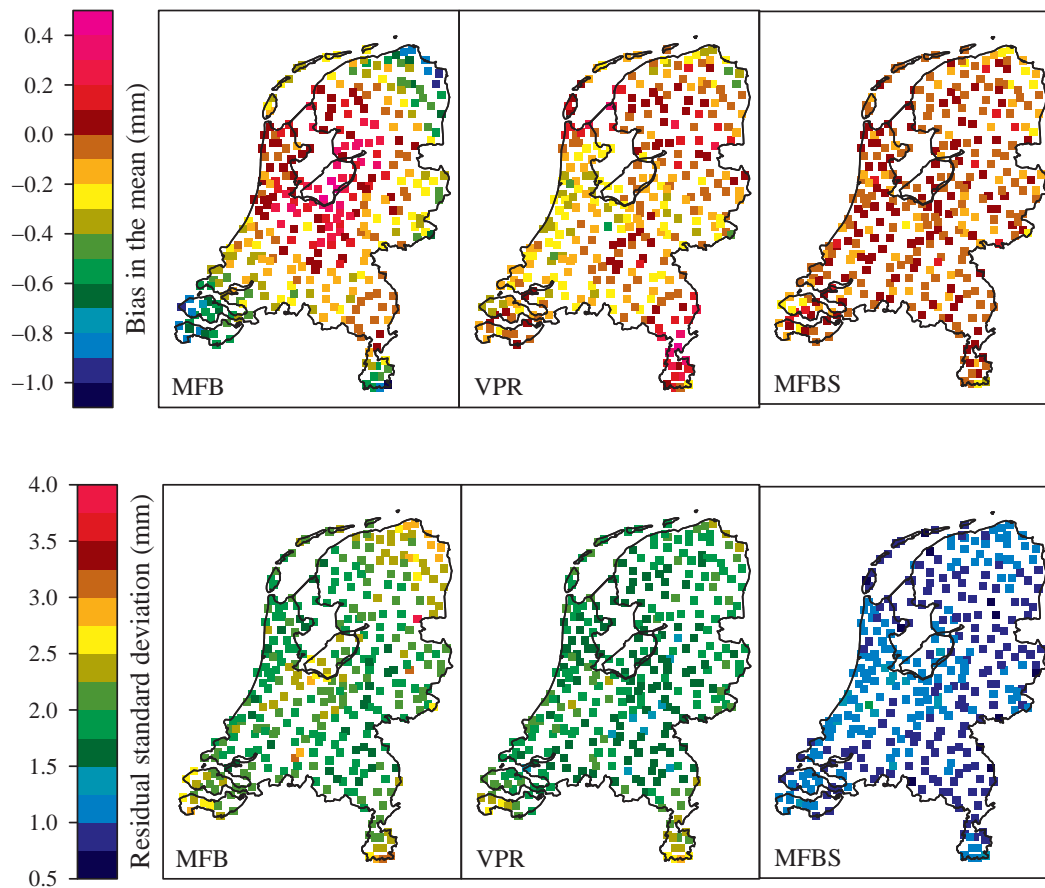


**Figure 3.5:** Spatial verification of 24-h 0800 UTC rainfall depths of radar composites against manual gauges. Results are shown for the (left) MFB-adjusted, (middle) VPR-adjusted, and (right) MFBS-adjusted (right) radar data for (top) the bias in the mean and (bottom) the residual std dev.

tial adjustment method was developed in which the normally used logarithmic adjustment was replaced by a proportional adjustment.

The seasonal cycle displayed in the 10-yr VPR gradient climatology partly reveals the influence of stratiform and convective rainfall on QPE with radar at long ranges. The most innovative aspect of this chapter consists of the rainfall climatologies, such as the exceedance probabilities and spatial correlations, especially for durations of less than 24 h. Furthermore, the radar-based precipitation climatologies have a spatial and temporal resolution that is unmatched by conventional rain gauge networks.

Representativeness errors of radar and rain gauges limit the extent to which rain gauges should be used to adjust radar rainfall depths and cause a large part of the scatter between radar and rain gauge observations. Nonetheless, for climatological purposes radar data

should be adjusted with rain gauges or disdrometers in a sensible manner, because of the possible errors in QPE with radar.

Errors in QPE not specifically accounted for in this chapter are attenuation, bright band effects, and advection of precipitation. However, the spatial adjustment will probably correct an important part of these errors. The VPR adjustment method is partially successful in correcting for spatial differences in the quality of radar rainfall depths. The VPR adjustment is a mean-range correction, whereas in reality large spatial variations in VPR gradients can occur. The spatial adjustment is clearly more successful in adjusting the radar rainfall depths and results in a data set with a spatially homogeneous quality.

Until February of 2001 the results were based on the De Bilt radar only. Some hardware calibration issues were addressed, such as the exclusion of radar data because of an elevation bias and the identification of systematically lower radar rainfall depths from the middle of 2004 caused by a sudden change in the calibration of the radar receiver. The radars were not replaced or moved during the 10-yr period, nor was the scanning strategy changed. The effective length of the time series is approximately 8 yr. Verification with rain gauges confirms the quality of the radar precipitation climatology.

If it were available, using a volumetric data set of radar reflectivities would increase the possibilities to improve the quality of QPE. For instance, a VPR correction could be applied using radar reflectivities instead of rain gauges (Vignal et al., 2000; Vignal and Krajewski, 2001). Further, an attenuation correction could be developed using polar data from one elevation. An advantage is that these corrections can be employed in real-time.

This data set is also potentially useful for the investigation of rainfall parameterization in mesoscale weather and climate models and as a test bed for the development of rainfall retrieval algorithms for satellite-based rainfall estimates, such as the Global Precipitation Measurement Mission.

The next step in the use of the radar rainfall climatology is to calculate probabilities of extreme rainfall (e.g., for use in the design of hydraulic structures). This would enable us to study the statistics of extreme areal rainfall for durations of less than 24 h, which is difficult to achieve with rain gauges. Attention will also be given to subhourly rainfall accumulations. Furthermore, statistics of extreme rainfall will be modeled as a function of area size, and regional variability in extreme rainfall will be studied.

## Acknowledgements

The authors gratefully acknowledge the comments given by Remko Uijlenhoet (Hydrology and Quantitative Water Management Group, Wageningen University). We also thank the two anonymous reviewers for their critical comments. Last, we thank Rudolf van Westrhenen (KNMI) for archiving more than 5 yr of radar data.

# Chapter 4

---

## Extreme rainfall analysis and estimation of depth-duration-frequency curves using weather radar<sup>1</sup>

### Abstract

Rain gauge data are often employed to estimate the rainfall depth for a given return period. However, the number of rain gauge records of short-duration rainfall, such as 15 min, is sparse. The obvious advantage of radar data over most rain gauge networks is their higher temporal and spatial resolution. Furthermore, the current quality of quantitative precipitation estimation with radar and the length of the available time series make it feasible to calculate radar-based extreme rainfall statistics. In this chapter an 11-year radar data set of precipitation depths for durations of 15 min to 24 h is derived for the Netherlands ( $3.55 \times 10^4 \text{ km}^2$ ). The radar data are adjusted using rain gauges by combining an hourly mean-field bias adjustment with a daily spatial adjustment. Assuming a Generalized Extreme Value (GEV) distribution, the index flood method is used to describe the distribution of the annual radar rainfall maxima. Regional variability in the GEV location parameter is studied. GEV parameters based on radar and rain gauge data are compared and turn out to be in reasonable agreement. Furthermore, radar rainfall depth-duration-frequency (DDF) curves and their uncertainties are derived and compared with those based on rain gauge data. Although uncertainties become large for long durations, it is shown that radar data are suitable to construct DDF curves.

---

<sup>1</sup>*Water Resources Research*, 2009, doi:10.1029/2009WR007869, **45**, W10424, by Aart Overeem, Adri Buishand and Iwan Holleman.

## 4.1 Introduction

Rain gauge data are often utilized to estimate rainfall depths for given probabilities of exceedance. For example, annual daily rainfall maxima are extracted from a 50-year record and subsequently an extreme value distribution, such as the Generalized Extreme Value (GEV) distribution, is fitted to these annual maxima. Next, the fitted distribution is used to calculate the rainfall depth for a given return period, which is, for instance, of importance for design purposes in water management.

Generally, only rain gauge data are used to obtain statistics of extreme rainfall, often for durations of 24 h or longer. However, the number of rain gauge records of short-duration rainfall, such as 15 min, is sparse. Further, the spatial density of rain gauge networks is often too low to obtain reliable statistics of extreme areal rainfall for subhourly durations.

Although Collier (1989) already mentioned the potential of weather radar data for extreme value analyses and weather radars are nowadays widely used in real-time quantitative precipitation estimation (QPE), radar data have only been used in some studies to derive statistics of extreme rainfall. Durrans et al. (2002) estimated rainfall depth-area relationships for different exceedance frequencies by fitting a Gumbel distribution to annual radar rainfall maxima for durations of 1, 2 and 4 h using an 8-year data set, the largest area size being approximately 1300 km<sup>2</sup>. Allen and DeGaetano (2005b) estimated extreme areal precipitation depths for return periods of 2, 5 and 10 years using a 5-year data set of 24-h accumulated rainfall for New Jersey and North Carolina (United States) for area sizes up to 20 000 km<sup>2</sup>. Lombardo et al. (2006) used radar data to estimate areal reduction factors for durations of 1 to 120 min and return periods of 2 to 50 years for area sizes ranging from 1 to 900 km<sup>2</sup>. The obvious advantage of radar data with respect to most rain gauge networks is their higher temporal and spatial resolution. Further, the current quality of QPE with radar and the length of available time series make it feasible to calculate radar-based extreme rainfall statistics. Possible limitations of the aforementioned studies are heterogeneities caused by continual improvements to the data processing algorithms (Durrans et al., 2002), the small number of levels (13) of daily rainfall accumulations (Allen and DeGaetano, 2005b), and the lack of an adjustment of radar rainfall depths using rain gauges (Lombardo et al., 2006).

In this chapter an 11-year radar data set of precipitation depths for durations of 15 min to 24 h is derived for the Netherlands ( $3.55 \times 10^4$  km<sup>2</sup>), a densely populated country with over 16 million inhabitants. The radar data are adjusted by combining an hourly mean-field bias adjustment using an automatic rain gauge network and a daily spatial adjustment employing a dense manual gauge network. The adjustment procedures and the verification of this data set are described in Chapter 3. The characteristics of annual maximum precipitation depths are investigated for each radar pixel (approximately 6 km<sup>2</sup>). Subsequently, GEV distributions are fitted to these annual maxima to derive the rainfall depths for various return periods. To obtain accurate estimates of the parameters of this distribution from an 11-year

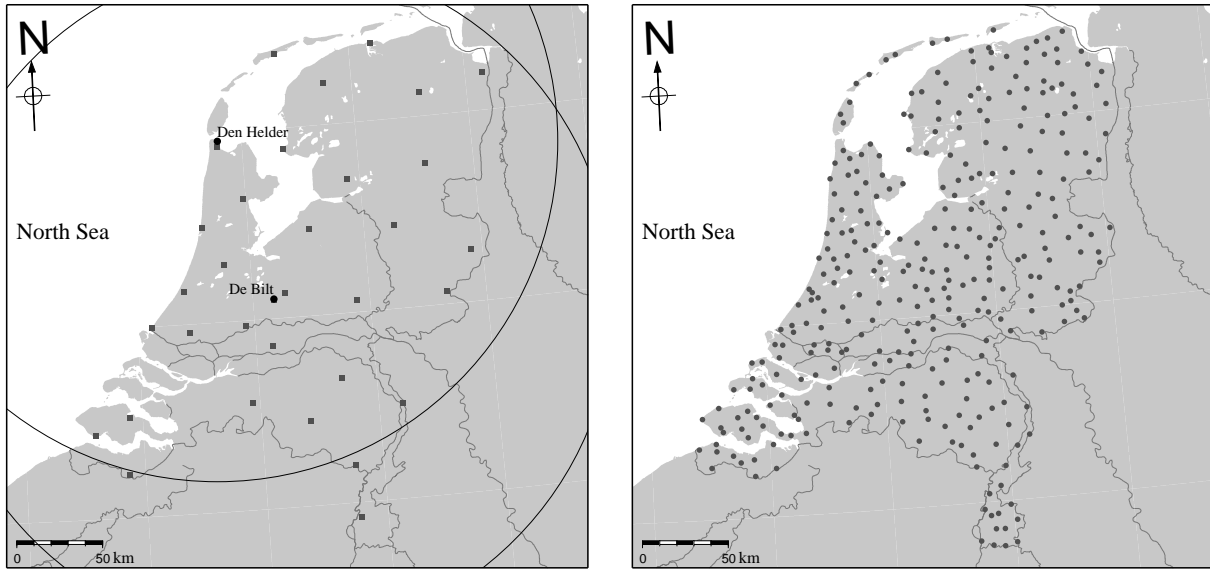


**Figure 4.1:** Maps of the Netherlands with left the locations of the weather radars in De Bilt and Den Helder, their 200-km range (circles), and the 33 automatic rain gauges (squares) and right the locations of the 326 manual rain gauges.

data set, the index flood method is applied. This method assumes that only the GEV location parameter varies spatially. A comparison is made between the parameters of the GEV distribution based on radar and on gauge data. Further, rainfall depth-duration-frequency (DDF) curves are derived. DDF curves describe rainfall depth as a function of duration for given return periods or probabilities of exceedance. To the authors' knowledge, this study is the first in which DDF curves are derived from radar data. The DDF curves and their uncertainties are calculated following a similar approach as developed in Chapter 2.

This chapter is organized as follows. Section 4.2 gives a description of the radar and rain gauge data. In Section 4.3 a data set of adjusted radar-derived rainfall accumulations is constructed. Some characteristics of annual maxima are discussed in Section 4.4. In Section 4.5 regional variability in extreme rainfall statistics is studied. In Section 4.6 extreme rainfall statistics based on radar and on gauge data are compared. GEV parameters are modeled as a function of duration in Section 4.7 to derive radar-based DDF curves and their uncertainties in Section 4.8. The chapter ends with a discussion and conclusions.

## 4.2 Radar and rain gauge data

A weather radar transmits radio-frequency waves into the atmosphere and receives the reflected signals from hydrometeors as echo powers, from which reflectivity factors are calculated. From 1998 to 2008, horizontal cross sections of radar reflectivity factor at constant altitude, called pseudo constant altitude plan position indicators (pseudo CAPPI), were obtained from the two C-band Doppler weather radars in the Netherlands. The radars, which are operated by the Royal Netherlands Meteorological Institute (KNMI), are located in De

Bilt (52.10° N, 5.18° E, 44 m above mean sea level) and Den Helder (52.96° N, 4.79° E, 51 m above mean sea level; see Figure 4.1). Ground clutter was removed from the pseudo CAPPI images, which have a 2.4-km horizontal resolution and a 5-min temporal resolution, using the procedure described in Holleman and Beekhuis (2005). To suppress echoes caused by hail or strong residual ground clutter, reflectivities above 55 dBZ ( $\approx 100 \text{ mm h}^{-1}$ ) were set to 55 dBZ. A rainfall intensity of  $96 \text{ mm h}^{-1}$  is exceeded approximately once in 6.6 years at an arbitrary pixel. Next, rainfall intensities  $R$  ( $\text{mm h}^{-1}$ ) were calculated from the reflectivity factors  $Z$  ( $\text{mm}^6 \text{ m}^{-3}$ ) with a fixed  $Z$ - $R$  relationship (Marshall et al., 1955),

$$Z = 200R^{1.6}. \quad (4.1)$$

The obtained rainfall intensities range from 0.1 to  $100 \text{ mm h}^{-1}$  and have a resolution of 97 levels. Subsequently, 1-h rainfall depths were derived from rainfall intensities for each clock-hour if at least 10 images (minimum availability of 83.3%) were available. A five-pixel median filter on nearest-neighbor pixels was applied to the depths to remove local outliers caused by accumulated residual ground clutter. The range of the radar accumulation images was limited to 200 km and the data were corrected for occultation due to tall buildings in the vicinity of the radar. Accumulation images from the individual radars were combined into one composite using a weighting factor depending on the range from the radar. Chapter 3 gives a more elaborate description of the radar data set based on 1998-2007, but do not derive subhourly rainfall accumulations. The present chapter uses the same methodology to also obtain adjusted 5-min rainfall data. Only those 5-min data were selected for which the corresponding 1-h depth (for a clock-hour) was available. The data set of composites covers the entire land surface of the Netherlands ( $\approx 3.55 \times 10^4 \text{ km}^2$ ) and has an effective length of approximately 9 years, of which 3 years are based on the De Bilt radar only.

In this chapter, rain gauges, which are considered to produce accurate point measurements, are used to improve the quality of QPE with radar. Data from an automatic network of 33 rain gauges ( $\approx 1$  station per  $1000 \text{ km}^2$ ) and a manual network of 326 rain gauges ( $\approx 1$  station per  $100 \text{ km}^2$ ) were employed. Figure 4.1 displays the locations of the rain gauges. The automatic rain gauges measured 1-h rainfall depths for each clock-hour, while from the manual rain gauges 24-h 08-08 UTC rainfall depths were obtained. For more details on the rain gauge networks, see Chapter 3.

### 4.3 Adjustment of radar-based rainfall depths

#### 4.3.1 Adjustment method

A radar indirectly measures rainfall intensities at heights of a few hundred meters to several kilometers above ground level. This may give rise to errors in QPE with radar, such as those caused by a nonuniform vertical profile of reflectivity or variability of the drop-size distribution. Besides, the radar signal is attenuated in the case of strong precipitation or a wet radome. Therefore, it is necessary to adjust the radar data to derive a high-quality radar-based rainfall climatology. A detailed discussion of QPE with radar and their associated

errors can be found in Joss and Waldvogel (1990) and Doviak and Zrnić (1993).

The methods used to adjust the radar rainfall depths are described in detail in Chapter 3. They show that combining an hourly mean-field bias adjustment with a daily spatial adjustment results in high-quality 1- to 24-h radar rainfall depths (for each clock-hour). The manual gauge network is used to apply a spatial adjustment to the unadjusted 24-h 08 UTC rainfall depths. A spatial adjustment factor field is calculated by dividing the interpolated manual gauge precipitation depths  $G$  by the corresponding interpolated raw radar precipitation depths  $R_{\text{raw}}^c$ :

$$F_S^c(i, j) = \frac{\sum_{n=1}^N w_n(i, j) \times G(i_n, j_n)}{\sum_{n=1}^N w_n(i, j) \times R_{\text{raw}}^c(i_n, j_n)}, \quad (4.2)$$

with  $S$  denoting the spatial adjustment method,  $c$  composite,  $N$  the number of radar-gauge pairs,  $(i_n, j_n)$  the image coordinates of rain gauge  $n$ , and  $w_n(i, j)$  a weighting function, given by (Barnes, 1964):

$$w_n(i, j) = \exp[-d_n^2(i, j)/\sigma^2], \quad (4.3)$$

where  $\sigma$  ( $= 12$  km) determines the smoothness of the  $F_S^c$  field and  $d_n(i, j)$  is the distance between manual rain gauge  $n$  and pixel  $(i, j)$ . Adjusted 24-h 08 UTC radar rainfall depths are obtained by multiplying the unadjusted radar rainfall depths with the spatial adjustment factor field.

Automatic rain gauges are utilized for a mean-field bias adjustment factor  $\bar{G}/\bar{R}_{\text{raw}}^c$  of the 1-h raw radar rainfall depths, where  $\bar{G}$  and  $\bar{R}_{\text{raw}}^c$  are the gauge and radar rainfall depths averaged over all automatic rain gauge locations for the clock-hour of interest (Holleman, 2007). Subsequently, for each 24-h 08 UTC interval the 1-h mean-field bias adjusted rainfall depths at each pixel are multiplied by a factor so that their 24-h 08 UTC accumulations correspond with the spatially adjusted 24-h 08 UTC depths. This results in both mean-field bias and spatially (MFBS) adjusted 1-h rainfall depths for every clock-hour. Finally, the 1-h rainfall depths are employed to construct 4-, 8-, 12- and 24-h depths for each clock-hour.

#### 4.3.2 Derivation of adjusted 15-min to 120-min composites

In this chapter the adjustment is extended to 5-min rainfall data, which are available for 288 time steps per day, such as 2300, 2305 UTC, etcetera. The raw 5-min composited rainfall data are accumulated to 1-h rainfall depths for each clock-hour. Subsequently, at each pixel the mean-field bias and spatially adjusted 1-h rainfall depth  $R_{\text{MFBS}}^{c,1h}$  is divided by the corresponding unadjusted depth, resulting in an adjustment factor field:

$$F_{\text{MFBS}}^{c,1h}(i, j) = R_{\text{MFBS}}^{c,1h}(i, j) / R_{\text{raw}}^{c,1h}(i, j). \quad (4.4)$$

Then, the 5-min unadjusted rainfall data are multiplied with this adjustment factor field to obtain both mean-field bias and spatially adjusted 5-min rainfall data:

$$R_{\text{MFBS}}^{c,5\text{min}}(i, j) = R_{\text{raw}}^{c,5\text{min}}(i, j) \times F_{\text{MFBS}}^{c,1h}(i, j). \quad (4.5)$$

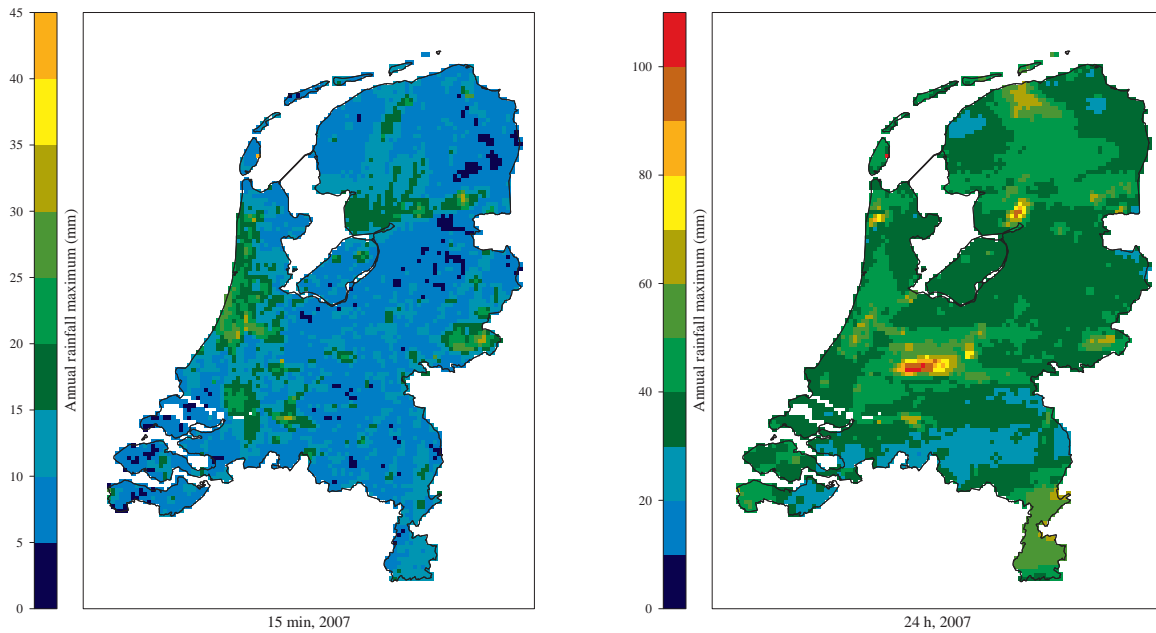


**Figure 4.2:** Annual MFBS-adjusted radar rainfall maxima for the Netherlands for durations of 15 min (left) and 24 h (right) for the year 2007.

From these 5-min composites of rainfall data, depths for durations of 15, 30, 60 and 120 min are obtained for each 5 min. In the derivation of extreme rainfall statistics, the 5-min extremes are not taken into account. This is because of an upper bound of 8.3 mm (corresponding with a reflectivity of 55 dBZ) of the raw 5-min data.

#### 4.4 Characteristics of annual maxima

The Netherlands, which is located at the midlatitudes, has a temperate climate with prevailing westerly winds and is a flat country with only small areas higher than 50 m above mean sea level. Regional differences in rainfall are small mainly because there is almost no orographic forcing. For example, mean annual rainfall varies spatially from 675 to 925 mm and in Chapter 2 regional variability in extreme rainfall statistics could not be found using annual rainfall maxima from 12 automatic rain gauges distributed over the Netherlands. Another study, based on 55 years of annual daily rainfall maxima from 141 manual rain gauges, shows that regional differences in extreme rainfall quantiles in the Netherlands are statistically significant, but relatively small. Roughly, these quantiles are 5-10% smaller for the 15% driest areas and approximately 15% larger for the 2% wettest areas compared to the countrywide-averaged quantiles (Buishand et al., 2009).

Radar provides new possibilities to investigate the date and timing of rainfall at high spatial resolutions over large areas. For example, Carbone and Tuttle (2008) studied the diurnal cycle of warm-season rainfall over the U.S. mainland using radar data from 12 seasons (May through August). In the current chapter, attention is given specifically to the date and timing



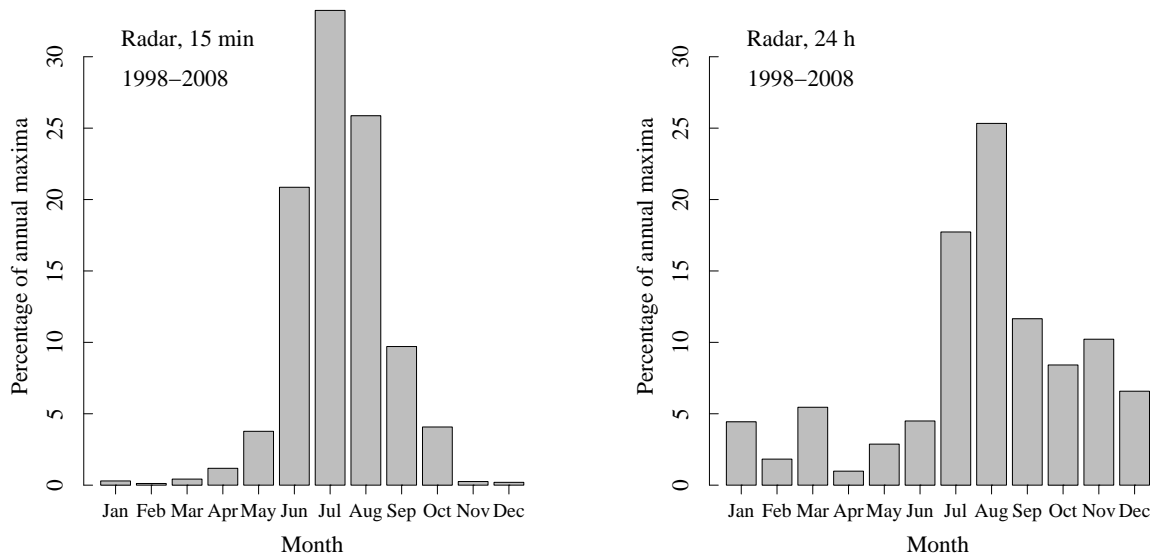


**Figure 4.3:** Frequency of occurrence of the 15-min and 24-h annual maxima in the period 1998-2008 over the land surface of the Netherlands for each calendar month. Based on 68 090 annual maxima.

of annual rainfall maxima for each radar pixel above the land surface of the Netherlands. In total 6190 (number of pixels) times 11 (number of years) annual rainfall maxima are available. Running MFBS-adjusted annual maxima are abstracted for durations  $D$  of 15, 30, 60 and 120 min and 4, 8, 12 and 24 h. Running implies here that the 4-h to 24-h rainfall amounts are calculated for each clock-hour of the year and the 15-min to 120-min rainfall amounts for each 5 min of the year (0600 UTC, 0605 UTC, etcetera). Figure 4.2 shows annual radar rainfall maxima for the Netherlands for  $D = 15$  min and 24 h for the year 2007. The figure illustrates that spatial variation in annual rainfall maxima can be quite large: 3 to 42 mm for  $D = 15$  min and 19 to 106 mm for  $D = 24$  h.

Figure 4.3 shows in which calendar months most annual maxima occurred during the period 1998-2008. Approximately 87% of the annual 60-min (not shown) and 90% of the 15-min rainfall maxima are observed in the period June to September, when convection contributes substantially to the formation of precipitation. For the 24-h rainfall depths the annual maxima are distributed more evenly over the year, with most events observed in the period July to December. At this timescale, stratiform rainfall becomes more important for annual maxima.

Figure 4.4 displays the percentage of annual 15-min and 60-min maxima for each clock-hour. In summer, convection plays an important role in the development of showers during the course of the day and reaches a maximum at the end of the afternoon. This is in agreement with Figure 4.4 which shows that most annual maxima occur between 1300 and 2100 UTC

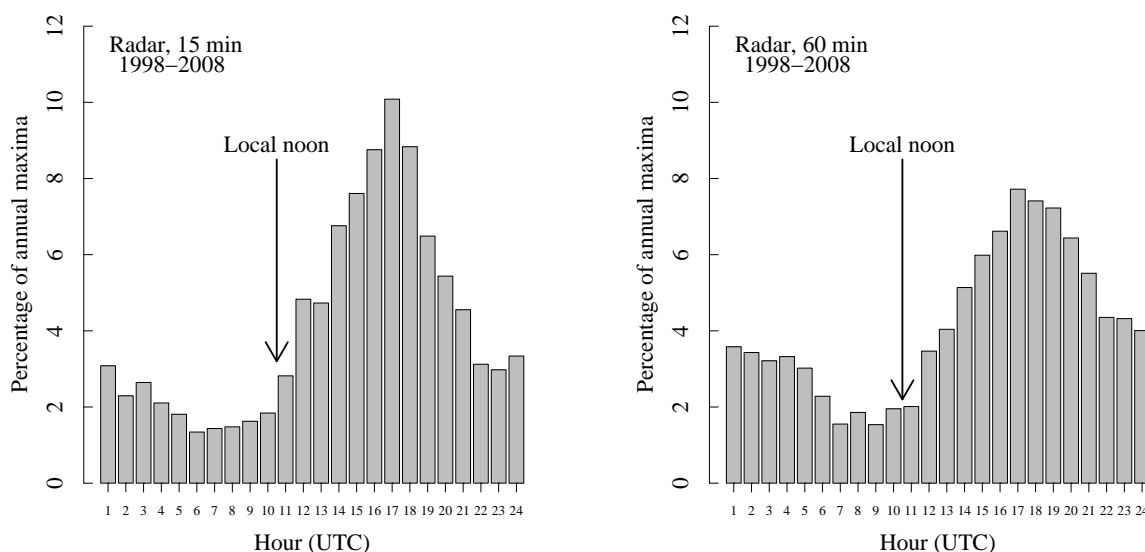


**Figure 4.4:** Timing of the 15-min and 60-min annual rainfall maxima over the land surface of the Netherlands in the period 1998-2008. For each clock-hour, the percentage of annual maxima is displayed. Based on 68 090 annual maxima.

(in summer 3 to 11 h after local noon).

For each pixel, the average date of occurrence of the annual maxima in 1998-2008 is calculated. The spatial distribution of the average dates is shown in Figure 4.5. No clear spatial pattern in average dates can be distinguished for 15-min annual maxima. It is apparent that the 24-h rainfall maxima usually occur later in the year for the coastal areas (the North Sea is indicated in Figure 4.1), in September. This can be related to a coastal effect: the sea surface temperatures are highest in September, which may lead to more intensive rainfall. Finally, it appears that 74.8% of the annual 24-h 08 UTC maxima based on radar data occurred on the same date as those measured by the manual rain gauges.

The average data availability is approximately 80%, this may result in lower annual rainfall maxima. However, the data availability is on average higher from June to September, 90%, and in this period most annual rainfall maxima are observed (see Figure 4.3). The influence of missing data was investigated theoretically. The GEV distribution for annual maxima is related to the Generalized Pareto Distribution, which describes the distribution of exceedances of a high threshold in the associated peak-over-threshold model. The number of exceedances of the threshold in a year follows a Poisson distribution. By combining these models and reducing the mean number of exceedances with 10%, it turned out that the influence of 10% missing data on the location parameter and the dispersion coefficient

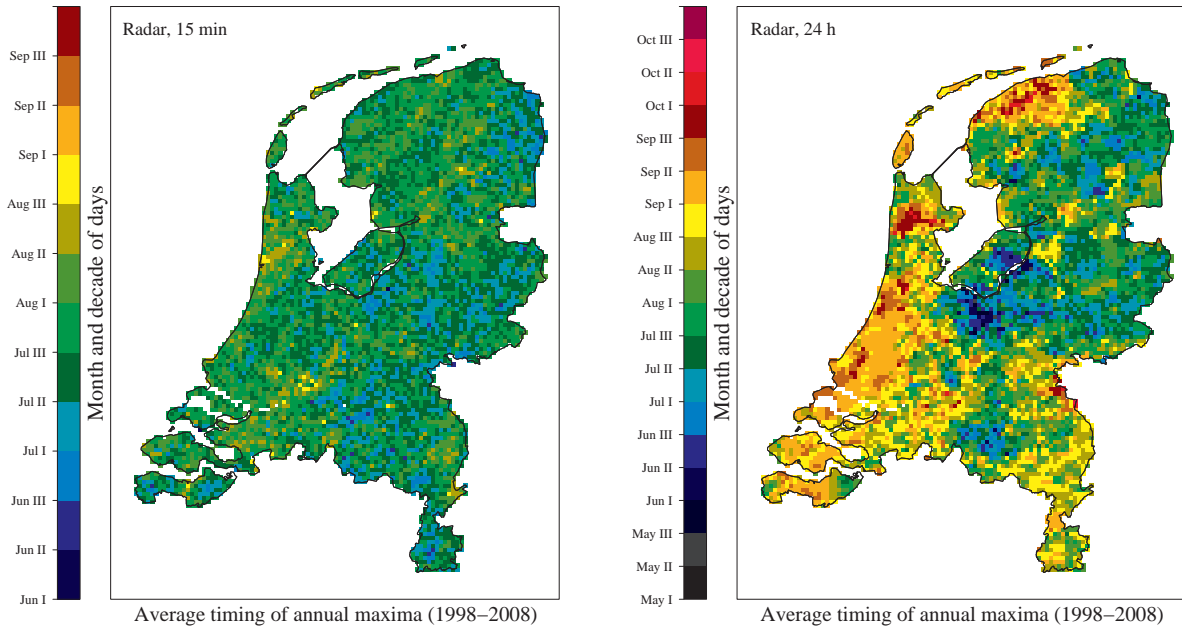


**Figure 4.5:** Average dates of occurrence of the 15-min and 24-h annual rainfall maxima during the period 1998–2008 for each pixel located above the land surface of the Netherlands.

of the extreme value distribution is small (less than 4%)<sup>2</sup>.

## 4.5 Regional variability in extreme rainfall statistics

### 4.5.1 Fitting a GEV distribution

The GEV distribution has been applied frequently to model rainfall maxima and consists of the three types of extreme value distributions. This type is determined by the value of the shape parameter  $\kappa$ . The GEV cumulative distribution function  $F(x)$  is given by (Jenkinson, 1955):

$$F(x) = \exp\left\{-\left[1 - \frac{\kappa}{\alpha}(x - \mu)\right]^{1/\kappa}\right\} \text{ for } \kappa \neq 0, \quad (4.6)$$

$$F(x) = \exp\left\{-\exp\left[-\frac{1}{\alpha}(x - \mu)\right]\right\} \text{ for } \kappa = 0, \quad (4.7)$$

with  $\mu$  the location,  $\alpha$  the scale and  $\kappa$  the shape parameter of the distribution. If  $\kappa = 0$  the Gumbel distribution is obtained (Eq. (4.7)).

The quantile function, the inverse of Eqs. (4.6) and (4.7), is given by:

$$x(T) = \mu + \frac{\alpha \{1 - [-\ln(1 - T^{-1})]^\kappa\}}{\kappa} \text{ for } \kappa \neq 0, \quad (4.8)$$

$$x(T) = \mu - \alpha \ln[-\ln(1 - T^{-1})] \text{ for } \kappa = 0, \quad (4.9)$$

<sup>2</sup>For a more complete description of the methodology and the outcome of this theoretical study, see Appendix C, which was not incorporated in the article.

where  $T = 1/(1 - F)$  is the return period.

Fitting a GEV distribution to annual maxima is a well-established method to describe the distribution of extreme rainfall. A problem, however, with fitting this distribution to data from a single rainfall station or radar pixel is that the resulting quantile estimators have large variance and may be seriously biased. In order to increase the accuracy of these estimates, a regional frequency analysis can be applied, assuming that certain distribution parameters are constant over the region of interest. The increased accuracy of quantile estimates results from the increased precision of the estimates of the common parameters from the pooled annual maxima across the region. The most restrictive assumption for the radar data set in this chapter would be that the three GEV parameters are constant over the Netherlands. The results in Section 4.4, however, indicate that this assumption may not be appropriate. Somewhat less restrictive is the index flood assumption that the underlying frequency distributions are identical apart from a scaling factor, the index flood. This assumption implies that  $\kappa$  and the dispersion coefficient  $\gamma = \alpha/\mu$  are constant over the region of interest. The index flood method has often been applied in regional frequency analysis (Gellens, 2002; Fowler and Kilsby, 2003; Mora et al., 2005).

The use of L-moments has become a popular means to estimate distribution parameters from pooled annual maxima (Hosking and Wallis, 1997; Fowler and Kilsby, 2003). Though L-moments estimates are known to exhibit relatively little bias in the case of short records, this bias may not be negligible for records as short as 11 years. An alternative is to maximize a likelihood function constructed under the assumption of spatial independence (Buishand, 1991; Sveinsson et al., 2001). In the case that the three GEV parameters are constant over the Netherlands, this likelihood function is given by:

$$L(\mu, \gamma, \kappa) = \sum_{s=1}^S L_s(\mu, \gamma, \kappa), \quad (4.10)$$

where  $L_s$  is the log-likelihood for the annual maxima for a given duration  $D$  at site or pixel  $s$ , and  $S = 6190$  is the number of sites or pixels. Maximizing  $L(\mu, \gamma, \kappa)$  with respect to  $\mu$ ,  $\gamma$  and  $\kappa$  gives the maximum likelihood estimates  $\hat{\mu}$ ,  $\hat{\gamma}$  and  $\hat{\kappa}$ . In the case of the index flood assumption the location parameter  $\mu$  is re-estimated for each site by maximizing  $L_s(\mu_s, \hat{\gamma}, \hat{\kappa})$  with respect to  $\mu_s$ . A small simulation study shows that further maximization of the likelihood function does not result in better parameter estimates and that popular L-moments estimates of  $\kappa$  are considerably biased for 11-year records (Appendix B).

Figure 4.6 shows two examples of a GEV distribution fitted to 6190 times 11 annual maxima for  $D = 15$  min and 24 h. Here it is assumed that all GEV parameters are constant over the Netherlands. The annual maxima are ordered and plotted using the Gringorten plotting position (Gringorten, 1963). The GEV distribution fits well for return periods up to  $T = 100$  years. Especially for  $D = 24$  h, an offset is found beyond  $T = 100$  years. This offset is largely due to the vulnerability of order statistics to spatial correlation. For  $D = 15$  min,

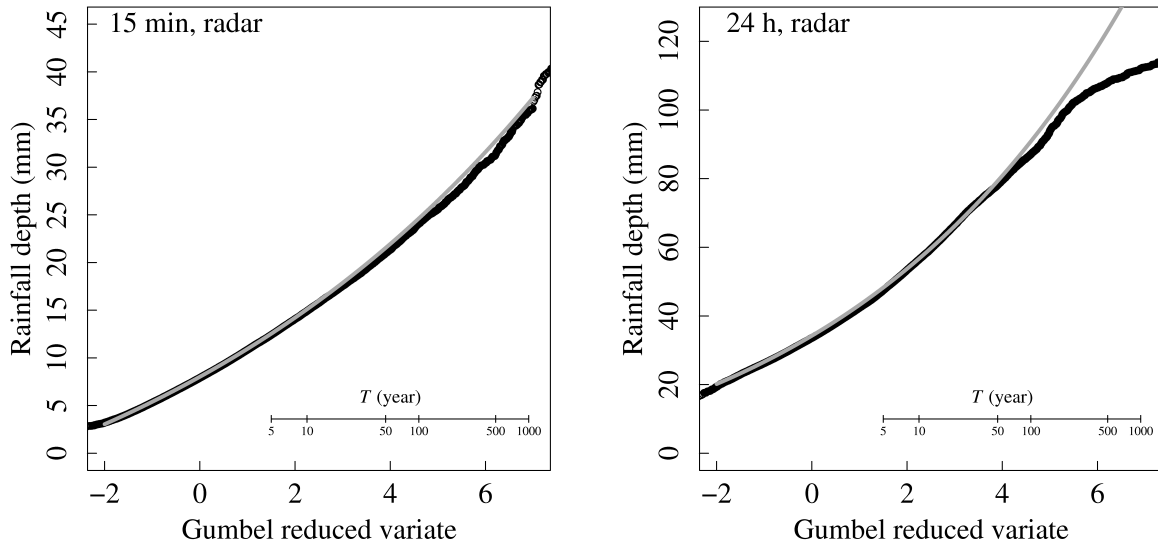


**Figure 4.6:** Gumbel probability plots of the GEV distribution fitted to annual 15-min (left) and annual 24-h (right) radar rainfall maxima. Ordered annual maxima (black) have been plotted using the Gringorten plotting position; gray lines represent GEV fits. The Gumbel reduced variate is defined as  $-\ln(-\ln F)$  with  $F$  the GEV cumulative distribution function.

there is no clear offset because of the lower spatial correlation for this duration. Because of spatial correlation, extremes tend to be smaller compared to a spatially uncorrelated data set. Plotting of spatially correlated data is, for instance, discussed by Reed et al. (1999).

The upward curvature of the fitted distributions in Figure 4.6 is characteristic of a GEV distribution with a negative shape parameter  $\kappa$  (Fréchet type) and is often found for  $D \leq 24$  h, e.g. Koutsoyiannis (2004) and Chapter 2.

#### 4.5.2 Bootstrap samples

Another consequence of spatial dependence is that usual methods to derive standard errors and confidence intervals from the likelihood function no longer apply. The bootstrap is a technique that can account for spatial correlation. This is achieved by resampling year numbers with replacement rather than the annual maximum rainfalls from individual pixels (GREHYS, 1996; Faulkner and Jones, 1999). Bootstrap samples are created as follows in this chapter:

- Draw a random sample with replacement from the series of year numbers 1998, ..., 2008.
- Select the annual maxima of the 6190 pixels above the land surface of the Netherlands for the sampled year numbers for  $D = 15, 30, 60$  and  $120$  min and  $D = 4, 8, 12$  and  $24$  h. This leads to one bootstrap sample of 11 years of annual maxima for each  $D$ . Each bootstrap sample consists of 11 times 6190 annual maxima.

- Repeat this 1000 times.

Each time that the bootstrap is used to estimate, for example, standard deviations of the estimated GEV parameters, the same 1000 bootstrap samples are employed.

#### 4.5.3 Test for regional variability in $\mu$

In this section, the regional variability in the GEV location parameter  $\mu$  is tested. The test is limited to 326 sites distributed evenly over the Netherlands, at the locations of the manual rain gauges, which are shown in Figure 4.1.

Rather than  $\mu$ , the transformed parameter  $\theta = \ln \mu$  is considered, partly because  $\ln \mu$  is modeled as a function of  $D$  in Section 4.7.2. From the bootstrap samples in Section 4.5.2, 1000 estimates of  $\theta$  are available for each site. These estimates are ranked in nondecreasing order  $\theta_{(1)}^* \leq \theta_{(2)}^* \leq \dots \leq \theta_{(1000)}^*$ . Subsequently, for each rank  $r$ , the 326 values of  $\theta_{(r)}^*$  are averaged. Figure 4.7 shows normal probability plots of these average ranked values for  $D = 15$  min, 60 min and 24 h, from which it can be concluded that  $\hat{\theta} = \ln \hat{\mu}$  is approximately normally distributed.

A technical difficulty with testing for regional differences in the GEV location parameter is that the estimates of this parameter are spatially correlated due to the spatial correlation of the annual rainfall maxima. This correlation has to be taken into account in the test. Let  $\theta_i$  be the transformed parameter  $\ln \mu$  at site  $i$ ,  $\hat{\theta}_i$  its maximum likelihood estimate and  $\hat{\theta}$  the vector of the 326  $\hat{\theta}_i$ s. The hypothesis  $\theta_1 = \dots = \theta_{326} = \theta$  can be tested with the statistic (Witter, 1984):

$$T_1 = (\hat{\theta} - \hat{\theta}_{GLS}\mathbf{s})^T \mathbf{C}^{-1} (\hat{\theta} - \hat{\theta}_{GLS}\mathbf{s}), \quad (4.11)$$

with  $\hat{\theta}_{GLS}$  the generalized least squares estimate of  $\theta$ :

$$\hat{\theta}_{GLS} = \frac{\mathbf{s}^T \mathbf{C}^{-1} \hat{\theta}}{\mathbf{s}^T \mathbf{C}^{-1} \mathbf{s}}, \quad (4.12)$$

**Table 4.1:** Values of the statistic  $T_1$  and the corresponding  $p$ -values for testing regional differences in the GEV parameter  $\mu$ ; also given are the  $p$ -values in the case of a fixed  $s_0$  of 0.5.

$D$	$T_1$	$p$ -value	$p$ -value ( $s_0 = 0.5$ )
15 min	429	$8.9 \times 10^{-5}$	$1.6 \times 10^{-4}$
30 min	437	$3.0 \times 10^{-5}$	$9.0 \times 10^{-6}$
60 min	377	$2.4 \times 10^{-2}$	$3.5 \times 10^{-3}$
120 min	354	$1.3 \times 10^{-1}$	$4.1 \times 10^{-2}$
4 h	342	$2.5 \times 10^{-1}$	$4.3 \times 10^{-1}$
8 h	394	$5.2 \times 10^{-3}$	$3.2 \times 10^{-2}$
12 h	402	$2.3 \times 10^{-3}$	$7.1 \times 10^{-3}$
24 h	426	$1.3 \times 10^{-4}$	$1.7 \times 10^{-2}$

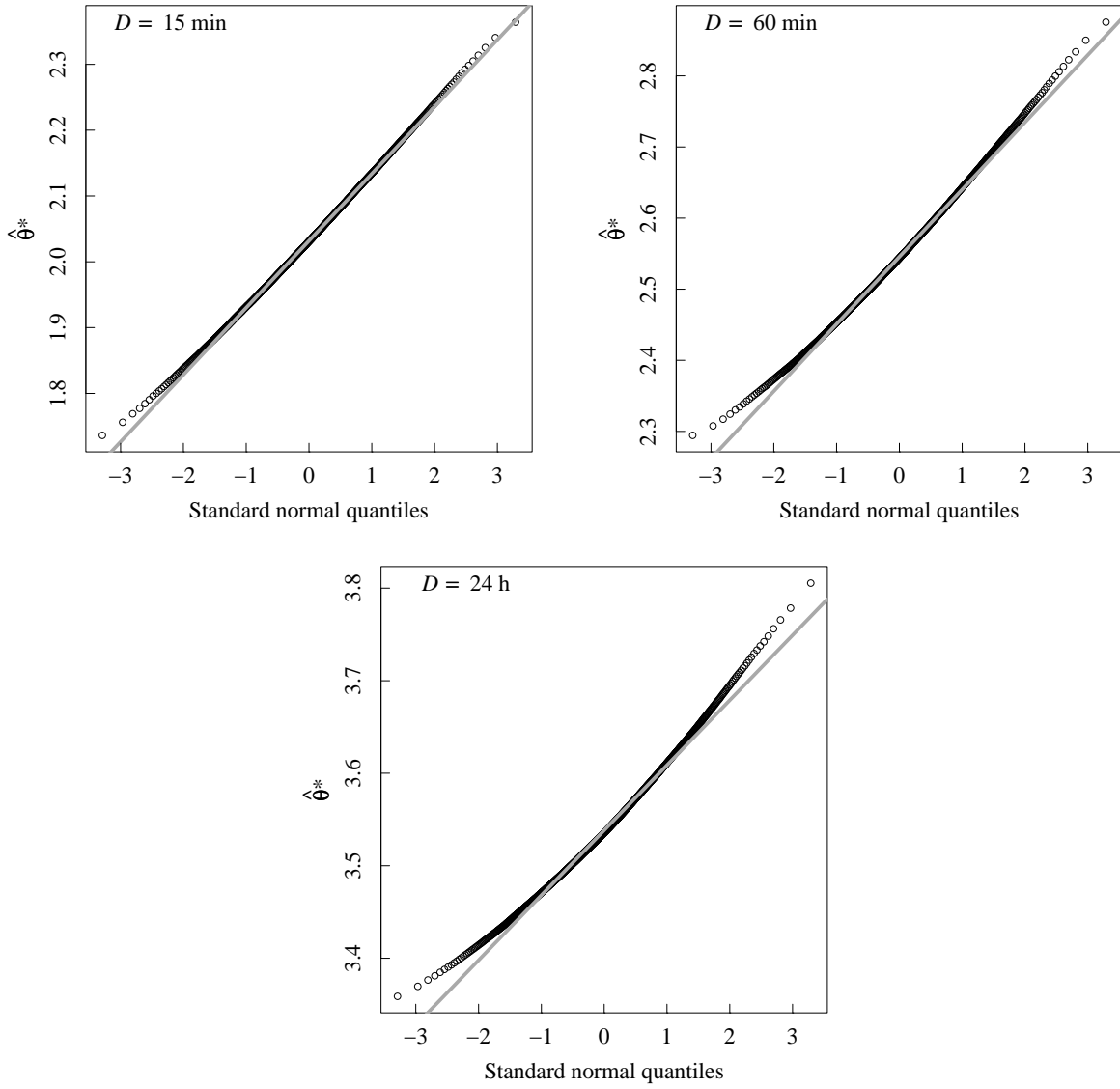


**Figure 4.7:** Normal probability plot of bootstrap estimates  $\hat{\theta}^*$  of  $\theta = \ln(\mu)$  for  $D = 15 \text{ min}$ ,  $60 \text{ min}$  and  $24 \text{ h}$ , averaged over 326 sites.

where  $\mathbf{C}$  is the covariance matrix of  $\hat{\boldsymbol{\theta}}$  and  $\mathbf{s}$  is a vector consisting of 326 ones.  $T_1$  has a chi-square distribution with 325 degrees of freedom under the hypothesis  $\theta_1 = \theta_2 = \dots = \theta_{326}$  provided that the  $\hat{\theta}_i$ s have a multivariate normal distribution and  $\mathbf{C}$  is known. If the elements of  $\mathbf{C}$  are estimated from the data, the chi-square distribution holds only approximately. In this chapter the variances on the main diagonal of  $\mathbf{C}$  are obtained as the averages of the bootstrap variances of the  $\hat{\theta}_i$ s for the 326 sites and the off-diagonal elements are derived from the bootstrap estimates of the cross correlations between the  $\hat{\theta}_i$ s. These estimated cross correlations exhibit large variability as can be seen from Figure 4.8 for  $D = 15 \text{ min}$ ,  $60 \text{ min}$  and  $24 \text{ h}$ . For the validity of the chi-square distribution of the test statistic, it is im-

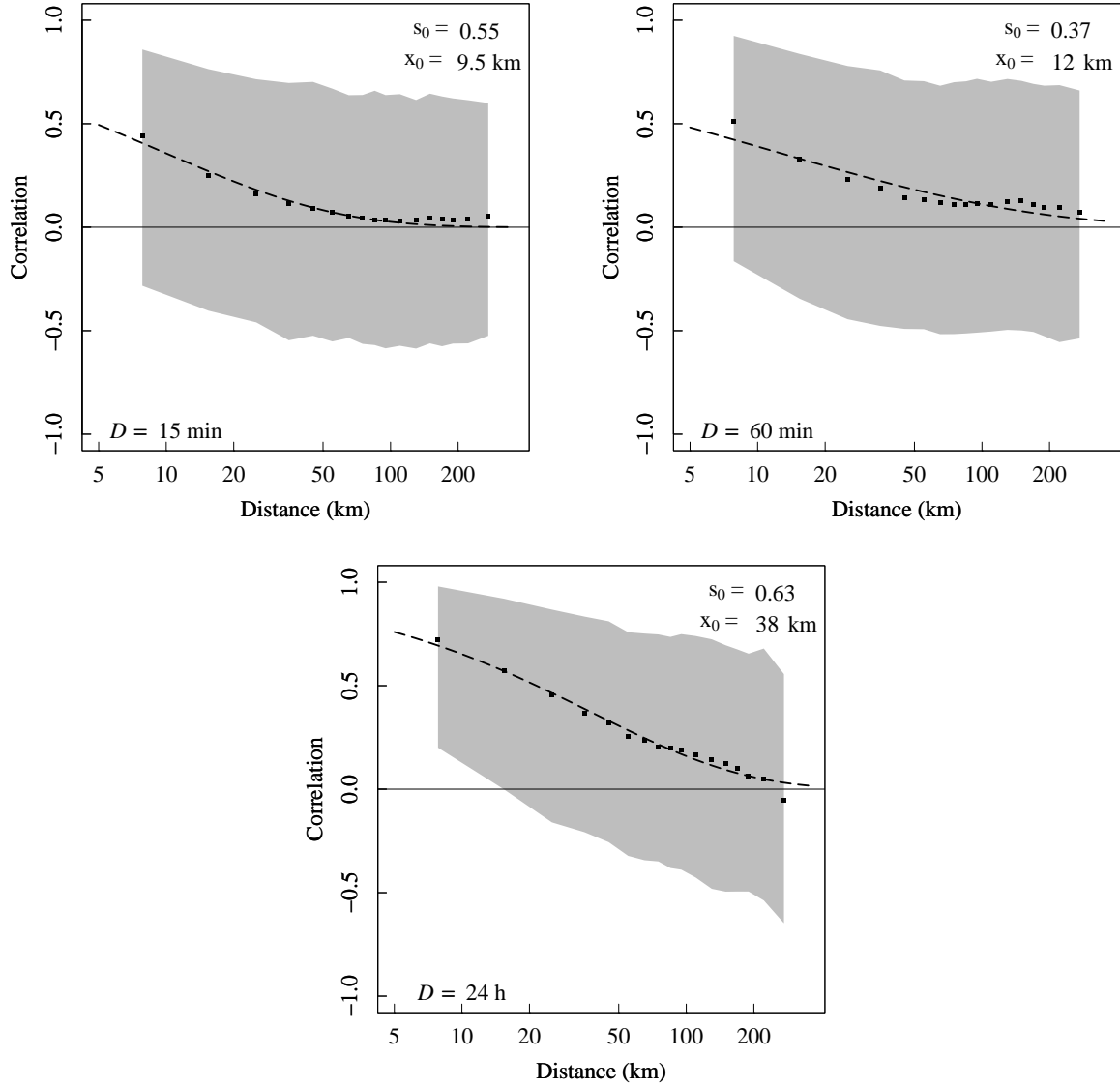


**Figure 4.8:** Correlation between the maximum likelihood estimates  $\hat{\theta}_i$  of  $\ln \mu$  as a function of distance for  $D = 15 \text{ min}$ ,  $60 \text{ min}$  and  $24 \text{ h}$ . The squares represent the average correlation coefficients for each distance class. The dashed line is an exponential curve fitted to these average correlation coefficients. The gray-shaded area contains for each distance interval 95% of the correlation coefficients.

portant to reduce the variance of the elements of  $\mathbf{C}$ . Therefore, average cross correlation coefficients are calculated for 17 distance classes. Subsequently, the following exponential model is fitted to these averaged correlation coefficients using nonlinear least squares:

$$\rho(x) = \exp \left[ - \left( \frac{x}{x_0} \right)^{s_0} \right], \quad (4.13)$$

where  $\rho(x)$  is the correlation at intersite distance  $x$  (km),  $x_0$  a scale parameter (km) and  $s_0$  a



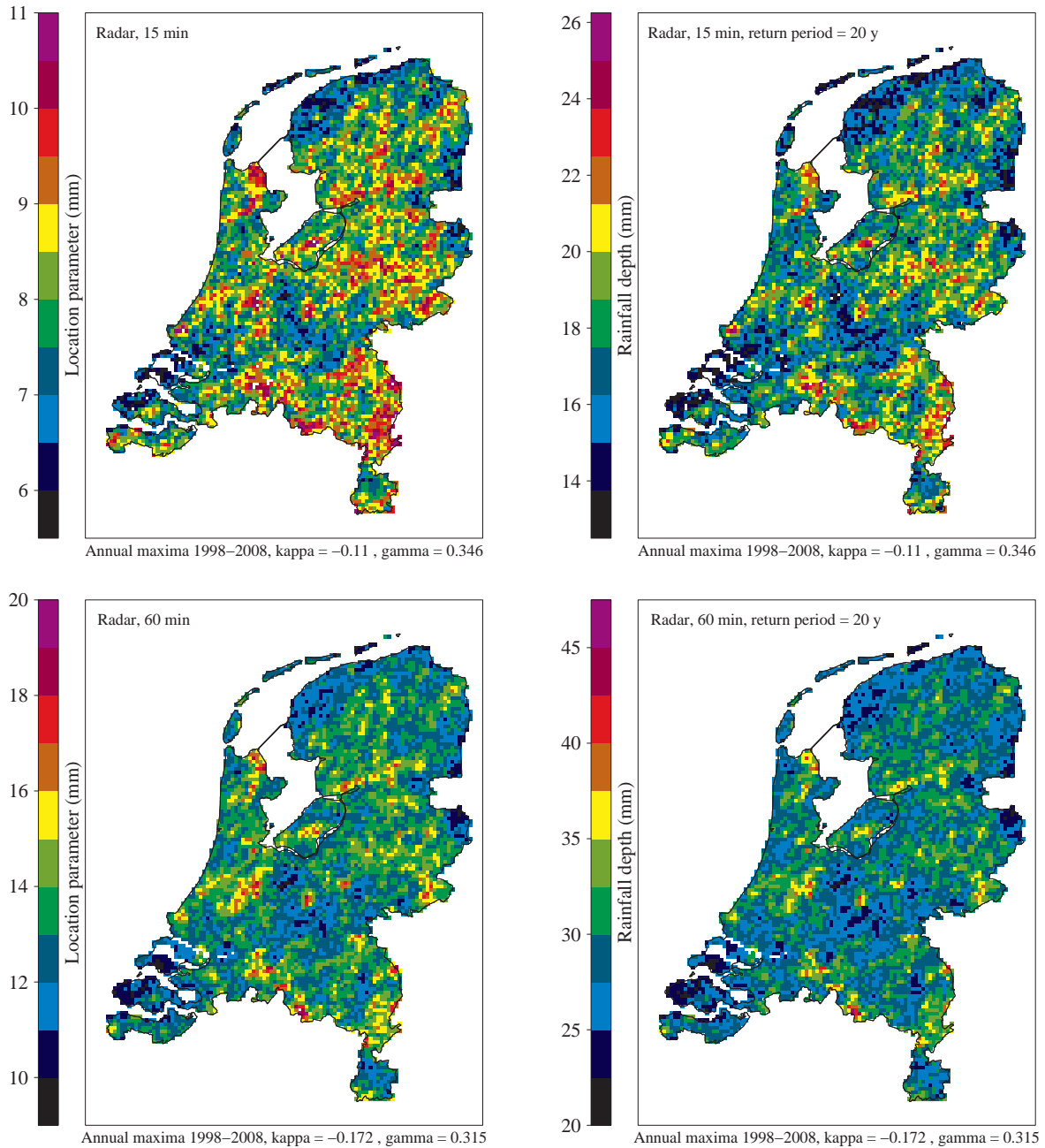


**Figure 4.9:** The location parameter (left) and the rainfall depth for a return period of 20 years (right) for  $D = 15$  min, 60 min and 24 h for each pixel in the Netherlands (*continued on next page*).

shape parameter. The model gives a reasonable description of the decay of  $\rho$  with intersite distance as can be seen in Figure 4.8 for  $D = 15$  min, 60 min and 24 h. The covariances in  $\mathbf{C}$  are calculated by multiplying the variance on the main diagonal with the correlation coefficient obtained from Eq. (4.13).

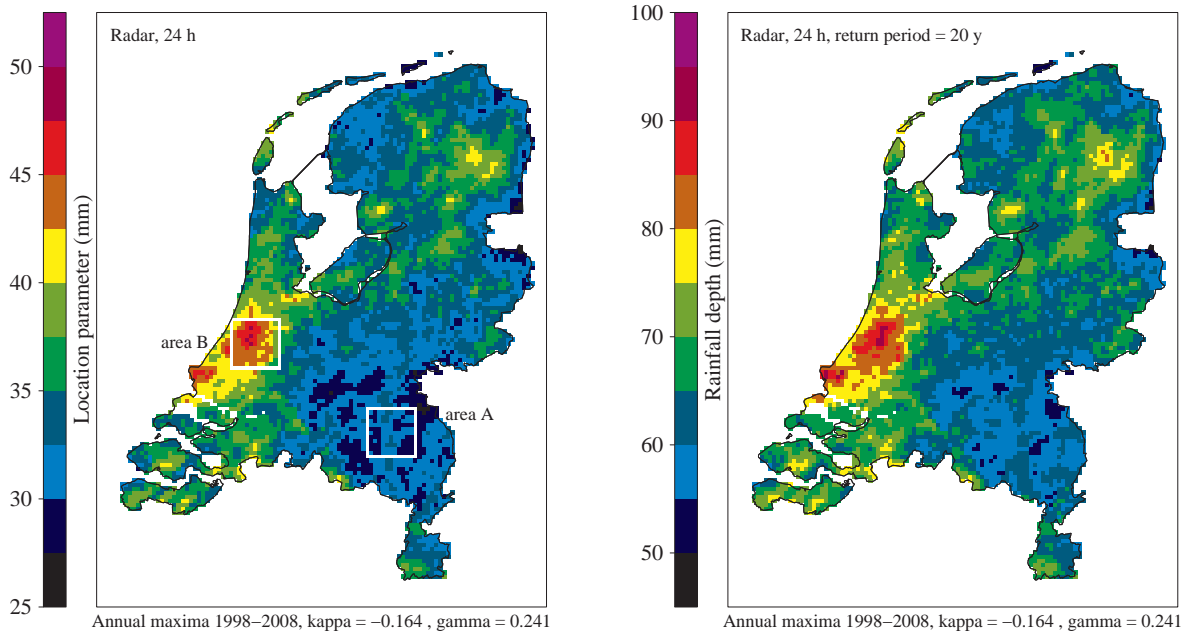


Figure 4.9, continued from previous page

$T_1$  was calculated for  $D = 15, 30, 60$  and  $120$  min and for  $D = 4, 8, 12$  and  $24$  h. Table 4.1 shows that the values of the  $T_1$  statistic are larger than the critical value 368 for a test at the 5% level, except for  $D = 120$  min and  $D = 4$  h. Since spatial differences in  $\ln(\mu)$  are statistically significant, the regional variability in  $\mu$  is also statistically significant.

The shape parameter  $s_0$  in Eq. (4.13) changes irregularly with increasing duration. The value of this parameter fluctuates between 0.37 for  $D = 60$  min and 0.63 for  $D = 24$  h. To limit the variability in the estimated correlation coefficients, a fixed shape parameter can be chosen. The  $p$ -values change considerably if this parameter is fixed at 0.5 for all durations (Table 4.1). However, the same results are obtained for the tests of regional differences in  $\ln \mu$  at the 5% significance level, except for  $D = 120$  min. A drawback of this fixed shape parameter is that the fit to the average correlation coefficients deteriorates.

Figure 4.9 displays the location parameters and the rainfall depths for a return period of 20 years for each pixel above the land surface of the Netherlands. Most noticeable are the high values of  $\mu$  (more than 40 mm) in the western part of the country, near the coast, for  $D = 24$  h, which are considerably larger than those in the rest of the country. For  $D = 24$  h, rainfall depths range from 48 to 94 mm for  $T = 20$  years. For the location parameter several isolated areas with high values can be distinguished for  $D = 15$  and 60 min. Rainfall depths vary from 11 to 27 mm ( $D = 15$  min) and 20 to 47 mm ( $D = 60$  min) for  $T = 20$  years.

Buishand et al. (2009) employed annual daily rainfall maxima obtained from 141 manual rain gauges with a record length of 55 years (1951–2005) to calculate extreme rainfall statistics

for the Netherlands. They also found that the largest values of the location parameter occur in the western part of the country implying that this is not an artifact of the period 1998-2008.

## 4.6 Comparison of radar and rain gauge extreme rainfall statistics

Although the high quality of the adjusted radar data set has been demonstrated in Chapter 3, no attention has been given yet to the verification of annual rainfall maxima. Therefore, GEV parameters based on rain gauge and radar data from the same period (1998-2008) are compared in this section.

Annual maxima are abstracted from the data of 326 manual rain gauges and from the radar data at the corresponding pixels for 1998-2008. Regional differences in the location parameter are negated. GEV parameters are estimated for 24-h 08 UTC rainfall depths, employing maximum likelihood. The same procedure is followed for the annual maxima obtained from 33 automatic gauges for  $D = 1$  and 24 h (clock-hours).

Table 4.2 shows a comparison of the estimated GEV parameters based on rain gauge and radar data. The estimates from the rain gauge data in this chapter refer to 1-h or 24-h intervals for which radar data were available, except for the estimated GEV parameters obtained from Chapter 2 in the last column. The standard deviation of the differences between the radar and rain gauge derived GEV parameters,  $s_{\text{diff}}$ , is calculated to investigate whether differences between radar and rain gauge data are statistically significant. For all durations,

**Table 4.2:** Estimated GEV parameters for  $D = 1$  h, 24 h and 24 h 08 UTC based on rain gauge and radar data with  $n$  denoting the number of annual maxima. The standard deviation of the differences between the radar and rain gauge derived GEV parameters,  $s_{\text{diff}}$ , is estimated with the bootstrap. An asterisk indicates that these differences are larger than  $2 \times s_{\text{diff}}$ .

$D$	$n$	$\hat{\mu}_{\text{gauge}}$ (mm)	$\hat{\mu}_{\text{radar}}$ (mm)	$s_{\text{diff}}$ (mm)	$n$	$\hat{\mu}_{\text{gauge}}^{\text{Chapter2}}$
1 h	358	13.06	11.23	0.22*	514	12.43
24 h	358	33.31	33.67	0.47	514	33.08
24 h 08 UTC	3550	30.82	29.69	0.07*		
$D$	$n$	$\hat{\gamma}_{\text{gauge}}$	$\hat{\gamma}_{\text{radar}}$	$s_{\text{diff}}$	$n$	$\hat{\gamma}_{\text{gauge}}^{\text{Chapter2}}$
1 h	358	0.351	0.326	0.009*	514	0.364
24 h	358	0.268	0.240	0.006*	514	0.253
24 h 08 UTC	3550	0.264	0.252	0.003*		
$D$	$n$	$\hat{\kappa}_{\text{gauge}}$	$\hat{\kappa}_{\text{radar}}$	$s_{\text{diff}}$	$n$	$\hat{\kappa}_{\text{gauge}}^{\text{Chapter2}}$
1 h	358	-0.190	-0.143	0.033	514	-0.127
24 h	358	-0.196	-0.167	0.029	514	-0.117
24 h 08 UTC	3550	-0.154	-0.147	0.012		

$\hat{\kappa}_{\text{gauge}}$  and  $\hat{\kappa}_{\text{radar}}$  differ less than  $1 \times$  or  $2 \times s_{\text{diff}}$ . Further, for the location parameter and the dispersion coefficient the differences between the estimates based on gauge data and those based on radar data are more than  $2 \times s_{\text{diff}}$ , except for the location parameter of the 24-h maxima from the automatic gauges. However, for the manual rain gauges the differences in the estimated values of  $\mu$  and  $\gamma$  are less than 5%.

For  $D = 1$  h,  $\hat{\mu}_{\text{radar}}$  is 14% lower than  $\hat{\mu}_{\text{gauge}}$ . The main reasons of this smaller value of  $\mu_{\text{radar}}$  are probably attenuation or changes in the vertical profile of reflectivity. The spatial adjustment factor field is constant during the day, while attenuation can be more severe in some hours and areas. The mean-field bias adjustment can partly compensate for this. To some extent the differences in the location parameters can be attributed to an areal reduction effect, which becomes larger for shorter durations. The radar measures the average rainfall depth over an area of  $6 \text{ km}^2$ , while the rain gauge measures precipitation at a point. However, this areal reduction effect might have been partially removed, because the radar data have been adjusted with hourly rainfall data.

Buishand and Wijngaard (2007) estimated  $\mu$  and  $\gamma$  using 84 sliding annual rainfall maxima from the automatic rain gauge at De Bilt for  $D = 5$  to 120 min assuming  $\kappa = -0.09$ . For  $D = 15$  min,  $\hat{\mu}_{\text{radar}}$  and  $\hat{\gamma}_{\text{radar}}$  are respectively 8% and 16% smaller than the estimates by Buishand and Wijngaard (2007), while reductions of respectively 4% and 14% are found for  $D = 60$  min.

Table 4.2 also shows the GEV parameters for  $D = 1$  to 24 h based on a study with 514 annual rainfall maxima observed with 12 automatic rain gauges (Chapter 2). The location parameters are closer to  $\hat{\mu}_{\text{gauge}}$  than to  $\hat{\mu}_{\text{radar}}$ , and for  $D = 1$  h the dispersion coefficient is also closer to  $\hat{\gamma}_{\text{gauge}}$  than to  $\hat{\gamma}_{\text{radar}}$ . The shape parameters are higher, i.e. less negative, in Chapter 2 than  $\hat{\kappa}_{\text{gauge}}$  and  $\hat{\kappa}_{\text{radar}}$  and are in better agreement with  $\hat{\kappa}_{\text{radar}}$ .

## 4.7 Regional estimation and modeling of GEV parameters

### 4.7.1 Estimated GEV parameters for individual durations

In this section, the variation of the GEV parameters with duration is described. The index flood method from Section 4.5.1 is applied, for each individual duration. The estimated location parameters for the individual pixels are averaged to obtain one value of this parameter for each duration. The estimated GEV parameters and their standard deviations are given in Table 4.3. As expected  $\mu$  rises with increasing  $D$ . The parameter  $\gamma$  increases with decreasing duration. For  $D = 15$  and 30 min,  $\kappa$  is less negative than for longer durations.

For longer durations, the standard deviation of  $\hat{\gamma}$  becomes larger with increasing  $D$ , while  $\hat{\gamma}$  becomes smaller. This is caused by the spatial correlation between annual maxima, which becomes larger for increasing  $D$  and results in a smaller effective size of the radar data set. For the same reason, the standard deviation of  $\hat{\kappa}$  increases with  $D$ . For the location parameter the standard deviation becomes also larger for longer durations, however, the relatively largest values are obtained for  $D = 60$  and 120 min. The effect of the increasing spatial

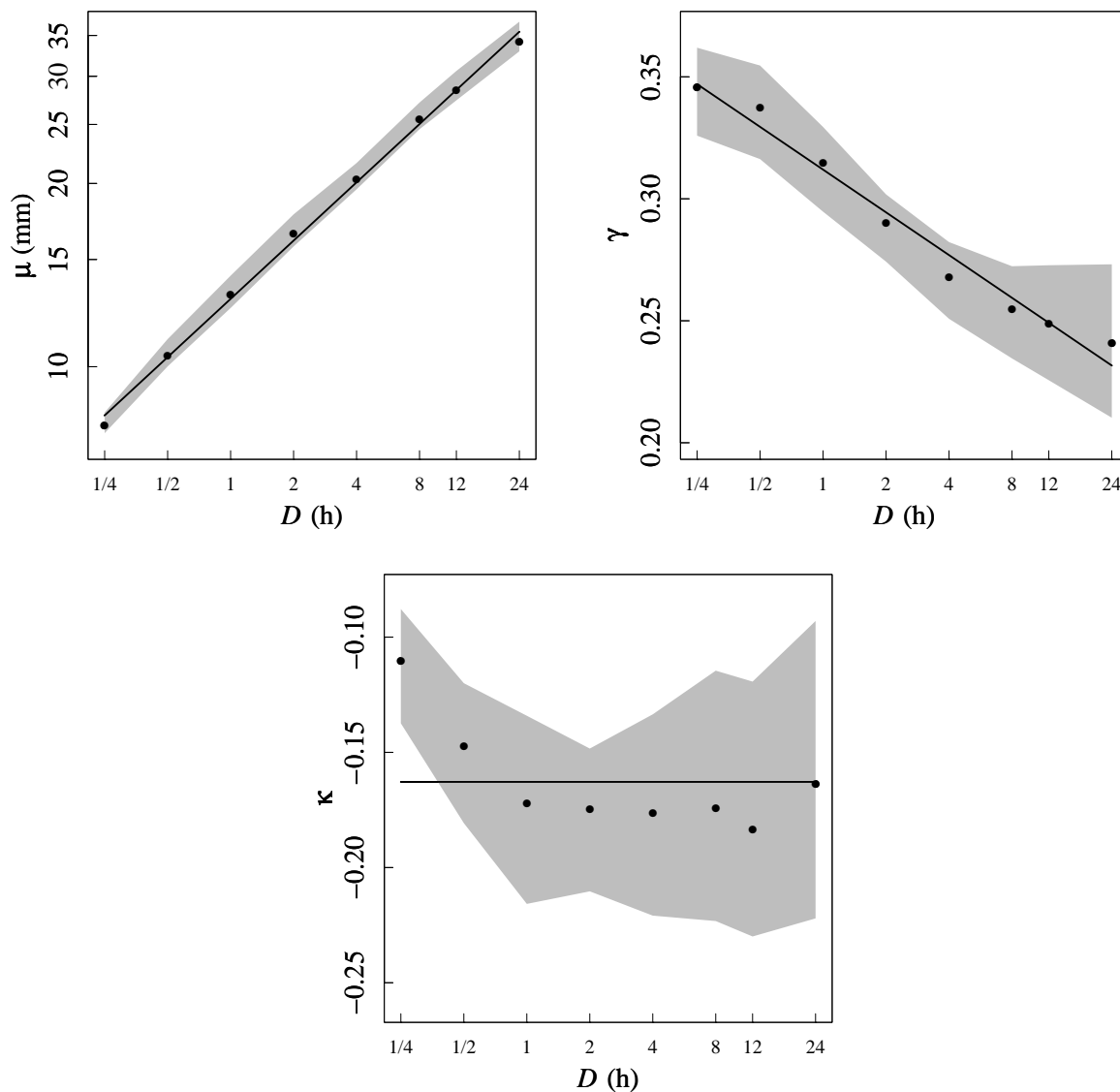


**Figure 4.10:** GEV parameters plotted against duration  $D$  (logarithmic scale). The solid lines represent the ordinary least squares fits to the estimated GEV parameters. The gray-shaded area represents a pointwise 95%-confidence region for the GEV parameter based on the bootstrap.

correlation with increasing duration on the relative standard deviation of this parameter is counterbalanced by the influence of  $\gamma$  on the relative standard deviation.

For  $D = 24$  h, 13% of the annual rainfall maxima in the year 1998 are larger than 75 mm. This is substantially more than the average value of 3%. The sensitivity of the GEV parameters to the influence of the extreme year 1998 is investigated by re-estimating the GEV parameters and their standard deviations using the annual maxima from 1999–2008, instead

of 1998-2008. It was found that  $\hat{\kappa}$  increases from -0.164 to -0.133 for  $D = 24$  h, while  $\hat{\mu}$  and  $\hat{\gamma}$  decrease only slightly with respectively 2% and 4%. The standard deviation of  $\hat{\mu}$  decreases substantially from 1.01 mm (1998-2008) to 0.80 mm (1999-2008) for  $D = 24$  h.

#### 4.7.2 GEV parameters as a function of duration

GEV parameters are modeled as a function of duration to construct rainfall depth-duration-frequency (DDF) curves. Figure 4.10 displays the GEV parameters for  $D = 15$  min to 24 h and reveals that  $\ln \mu$  and  $\gamma$  have a linear relationship with  $\ln D$  ( $D$  in h). Table 4.4 gives the ordinary least squares estimates of the regression coefficients  $a$  and  $b$  in the model

$$\hat{\theta} = a + b \ln D + e, \quad (4.14)$$

where  $\hat{\theta}$  is the estimated GEV parameter of interest ( $\ln \hat{\mu}$ ,  $\hat{\gamma}$  or  $\hat{\kappa}$ ) and  $e$  is a residual. In Chapter 2 the method of generalized least squares is used, which is in this case not applicable, because the estimated covariance matrices are rather unreliable due to the short time series. The bootstrap samples from Section 4.5.2 are used to obtain 1000 estimated intercepts and slopes for each GEV parameter. Subsequently, the standard deviations of the estimated intercept  $\hat{a}$  and slope  $\hat{b}$  are calculated. These are shown in Table 4.4. For  $\kappa$ , the estimate of the slope differs no more than 1.15 times its standard deviation from zero, so that  $\kappa$  is chosen to be constant. Note from Figure 4.10 that the uncertainty of  $\kappa$  is large.

### 4.8 Construction of DDF curves and modeling their uncertainties

#### 4.8.1 Derivation of DDF curves

The relationships that describe the GEV parameters as a function of duration are substituted into the quantile function of the GEV distribution (Eq. (4.8)) to obtain rainfall DDF curves:

$$\hat{x}(T) = \exp(\hat{a}_\mu + \hat{b}_\mu \ln D) \times \left( 1 + (\hat{a}_\gamma + \hat{b}_\gamma \ln D) \frac{\{1 - [-\ln(1 - T^{-1})]^{\hat{\kappa}}\}}{\hat{\kappa}} \right), \quad (4.15)$$

**Table 4.3:** Estimated GEV parameters for  $D = 15, 30, 60$  and 120 min and 4, 8, 12 and 24 h based on radar data for the Netherlands. Standard deviations are estimated with the bootstrap and given between brackets.

$D$	$\hat{\mu}$ (mm)	$\hat{\gamma}$	$\hat{\kappa}$
15 min	8.02 (0.17)	0.346 (0.009)	-0.110 (0.013)
30 min	10.41 (0.29)	0.337 (0.010)	-0.147 (0.016)
60 min	13.12 (0.42)	0.315 (0.009)	-0.172 (0.021)
120 min	16.54 (0.52)	0.290 (0.007)	-0.175 (0.015)
4 h	20.31 (0.52)	0.268 (0.008)	-0.176 (0.024)
8 h	25.45 (0.68)	0.255 (0.010)	-0.174 (0.028)
12 h	28.48 (0.83)	0.249 (0.012)	-0.184 (0.029)
24 h	34.23 (1.01)	0.241 (0.016)	-0.164 (0.032)

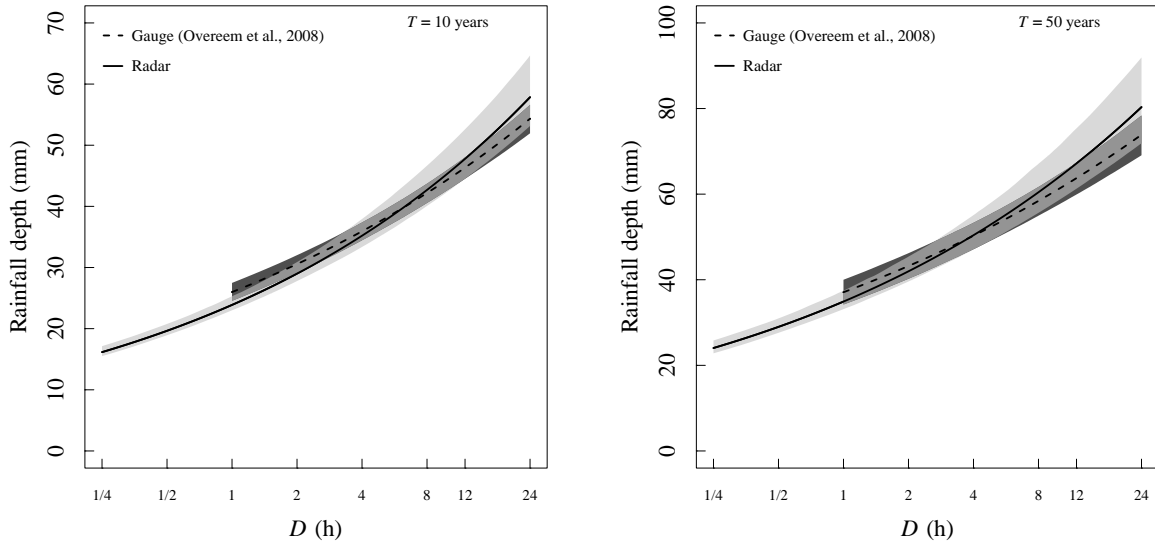


**Figure 4.11:** Rainfall DDF curves for return periods of 10 (left) and 50 (right) years based on rain gauge data (dashed lines, obtained from Chapter 2) and based on radar data (solid lines). Also shown are pointwise 95%-confidence intervals: dark gray for the rain gauge data, light gray for the radar data. The overlap region of these two confidence intervals is shown as gray. Note that  $D$  is plotted on a logarithmic scale.

where  $\hat{a}_\mu = 2.559$ ,  $\hat{b}_\mu = 0.318$ ,  $\hat{a}_\gamma = 0.312$ ,  $\hat{b}_\gamma = -0.025$ ,  $\hat{\kappa} = -0.163$ , and  $D$  is expressed in h. Eq. (4.15) describes the rainfall depth  $x$  (mm) as a function of duration  $D$  for a given return period  $T$ . Figure 4.11 displays the DDF curves for  $T = 10$  and  $T = 50$  years based on radar data from this chapter (solid lines) and those obtained from Chapter 2, using gauge data (dashed lines). As an example, for a return period of 50 years the 60-min radar rainfall depth is 35 mm. For durations shorter than 6.2 h ( $T = 10$  years) and 3.8 h ( $T = 50$  years), gauge rainfall depths are larger than radar rainfall depths. This may be related to remaining errors in the radar data, as was explained in Section 4.6. Note that the rainfall data were obtained from 12 stations in the period 1906-2005 and most data refer to the period 1977-2005, while the radar data span the period 1998-2008.

#### 4.8.2 Modeling uncertainty in DDF curves

It is important to estimate the uncertainty in DDF curves and to take this uncertainty into account in the design of hydraulic structures. The bootstrap is employed to assess the uncertainty in the estimation of the GEV parameters, i.e. sampling errors. The whole fitting procedure of Sections 4.5.1 and 4.7 is applied for each of the 1000 bootstrap samples of annual maxima used earlier. This results in 1000 estimated relationships between GEV parameters and duration, so that 1000 estimated DDF curves are obtained. For each DDF curve the rainfall depths are derived for durations between 15 min and 24 h in steps of 1 min. Next, the 1000 depths are ranked in increasing order for each duration separately and the 25th and

975th values are determined to obtain the 95%-confidence intervals for the rainfall depth quantiles, shown as a light gray-shaded area in Figure 4.11 for return periods of 10 and 50 years. A similar procedure was followed in Chapter 2 to obtain 95%-confidence intervals based on rain gauge data, which are shown in dark gray. The overlap region of the rain gauge- and radar-based confidence intervals is shown in gray.

For the radar data uncertainties become rather large for the longest durations, for example, the 95%-confidence interval ranges from 72 to 92 mm for  $D = 24$  h and  $T = 50$  years, which is due to the relatively small size of the radar data set for calculating the statistics of extreme rainfall. For the gauge data uncertainties are smaller for durations longer than 1.7 h for  $T = 10$  years and 2.2 h for  $T = 50$  years, because they are based on 514 annual maxima with a low spatial correlation. In contrast, for the radar data the uncertainties become small for short durations compared to the gauge data. Because of the low spatial correlation of short-duration rainfall, the large number of observations in space compensates for the small number of observations in time. So, especially for short-duration rainfall, the limited length of the radar data set for deriving the statistics of extreme rainfall becomes less important. Moreover, in Chapter 2 uncertain conversion factors were used to obtain the location parameter and dispersion coefficient for sliding 60-min and 120-min maxima from clock-hour data, which increases the standard deviation of these GEV parameters for the rain gauge data.

The bootstrap is used to estimate the standard deviation of the quantiles for each duration for both radar and gauge data. Since the gauge data consist of 514 almost uncorrelated annual rainfall maxima, the corresponding effective length of the radar data set can be calculated and appears to be 80 to 100 years for  $T = 10$  and 50 years respectively for  $D = 24$  h and increases for shorter durations. Because of the smaller spatial association of more extreme events, the effective length of the data set increases for longer return periods.

### 4.8.3 Local DDF curves

Following the approach described in Sections 4.8.1 and 4.8.2, local DDF curves and their uncertainties are derived. Annual maxima are obtained from two areas, each containing 121 pixels in a square lattice. These two areas A and B are indicated by the white boxes in

**Table 4.4:** Estimates of the regression coefficients  $a$  and  $b$  in Eq. (4.14) and their standard deviations between brackets. The result in the bottom row refers to the case of a constant shape parameter ( $b = 0$ ).

GEV parameter	$\hat{a}$	$\hat{b}$
$\ln \mu$	2.559 (0.025)	0.318 (0.006)
$\gamma$	0.312 (0.006)	-0.025 (0.005)
$\kappa$	-0.153 (0.014)	-0.011 (0.009)
$\kappa$	-0.163 (0.016)	-



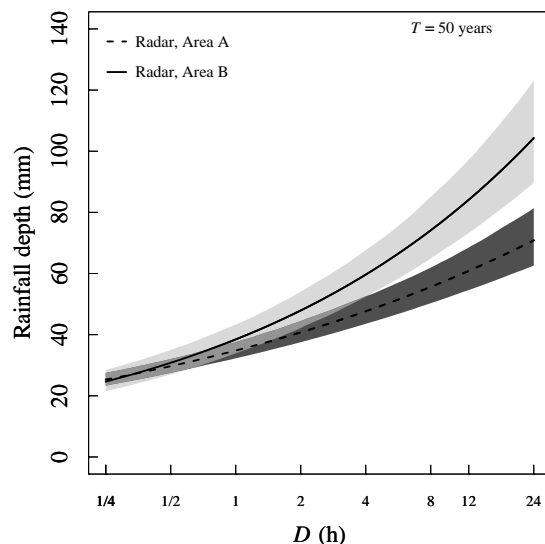


**Figure 4.12:** Local rainfall DDF curves for two areas for a return period of 50 years based on radar data. Also shown are pointwise 95%-confidence intervals: dark gray for area A and light gray for area B and their overlap region shown as gray. Note that  $D$  is plotted on a logarithmic scale. The areas A and B are indicated in Figure 4.9.

Figure 4.9. For  $D = 24$  h, area A is one of the “driest” areas and area B one of the “wettest” areas in the Netherlands. The location parameter  $\mu$  is estimated for each area and duration separately by fitting a GEV distribution to 1331 annual maxima with  $\gamma$  and  $\kappa$  set equal to the estimated values in Table 4.3. Next, the regression coefficients  $a$  and  $b$  for this GEV parameter are estimated for each area. Eq. (4.15) is utilized to construct local DDF curves for  $T = 50$  years, which are shown in Figure 4.12 together with their 95%-confidence intervals. For durations longer than 4.1 hours, the 95%-confidence intervals of area A and B do not overlap implying that the DDF curves from those two areas differ significantly. In general, the 95%-confidence intervals are wider than those for the average DDF curve for the Netherlands, shown in Figure 4.11, due to the larger uncertainty of the location parameter.

## 4.9 Discussion and conclusions

Based on radar data an extreme rainfall climatology for the Netherlands was derived. Two adjustment methods, which use rain gauge data, were combined to obtain a high-quality radar rainfall data set suitable for hydrological and climatological applications (Chapter 3). From the adjusted radar data, annual rainfall maxima were abstracted for durations of 15 min to 24 h. The date and timing of annual rainfall maxima were studied. The index flood method was applied by fitting GEV distributions with constant shape parameter and dispersion coefficient to these annual maxima using maximum likelihood. It was shown that regional variability in the GEV location parameter in the Netherlands is statistically significant for most durations. Estimated GEV parameters based on radar and rain gauge data

were compared. Subsequently, radar-based rainfall depth-duration-frequency (DDF) curves and their uncertainties were derived.

This is one of the few studies which has been devoted to the derivation of extreme rainfall statistics based on radar data. For this purpose, one of the longest radar data sets described in the literature was used. To the authors' knowledge this study is the first which shows that radar data are suitable to derive rainfall DDF curves if a regional frequency analysis is applied. Nevertheless, the length of the time series of annual maxima is relatively short for estimating the GEV parameters for long durations, such as  $D = 24$  h.

Madsen et al. (2002) estimated regional rainfall intensity-duration-frequency curves in Denmark using the partial duration series method. Threshold exceedances were modelled with the generalized Pareto distribution with a constant shape parameter across the country. This parameter was estimated from the regional average coefficient of L variation (L-CV). The choice of the partial duration series method was based on earlier Monte Carlo studies (Madsen et al., 1997a,b) showing that in the case of a negative shape parameter this method generally provides better estimates than fitting a GEV distribution to the annual maxima using L-moments. Spatial dependence was not considered in these Monte Carlo studies. A change in the degree of spatial association with event magnitude may, however, strongly influence the choice between annual maxima and the partial duration series. Moreover, the estimates of large quantiles of the annual maximum distribution might be sensitive to the choice of the threshold. Despite the small number of years in the case of radar-based rainfall data, the gain of using the partial duration series method is not clear.

The comparison of GEV parameters based on radar and rain gauge data from the same locations shows that these are in reasonable agreement. However, especially for short durations, the estimated location parameters differ from those obtained from gauge data. This can be attributed largely to remaining errors in the radar data, such as attenuation or changes in the vertical profile of reflectivity. The combination of a daily spatial adjustment and an hourly mean-field bias adjustment is probably not sufficient to remove these errors completely on subdaily timescales.

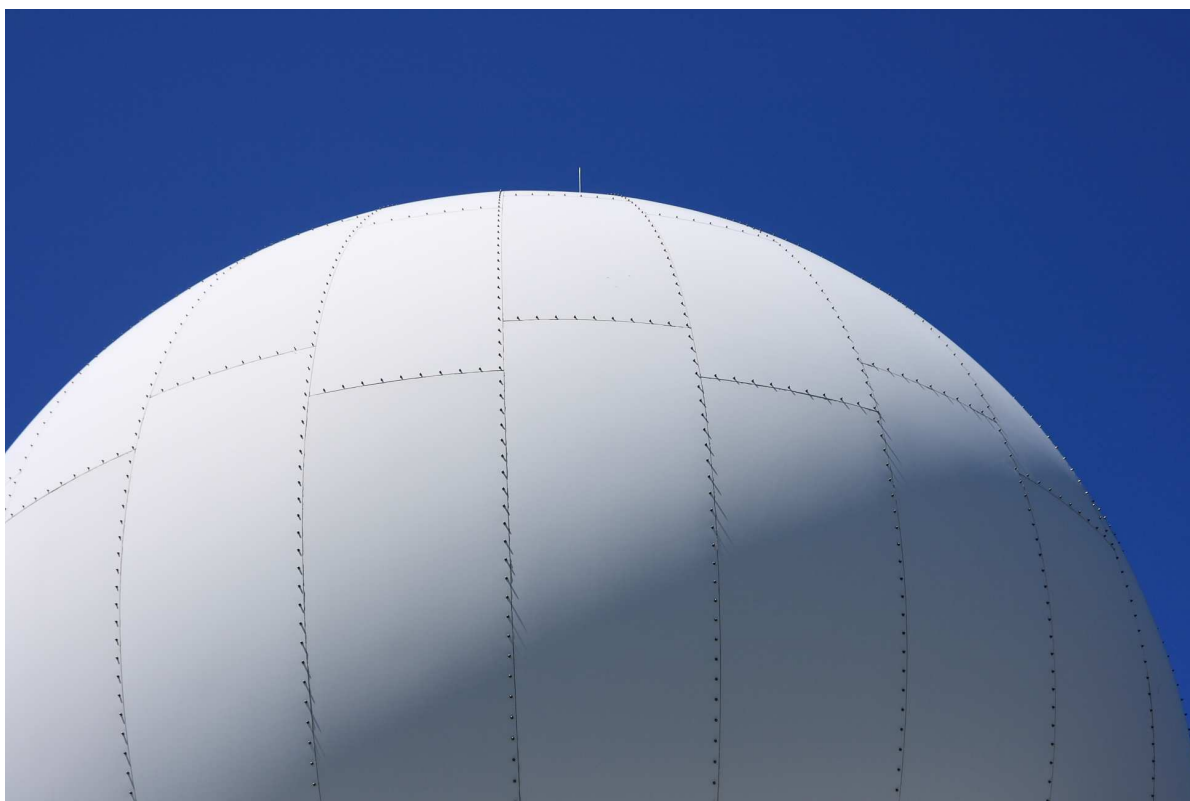
The radar-based rainfall DDF curves contain quantiles of extreme rainfall averaged over the Netherlands, while it has been shown that regional differences in the GEV location parameter exist for most durations. However, if DDF curves are derived for small areas, the uncertainties in the DDF curves generally become larger compared to the uncertainties of the average DDF curve for the Netherlands. This is due to the small number of annual maxima.

For long durations uncertainties in radar-based DDF curves become rather large because of the short period of 11 years and the high spatial correlation between annual maxima at these timescales. Nevertheless, for short-duration rainfall uncertainties are small, because the spatial correlation of these events is much lower. It appeared that, for  $D = 24$  h, the

shape parameter of the GEV distribution changes considerably if a year with extreme rainfall events was left out of the analysis. This implies that 11-year records of radar rainfall are useful, but still quite short to obtain reliable statistics of extreme rainfall for long return periods and long durations. However, the length of the radar data set is less important for short-duration rainfall. And especially at those short timescales the contribution of radar in deriving extreme rainfall statistics is most interesting.

### **Acknowledgements**

We thank Remko Uijlenhoet (Hydrology and Quantitative Water Management Group, Wageningen University) for discussion, the three anonymous reviewers for their comments, and Rudolf van Westrhenen (KNMI) for archiving more than five years of radar data in the period 1998-2003.





## Chapter 5

---

# Extreme-value modeling of areal rainfall from weather radar<sup>1</sup>

### Abstract

An 11-year high-quality radar rainfall data set is used to abstract annual maximum rainfall depths for durations of 15 min to 24 h and area sizes of 6 to  $1.7 \times 10^3 \text{ km}^2$  for the Netherlands ( $\approx 3.55 \times 10^4 \text{ km}^2$ ). Generalized Extreme Value (GEV) distributions are fitted to the annual maxima and a new method is presented to model GEV parameters as a function of duration and area size. This leads to a semi-empirical expression from which quantiles of extreme rainfall depths can be obtained for a chosen duration, area size and return period. The uncertainties in these quantiles are calculated using the bootstrap method. Radar-based areal reduction factors (ARFs) are derived. These ARFs are comparable to those based on high-density rain gauge networks derived from the literature. It is concluded that radar data, after careful quality control, are suitable to estimate extreme areal rainfall depths.

---

<sup>1</sup>*Water Resources Research*, 2009, submitted, by Aart Overeem, Adri Buishand, Iwan Holleman and Remko Uijlenhoet.

## 5.1 Introduction

Extreme-value modeling of areal rainfall is of importance for the design of hydraulic structures and verification of weather and climate models. Extreme areal rainfall depths, for instance over catchment areas, are usually obtained by spatial interpolation of rain gauge data. A reliable estimation of these depths is often hampered by the low spatial density of rain gauge networks, particularly for short durations. Weather radars provide quantitative precipitation estimates with a high spatial and temporal resolution, however, these estimates need adjustment due to gross errors.

Few studies have been devoted to the statistics of extreme areal rainfall depths obtained from weather radar. Frederick et al. (1977) were probably the first to derive rainfall depth-area relations from radar data. The increased quality of quantitative precipitation estimates from radar and the long time series that have become available has led to a renewed interest for this kind of research in recent years, for instance, Durrans et al. (2002), Allen and DeGaetano (2005b) and Lombardo et al. (2006). A particular quantity of interest is the areal reduction factor (ARF), which converts percentiles of point rainfall to percentiles of areal rainfall. ARFs have usually been calculated employing data from rain gauge networks (U.S. Weather Bureau, 1964; NERC, 1975; Bell, 1976).

In this chapter 11 years (1998-2008) of annual radar rainfall maxima are analyzed for durations  $D$  of 15 min to 24 h and area sizes of 6 km<sup>2</sup> (one radar pixel) to  $1.7 \times 10^3$  km<sup>2</sup> (289 radar pixels) for the Netherlands. The radar rainfall data have been adjusted using rain gauges.

In Chapter 2 GEV distributions are fitted to annual rainfall maxima obtained from rain gauges and the GEV parameters are modeled as a function of duration for  $D = 1$  to 24 h. In the subsequent chapter, it is shown that these relationships are also applicable to model the estimated GEV parameters from the adjusted radar rainfall at a radar pixel for  $D = 15$  min to 24 h. We find that the radar data set is suitable to derive rainfall depth-duration-frequency (DDF) curves, which describe the rainfall depth as a function of duration for given return periods.

The estimation of extreme *areal* rainfall depths employing the GEV distribution has hardly ever been pursued so far. This chapter presents a new approach to obtain quantiles of extreme areal rainfall depths by modeling GEV parameters as a function of duration as well as area size. Besides, the GEV parameters are estimated using a high-quality radar rainfall data set, one of the longest described in the literature. The bootstrap method (Diaconis and Efron, 1983; Efron and Tibshirani, 1993) is applied to estimate the uncertainty in GEV-parameter-duration-area relationships. These relationships are employed to derive areal DDF curves. From the estimated quantiles of rainfall depths, areal reduction factors are calculated

In Section 5.2 the radar data set is described. Section 5.3 describes the methodology to fit a GEV distribution to annual radar rainfall maxima. In Section 5.4 GEV parameters are modeled as a function of duration and area size. These models are used to derive areal DDF

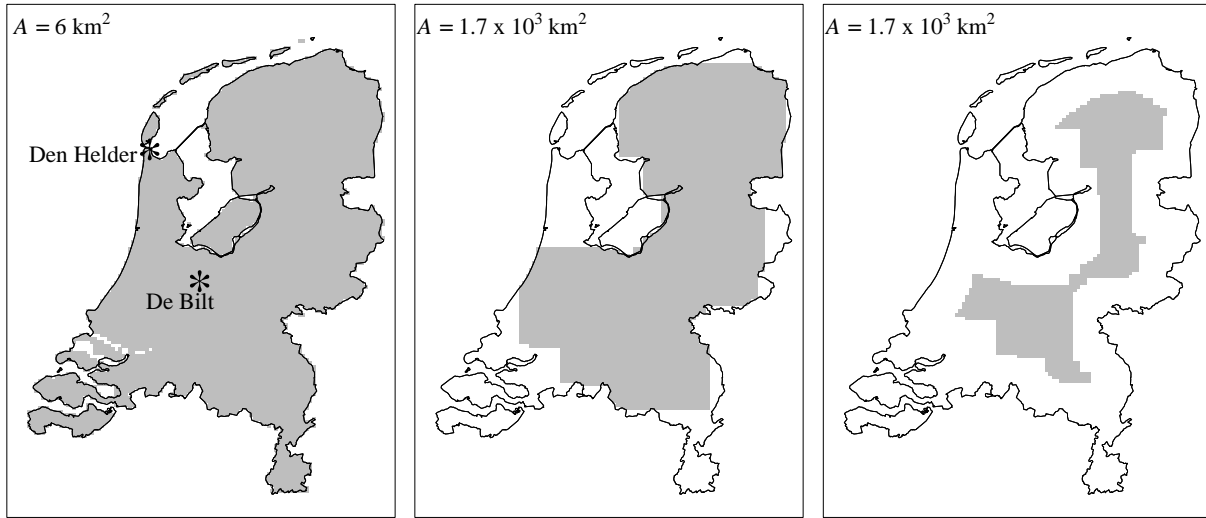


**Figure 5.1:** Domain size employed to calculate annual rainfall maxima for  $A = 6 \text{ km}^2$  (left) and  $1.7 \times 10^3 \text{ km}^2$  (middle). The right figure displays the pixels to which annual maxima are assigned to for  $A = 1.7 \times 10^3 \text{ km}^2$ . The locations of the weather radars are indicated in the left panel.

curves and their uncertainties in Section 5.5. Radar-based areal reduction factors are derived in Section 5.6. Finally, a discussion and conclusions are given.

## 5.2 Radar data

KNMI operates two C-band Doppler weather radars, from which horizontal cross sections of radar reflectivity factor at constant altitude were obtained (pseudo CAPPI images) with a 2.4-km spatial resolution and a 5-min temporal resolution. The radars are located in the Netherlands in De Bilt ( $52.10^\circ \text{ N}$ ,  $5.18^\circ \text{ E}$ , 44 m above mean sea level) and Den Helder ( $52.96^\circ \text{ N}$ ,  $4.79^\circ \text{ E}$ , 51 m above mean sea level), see Figure 5.1. After ground clutter removal (Holleman and Beekhuis, 2005), the influence of remaining strong residual clutter and hail was limited by setting reflectivities above 55 dBZ to 55 dBZ ( $\approx 100 \text{ mm h}^{-1}$ ). Next, reflectivity factors  $Z$  ( $\text{mm}^6 \text{ m}^{-3}$ ) were converted to rainfall intensities  $R$  ( $\text{mm h}^{-1}$ ) with a fixed  $Z$ - $R$  relationship (Marshall et al., 1955),

$$Z = 200R^{1.6}, \quad (5.1)$$

resulting in 97 levels of rainfall intensities ranging from 0.1 to  $100 \text{ mm h}^{-1}$ , from which 5-min rainfall data and 1-h rainfall depths were derived if at least 10 images were available in the corresponding clock-hour. A five-pixel median filter on nearest-neighbor pixels was applied to the depths to remove local outliers caused by accumulated residual ground clutter. Accumulation data from both radars were combined into one composite using a weighting factor as a function of range from the radar. The data set of composites covers the entire land surface of the Netherlands ( $\approx 3.55 \times 10^4 \text{ km}^2$ ) for the period 1998-2008, with a data availability of approximately 82%.

Quantitative precipitation estimation with radar is hampered by, for example, overshooting of precipitation, variability of the drop-size distribution and attenuation in the case of strong precipitation or a wet radome (Joss and Waldvogel, 1990; Doviak and Zrnić, 1993). Volumetric data have been used to improve the quality of radar rainfall depths, for instance, by performing a vertical profile of reflectivity correction (Vignal and Krajewski, 2001; Germann and Joss, 2002) or an attenuation correction (Nicol and Austin, 2003). Since such data were not available, rain gauge networks were utilized to adjust the radar-based accumulations: an automatic network with 1-h rainfall depths for each clock-hour ( $\approx 1$  station per  $1000 \text{ km}^2$ ) and a manual network with 24-h 08-08 UTC rainfall depths ( $\approx 1$  station per  $100 \text{ km}^2$ ). A daily spatial adjustment was combined with an hourly mean-field bias adjustment. The 1-h rainfall depths were employed to construct 4-, 8-, 12- and 24-h depths for each clock-hour. From the 5-min composites of rainfall data, depths for durations of 15, 30, 60 and 120 min were obtained for each 5 min. Chapters 2 and 3 give a more elaborate description of the radar and rain gauge data set and the employed adjustment methods.

## 5.3 Extreme-value modeling of areal rainfall

### 5.3.1 Abstracting annual maxima

The radar data set consists of 6190 pixels of approximately  $6 \text{ km}^2$  each, which cover the entire land surface of the Netherlands. Running annual maxima are abstracted for 8 durations  $D$  of 15, 30, 60 and 120 min and 4, 8, 12 and 24 h and 9 different area sizes  $A$  for the 11-year period (72 different combinations of  $D$  and  $A$ ). The term running is employed here to indicate that the annual maxima are selected from the  $D$ -h or  $D$ -min depths for each clock-hour of the year, for  $D = 4$  to 24 h, or each 5 min of the year, for  $D = 15$  to 120 min. Annual areal rainfall maxima are selected for square lattices of 1, 3, ..., 17 pixel(s) a side, which correspond to areas of 6 to  $1.7 \times 10^3 \text{ km}^2$  and are only available if each pixel in the square lattice is above the land surface of the Netherlands. For increasing  $A$  this results in a decline of the number of square lattices and therefore a decrease in the domain size used in the calculation of annual maxima from  $3.55 \times 10^4 \text{ km}^2$  for  $A = 6 \text{ km}^2$  to  $2.55 \times 10^4 \text{ km}^2$  for  $A = 1.7 \times 10^3 \text{ km}^2$ , see Figure 5.1.

The distribution of annual maxima over the months was studied. For  $A = 1.7 \times 10^3 \text{ km}^2$ , approximately 86% of the annual 15-min rainfall maxima were observed in the period June to September, which is only slightly lower than the percentage found for  $A = 6 \text{ km}^2$  (Chapter 4).

### 5.3.2 Fitting a GEV distribution

The GEV distribution is often employed to describe the distribution of annual maximum rainfall. This distribution represents the three extreme value types (Fréchet, Gumbel and Weibull) in a single equation. The type is determined by the shape parameter of the distri-



bution. The GEV cumulative distribution function  $F(x)$  is given by (Jenkinson, 1955):

$$F(x) = \begin{cases} \exp\{-[1 - \frac{\kappa}{\alpha}(x - \mu)]^{1/\kappa}\} & \text{for } \kappa \neq 0, \\ \exp\{-\exp[-\frac{1}{\alpha}(x - \mu)]\} & \text{for } \kappa = 0, \end{cases} \quad (5.2)$$

with  $\mu$  the location,  $\alpha$  the scale and  $\kappa$  the shape parameter of the distribution. The quantile function, the inverse of Eq. (5.2), is given by:

$$x(T) = \begin{cases} \mu + \frac{\alpha\{1 - [-\ln(1 - T^{-1})]^\kappa\}}{\kappa} & \text{for } \kappa \neq 0, \\ \mu - \alpha \ln[-\ln(1 - T^{-1})] & \text{for } \kappa = 0, \end{cases} \quad (5.3)$$

where  $T = 1/(1 - F)$  is the return period.

Quantile estimators would be very inaccurate if they would be obtained from a GEV distribution fitted to the 11 annual maxima from a single radar pixel. This can be overcome by applying a regional frequency analysis, in which certain distribution parameters are assumed to be constant over a region. In Chapter 4 the index flood method is employed using a constant shape parameter and dispersion coefficient  $\gamma = \alpha/\mu$  over the Netherlands while estimating the location parameter for single radar pixels. They show that regional differences in the location parameter are significant for most durations. Nevertheless, because only 11 years of data have been used, there can be large spatial differences in the estimated location parameter due to randomness. In Chapter 4 it was found that uncertainties in the estimated quantiles for individual pixels become rather large if the index flood method is applied to the radar data. These can be reduced by averaging the estimated location parameters from each pixel over a region. In this chapter, the three GEV parameters are taken to be constant over the whole Netherlands for each  $D$  and  $A$  implying that regional variability in extreme areal rainfall statistics is neglected. The estimated location parameters for  $A = 6 \text{ km}^2$  are 1.2-1.8% smaller than the country-wide average values of this parameter for the various durations in Chapter 4, which is partly due to a positive bias in the latter.

Estimation of these GEV parameters is based on a likelihood function, constructed under the assumption that the maxima at different radar pixels are independent (Buishand, 1991; Northrop, 2004). This likelihood function is given by:

$$L(\mu, \gamma, \kappa) = \sum_{s=1}^S L_s(\mu, \gamma, \kappa), \quad (5.4)$$

where  $L_s$  is the log-likelihood for the annual maxima for a given duration  $D$  in region  $s$  of size  $A$ , and  $S$  is the number of regions of this size, which varies from 1477 ( $A = 1.7 \times 10^3 \text{ km}^2$ ) to 6190 ( $A = 6 \text{ km}^2$ ). Maximizing  $L(\mu, \gamma, \kappa)$  with respect to  $\mu$ ,  $\gamma$  and  $\kappa$  gives the maximum likelihood estimates  $\hat{\mu}$ ,  $\hat{\gamma}$  and  $\hat{\kappa}$ . An implementation of the Nelder-Mead optimization algorithm was used for this purpose. Though spatially correlated annual maxima will hardly lead to a bias in the estimated GEV parameters, their variance will increase

with respect to the case of uncorrelated annual maxima. However, a small simulation study in Chapter 4 indicates that the maximum likelihood estimates have smaller variances than those based on the method of L-moments under the index flood assumption. This also applies to the situation where regional variation in the location parameter is neglected.

As was pointed out in Section 5.3.1, an increase in area size leads to a decrease in the domain size used in the calculation of annual maxima. To investigate the resulting effect, annual maxima were selected for the domain size shown in Figure 5.1 (middle panel), which belongs to  $A = 1.7 \times 10^3 \text{ km}^2$ , for each area size. Next, these maxima were used to estimate the GEV parameters for  $A = 6 \text{ km}^2$ . It appears that the values of the location parameter and the dispersion coefficient differ less than respectively 1.1% and 3.9% from those obtained earlier, implying that the influence of the decreasing domain size with increasing area size is small.

It is important to verify whether the GEV distribution is suitable to model areal radar rainfall maxima. The Anderson-Darling statistic is employed to test the goodness of fit following the same procedure as described in Ahmad et al. (1988). The test statistic is given by (Anderson and Darling, 1952):

$$\int_{-\infty}^{+\infty} [F_n(x) - F(x)]^2 \varphi(x) dF(x), \quad (5.5)$$

where  $F(x)$  is the GEV cumulative distribution function,  $F_n(x)$  is the empirical distribution function, and  $\varphi(x)$  is a weight function. In the original Anderson-Darling test  $\varphi(x) = [F(x)(1 - F(x))]^{-1}$  and in the modified Anderson-Darling test  $\varphi(x) = [1 - F(x)]^{-1}$ . In the latter large weight is given to departures in the right tail of the distribution. A GEV distribution is fitted to the annual maxima and the Anderson-Darling statistic is calculated for each region separately. The percentage of regions for which the null hypothesis of an adequate fit of the GEV distribution is not rejected at the 5% level is given in Table 5.1 for six combinations of  $D$  and  $A$ . This percentage is at least 95, indicating that the GEV distribution fits well.

**Table 5.1:** Results of testing the goodness of fit of the GEV distribution using Anderson-Darling statistics for six combinations of  $D$  and  $A$ . For each combination the percentage of the regions is given for which the null hypothesis is not rejected at the 5% level.

$D$	$A$	Percentage of regions (Anderson-Darling)	Percentage of regions (modified Anderson-Darling)
15 min	$6 \text{ km}^2$	97.4	97.2
15 min	$2.8 \times 10^2 \text{ km}^2$	97.7	97.7
15 min	$1.7 \times 10^3 \text{ km}^2$	99.2	98.6
24 h	$6 \text{ km}^2$	96.2	97.0
24 h	$2.8 \times 10^2 \text{ km}^2$	96.5	98.3
24 h	$1.7 \times 10^3 \text{ km}^2$	95.1	98.4

### 5.3.3 Bootstrap samples

Because the annual maxima are spatially correlated, it is not appropriate to apply the usual methods for deriving standard errors and confidence intervals from the likelihood function. The bootstrap is a technique that can account for spatial correlation by resampling year numbers with replacement (Diaconis and Efron, 1983; GREHYS, 1996; Faulkner and Jones, 1999). Bootstrap samples are created as follows in this chapter:

- Draw a random sample of 11 year numbers with replacement from the series of year numbers 1998, ..., 2008.
- Select the annual areal rainfall maxima for the  $S$  regions above the land surface of the Netherlands for the sampled year numbers for each combination of  $D$  and  $A$ . This leads to one bootstrap sample of 11 years of annual maxima for 72 combinations of  $D$  and  $A$ .
- Repeat this 1000 times.

Each time that the bootstrap is used to calculate, for example, 95%-confidence bands for the rainfall depth-duration-frequency curves, the same 1000 bootstrap samples are employed.

## 5.4 GEV parameters as a function of duration and area size

In this section, GEV parameters are modeled as a function of both duration and area size resulting in GEV-parameter-duration-area relationships. Thus, each GEV parameter is modeled as a function of  $D$  and  $A$  for  $D = 15$  min to 24 h and  $A = 6$  to  $1.7 \times 10^3$  km<sup>2</sup> using 72 estimates. Similar relationships are employed as in Chapters 2 and 4 for the terms in the equation where  $A$  is not involved. In Chapter 2 a 514-year record of annual rainfall maxima is used, obtained from 12 automatic rain gauges, to estimate GEV parameters for  $D = 1$  to 24 h, and in Chapter 4 GEV distributions are fitted to annual rainfall maxima at a radar pixel for  $D = 15$  min to 24 h.

The following three semi-empirical models give a reasonable fit to the estimated GEV parameters:

$$\mu(D, A) = a_1 D^{a_2} + b_1 A^c + b_2 A^c \ln D, \quad (5.6)$$

$$\gamma(D, A) = a_1 + a_2 \ln D + b_1 \ln A + b_2 D \ln A, \quad (5.7)$$

$$\kappa(D, A) = a_1 + b_1 \ln A + b_2 \ln D \ln A, \quad (5.8)$$

where  $D$  is expressed in h and  $A$  in km<sup>2</sup>. Table 5.2 gives the nonlinear least squares estimates of the regression coefficients  $a_1$ ,  $a_2$ ,  $b_1$ ,  $b_2$  and  $c$  and their standard deviations obtained from the bootstrap. The last column of the table gives the mean square of the standardized residuals:

$$MS = \frac{1}{K - p} \sum_{k=1}^K \frac{e_k^2}{\hat{\sigma}_k^2}, \quad (5.9)$$

with  $e_k$  the difference between the estimated GEV parameter and the value from the semi-empirical model for the  $k$ th combination of  $D$  and  $A$ ,  $\hat{\sigma}_k$  the standard deviation of the estimated GEV parameter obtained from the bootstrap,  $K$  the number of duration-area combinations ( $K = 72$ ) and  $p$  the number of estimated regression coefficients. This statistic should be about 1 in the case of an adequate fit. Large values indicate lack of fit and small values overfitting.

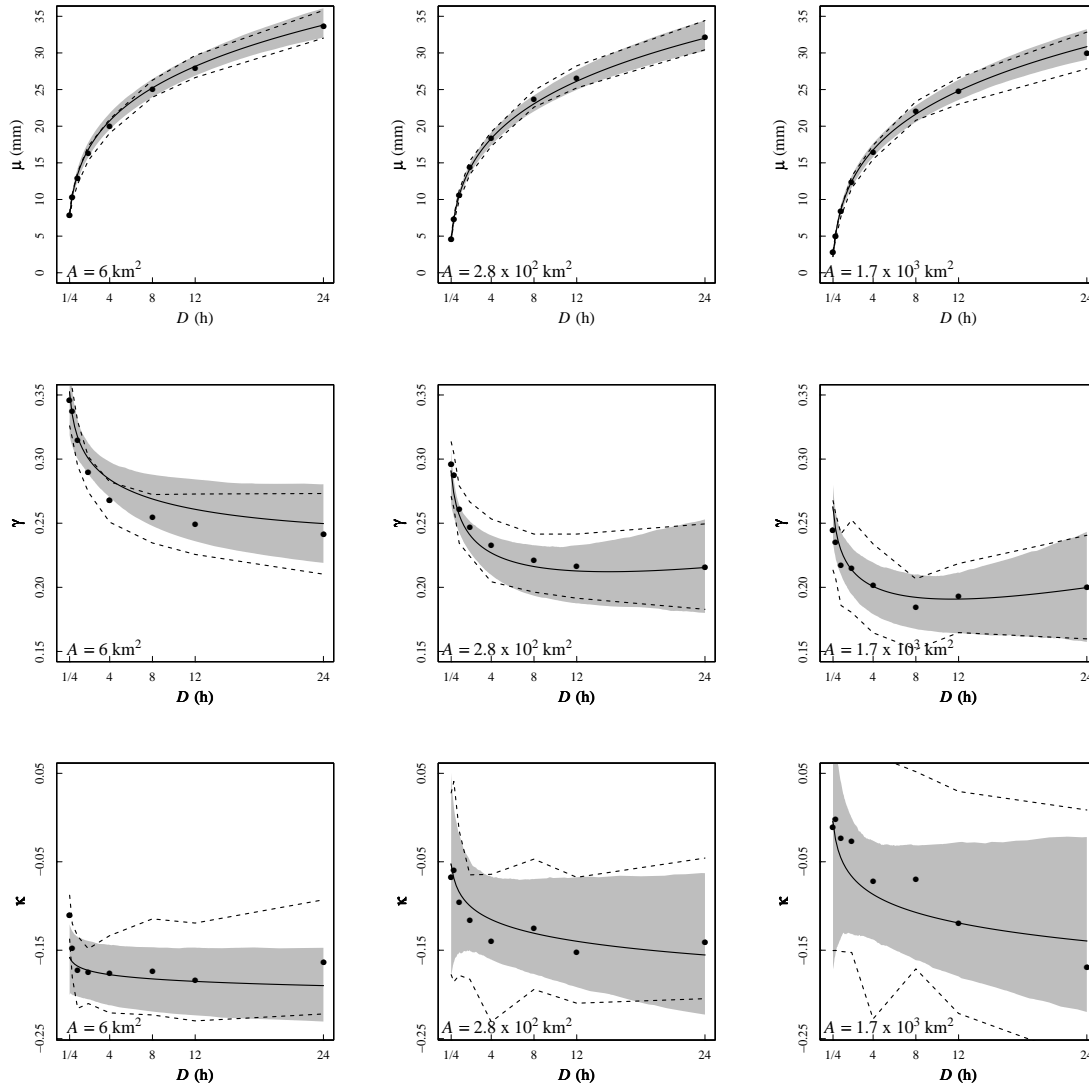
In general, the values of the estimated regression coefficients are relatively large compared to their standard deviations. However, the standard deviations become rather large for the estimated regression coefficients  $\hat{b}_1$  in the model for  $\mu$ , and  $\hat{b}_2$  in the models for  $\gamma$  and  $\kappa$ . This and the relatively low values of MS point to some overfitting. The correlation coefficients between the estimated regression coefficients were also estimated from the bootstrap samples. This revealed a large negative correlation between the estimates  $\hat{b}_1$  and  $\hat{b}_2$  as well as a large positive or negative correlation for the other estimated coefficients in the model for  $\mu$ . Therefore, these models may not be appropriate for  $D$ s and  $A$ s outside the range of used durations and area sizes. If the term  $b_1 A^c$  is removed from Eq. (5.6), MS increases to 37.8 for  $\mu$  implying that the reduced model is not appropriate. For  $\gamma$  and  $\kappa$  MS rises to respectively 0.83 and 1.05 if the interaction term in Eqs. (5.7) and (5.8) is deleted.

Figure 5.2 shows the estimated GEV parameters and the obtained fits as a function of duration for  $A = 6 \text{ km}^2$ ,  $2.8 \times 10^2 \text{ km}^2$  and  $1.7 \times 10^3 \text{ km}^2$ . The parameter  $\mu$  increases and  $\kappa$  decreases with increasing  $D$ . For the latter, however, the change is small if  $A = 6 \text{ km}^2$ . With the exception of a slight increase at long durations when  $A$  becomes large, the parameter  $\gamma$  declines for increasing  $D$ . For the same duration,  $\mu$  and  $\gamma$  decrease with increasing  $A$  due to an areal reduction effect. This effect is stronger at short durations. The relatively weak areal reduction effect at long durations explains the nonmonotonous change of  $\gamma$  with duration for large  $A$ , which is not reproduced by the reduced model for  $\gamma$ .

The shape parameter  $\kappa$  becomes less negative for increasing  $A$  and even approaches zero for short durations. By contrast,  $\kappa$  should be constant in the case of a max-stable process (Coles and Tawn, 1996). Max-stable processes have been used in the statistical literature to describe extreme areal rainfall (Coles, 1993; Coles and Tawn, 1996; Buishand et al., 2008). The observed change of  $\kappa$  in Figure 5.2 implies that the extreme upper tail becomes shorter in the case of area-average rainfall. This may be attributed to the nature of spatial dependence

**Table 5.2:** Estimates of the regression coefficients in Eqs. (5.6) - (5.8), their standard deviations (between brackets), and the mean square of the standardized residuals (MS).

GEV p.	$\hat{a}_1$	$\hat{a}_2$	$\hat{b}_1$	$\hat{b}_2$	$\hat{c}$	MS
$\mu$ (mm)	17.92 (2.82)	0.225 (0.034)	-3.57 (2.39)	0.43 (0.205)	0.128 (0.044)	0.74
$\gamma$	0.344 (0.012)	-0.025 (0.007)	-0.016 (0.003)	0.0003 (0.0002)	-	0.51
$\kappa$	-0.206 (0.018)	-	0.022 (0.006)	-0.004 (0.003)	-	0.39



**Figure 5.2:** GEV parameters plotted against duration  $D$  for different area sizes  $A$ . The solid lines represent the nonlinear least squares fits to the estimated GEV parameters. The gray-shaded areas represent point-wise 95%-confidence intervals for the modeled GEV parameters based on the data for the 72 considered combinations of duration and area size. The dashed lines mark 95%-confidence bands for the GEV parameters based on the data for the given duration and area size only.

of precipitation. For a region in south-west England, Ancona-Navarrete and Tawn (2002) demonstrate that the daily precipitation amounts  $X$  and  $Y$  from two locations separated by 5 km or more are asymptotically independent, i.e.  $\lim_{u \rightarrow \infty} \Pr(Y > u | X > u) = 0$ . Thus the probability that  $Y$  is extreme given that  $X$  is extreme tends to zero, or it is unlikely that the extreme values of  $X$  and  $Y$  occur together. The area-average will therefore be considerably

reduced with respect to the highest point rainfall amounts in extreme situations. This leads to a relatively short upper tail of the annual maximum distribution of area-average rainfall. For the reduced model in which the interaction term in Eq. (5.8) is deleted, the estimates of  $\kappa$  range from -0.175 for  $A = 6 \text{ km}^2$  to -0.075 for  $A = 1.7 \times 10^3 \text{ km}^2$ . In particular for large area sizes, the  $\kappa$ s from this model deviate considerably from the estimated  $\kappa$ s for  $D = 0.25, 0.5$  (up to 0.07 for  $A = 1.7 \times 10^3 \text{ km}^2$ ) and 24 h (down to -0.09 for  $A = 1.7 \times 10^3 \text{ km}^2$ ).

The regression coefficients were also estimated using weighted least squares with the inverse of the variances of the estimated GEV parameters as weights. The influence on the values of the estimated regression coefficients is, however, small.

A thousand bootstrap estimates of the GEV-parameter-duration-area relationships (Eqs. (5.6) - (5.8)) were obtained from which 1000 values of each GEV parameter were calculated with a time step of 1 min. These were ranked in increasing order and the 25th and 975th values were determined to plot 95%-confidence intervals for the modeled GEV parameters as gray-shaded areas in Figure 5.2. The dashed lines in that figure connect the 95%-confidence intervals for the GEV parameter based on the data for the given duration and area size only, using the same bootstrap samples. For  $\kappa$  the area between these dashed lines is larger than the gray-shaded area, indicating that modeling this GEV parameter as a function of  $D$  and  $A$  reduces the uncertainty.

The confidence intervals for  $\kappa$  are relatively narrow for  $A = 6 \text{ km}^2$  and wide for larger area sizes. This can mainly be attributed to the increase of spatial correlation between the area-average rainfalls resulting from the overlap of areas if  $A > 6 \text{ km}^2$ . For the parameters  $\mu$  and  $\gamma$ , the width of the confidence intervals depends much less on the area size. For the confidence intervals for  $\gamma$ , the effect of increased spatial correlation with area size is counterbalanced by the decrease of this parameter with area size, and for the confidence intervals for  $\mu$ , it is the decrease of the GEV scale parameter with area size that also matters. For a fixed area size, the width of the confidence intervals for  $\mu$  increases with duration. Apart from an increased spatial correlation at long durations, the increase of the GEV scale parameter with duration is important here. The confidence intervals for the two other GEV parameters  $\gamma$  and  $\kappa$  are relatively wide at short and long durations.

## 5.5 Derivation of areal DDF curves and their uncertainties

Areal rainfall depth-duration-frequency (DDF) curves are derived by substituting the GEV-parameter-duration-area relationships (Eqs. (5.6) - (5.8)) into the quantile function of the GEV distribution (Eq. (5.3)). Thus, a mathematical expression is obtained for the  $D$ -h rainfall depth  $\hat{x}(T; D, A)$  that is exceeded on average once in  $T$  years in a region of size  $A$ :

$$\hat{x}(T; D, A) = \hat{\mu}(D, A) + \frac{\hat{\mu}(D, A)\hat{\gamma}(D, A) \left\{ 1 - [-\ln(1 - T^{-1})]^{\hat{\kappa}(D, A)} \right\}}{\hat{\kappa}(D, A)}. \quad (5.10)$$

This expression can be used to plot rainfall depths for durations from 15 min to 24 h and area sizes ranging from  $6 \text{ km}^2$  to  $1.7 \times 10^3 \text{ km}^2$  for a chosen return period  $T$ . Figure 5.3 shows

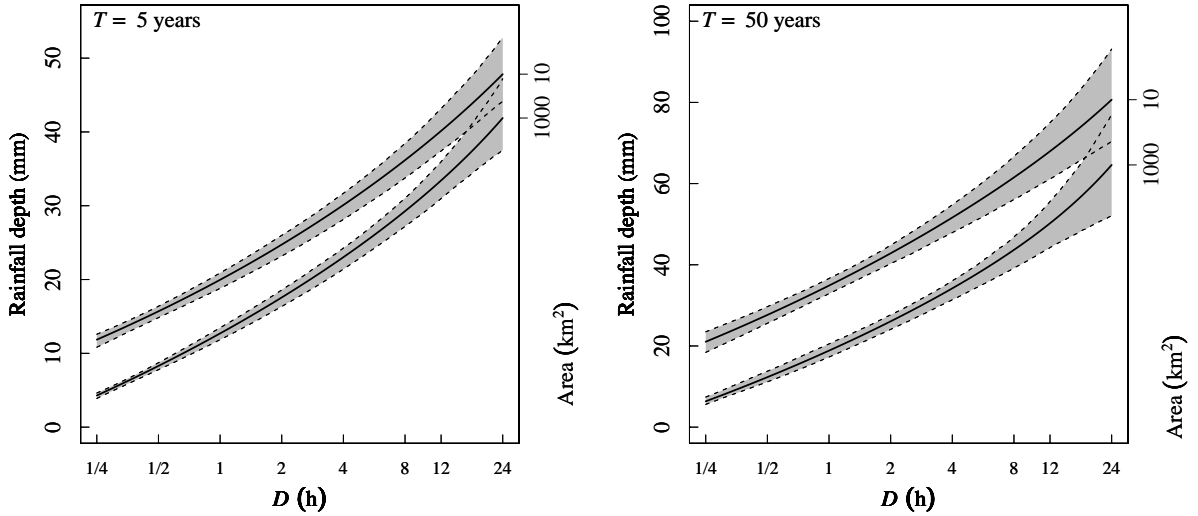


**Figure 5.3:** Areal rainfall DDF curves for a return period  $T$  of 5 (left) and 50 (right) years and  $A = 10$  and  $1000 \text{ km}^2$  based on radar data. The dashed lines represent pointwise 95%-confidence bands. Note that  $D$  is plotted on a logarithmic scale.

areal DDF curves for  $T = 5$  and 50 years and  $A = 10$  and  $1000 \text{ km}^2$ . If  $A$  increases from 10 to  $1000 \text{ km}^2$  a large areal reduction effect is found for both return periods, which becomes considerably stronger for short durations. For  $T = 50$  years and  $A = 1000 \text{ km}^2$ , rainfall depths increase from 6 to 65 mm for  $D = 15 \text{ min}$  to 24 h. The large upward curvature of the DDF curve for long durations if  $A = 1000 \text{ km}^2$ , is caused by the relatively small areal reduction at these durations.

A similar algorithm as used in Chapter 4 is applied to estimate the uncertainty in the DDF curves. Using the 1000 estimated relationships from the previous section, 1000 areal DDF curves are constructed for each  $A$  separately. For each areal DDF curve rainfall depths are derived for  $D = 15 \text{ min}$  to 24 h in steps of 1 min and the 1000 rainfall depths from each time step are ranked in increasing order. The 25th and 975th values are determined to obtain 95%-confidence intervals for the rainfall depth quantiles, shown as gray-shaded areas in Figure 5.3. Uncertainties become large for long durations. For example, the width of the 95%-confidence interval ranges from 4 mm for  $D = 60 \text{ min}$  to 23 mm for  $D = 24 \text{ h}$  if  $A = 10 \text{ km}^2$  and  $T = 50$  years. This increase is relatively large compared to that in the amount of rainfall, which changes from 35 to 81 mm according to the DDF curve.

The confidence intervals for  $A = 1000 \text{ km}^2$  are narrower than those for  $A = 10 \text{ km}^2$ , except for  $D$  larger than approximately 18 h. This holds both for  $T = 5$  and  $T = 50$  years. The smaller width for  $A = 1000 \text{ km}^2$  over a long range of durations is due partly to the lower uncertainty of the dispersion coefficient for these durations and partly to the fact that the

quantiles for  $A = 1000 \text{ km}^2$  are lower than the corresponding quantiles for  $A = 10 \text{ km}^2$ .

For  $T = 50$  years, the width of the 95%-confidence band for the DDF curve for  $A = 10 \text{ km}^2$  reaches a minimum for  $D = 1 \text{ h}$ . This is related to the small width of the 95%-confidence intervals for the modeled parameters  $\gamma$  and  $\kappa$  for respectively  $D$  is 30-60 min and 1-2 h. For  $A = 1000 \text{ km}^2$ , these intervals for  $\gamma$  and  $\kappa$  are relatively short for respectively  $D$  is 1 h and 2.5 - 6.5 h. Because these durations differ considerably, a minimum width of the 95%-confidence band for the DDF curve is not found beyond  $D = 15 \text{ min}$ . Moreover, Figure 5.3 reveals that for the two area sizes the confidence intervals do not overlap for most durations, implying that the areal DDF curves differ significantly.

Eq. (5.10) is used to obtain a contour plot of rainfall depths for  $D = 15 \text{ min}$  to  $24 \text{ h}$  and  $A = 6 \text{ km}^2$  to  $1.7 \times 10^3 \text{ km}^2$  for  $T = 5$  and  $50$  years (Figure 5.4). Strong gradients are found at short durations and small area sizes.

## 5.6 Areal reduction factors

In this section, areal reduction factors (ARF) are derived from weather radar and compared with those obtained from rain gauges. ARFs are used to convert percentiles of point rainfall to percentiles of areal rainfall. In general, only local high-density rain gauge networks are available to calculate ARFs, which are assumed to be valid for other regions with less dense rain gauge networks. Some studies utilizing rain gauge data to calculate ARFs are NERC (1975), Bell (1976), Omolayo (1993), and Allen and DeGaetano (2005a). Studies using radar data to estimate ARFs are Durrans et al. (2002), Allen and DeGaetano (2005b) and Lombardo et al. (2006).

Areal reduction factors are defined as a ratio of rainfall depth quantiles:

$$\widehat{\text{ARF}}(T; D, A) = \frac{\hat{x}(T; D, A)}{\hat{x}(T; D, A_0)}, \quad (5.11)$$

where  $A \geq A_0$  and  $A_0$  is usually the horizontal entry surface of the rain gauge funnel (gauge-based ARF). The area-averaged rainfall depths are calculated from a (weighted) average of point rainfall depths. In this chapter, the radar-based areal DDF curves are employed to calculate ARFs, for which  $A_0 = 6 \text{ km}^2$ . Radar-based ARFs can only be derived for area sizes from  $A = 6 \text{ km}^2$ , since Eqs. (5.6) - (5.8) are not appropriate for extrapolation to smaller area sizes. Moreover, one could question what area size a radar pixel represents, because the radar data have been adjusted to point measurements from rain gauge networks. It is expected, however, that this adjustment has little effect on the representativity of the data from one pixel because a smooth adjustment field has been used rather than an exact match with the point measurements. From the gauge-based ARFs in the UK Flood Studies Report (NERC, 1975) it can be concluded that the areal reduction of quantiles between a point and a radar pixel is small for  $D = 24 \text{ h}$  but not for short durations. These ARFs were based on rain gauge networks in the UK, particularly from the southern part, its climate being comparable to that of the Netherlands.



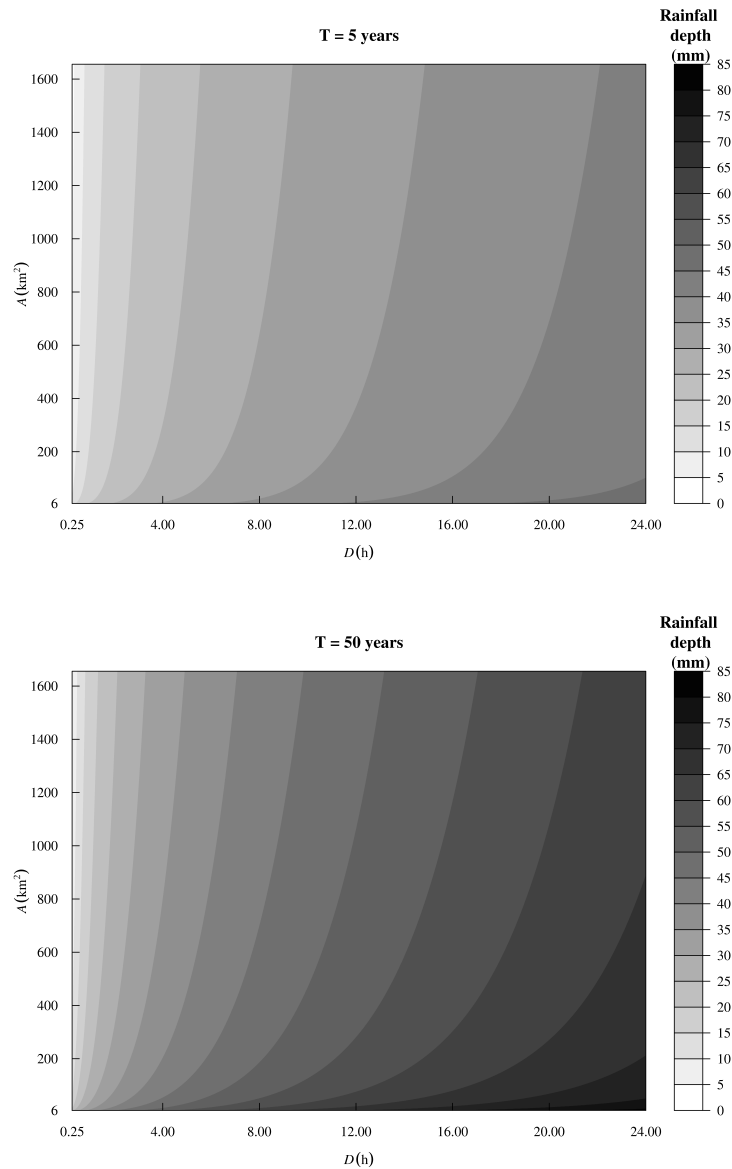


**Figure 5.4:** Rainfall depths as a function of duration and area size for durations of 15 min to 24 h and area sizes of 6 km<sup>2</sup> (one radar pixel) to  $1.7 \times 10^3$  km<sup>2</sup> for a return period  $T$  of 5 (top) and 50 (bottom) years.

Radar-based ARFs for  $D = 24$  h can thus be directly compared with gauge-based ARFs. Table 5.3 shows that the ARFs for  $T = 2$  years agree well with those from NERC (1975). The table also presents ARFs for  $D = 15$  min and 1 h. The areal reduction effect becomes large for  $D = 15$  min, for example,  $\text{ARF} = 0.37$  for  $A = 1000$  km<sup>2</sup>. For such short durations, an adjustment factor should be applied to the gauge-based ARFs to obtain ARFs which can be compared with those based on radar data. Therefore, gauge-based ARFs for  $A = 100$  and 1000 km<sup>2</sup> are divided by the ARF for  $A = 6$  km<sup>2</sup> from NERC (1975). Table 5.3 reveals that

the adjusted ARFs are in good agreement with those based on radar data for  $D = 15$  min, 1 h and 24 h.

Figure 5.5 displays radar-based areal reduction factors as a function of duration (left panel) and as a function of area size (right panel) and reveals a clear influence of the chosen return period. Particularly for area sizes up to  $500 \text{ km}^2$ , the ARFs decrease substantially with area size and this decline becomes more pronounced if a return period of 50 years instead of 2 years is chosen. This holds both for short and long durations. These results indicate that very rare events have relatively strong spatial gradients. In particular, for long durations widespread stratiform rainfall becomes more important for the less extreme events. It should be noted, however, that with increasing  $A$  the likelihood increases that the annual maxima within the region occur on different dates or, in the case of very short durations, on consecutive  $D$ -min intervals. Figure 5.5 further shows a strong decline in the AFRs at short durations. Almost the same decline is found if the interaction terms in Eqs. (5.7) and (5.8) are omitted.

Generally, high-density rain gauge networks are needed to calculate ARFs. These results show that radar data are also suitable to derive ARFs with respect to the size of a radar pixel.

## 5.7 Discussion and conclusions

An 11-year radar data set of precipitation depths was used to derive an extreme areal rainfall climatology for the Netherlands. This high-quality radar data set was obtained after adjustments using rain gauge data (Chapters 3 and 4). Annual rainfall maxima were abstracted for durations of 15 min to 24 h and area sizes of 6 to  $1.7 \times 10^3 \text{ km}^2$ . A GEV distribution was fitted to the annual maxima for each duration and area size separately. The GEV parameters were modeled as a function of duration and area size. These relationships were employed to derive areal rainfall depth-duration-frequency curves and their uncertainties. Finally, areal reduction factors were calculated.

**Table 5.3:** Areal reduction factors for  $T = 2$  years and  $A = 100$  or  $1000 \text{ km}^2$ .

	15 min	1 h	24 h
$A = 100 \text{ km}^2$			
Radar	0.70	0.84	0.96
NERC (1975)	0.64	0.79	0.94
NERC (1975) adjusted	0.73	0.85	0.96
$A = 1000 \text{ km}^2$			
Radar	0.37	0.67	0.91
NERC (1975)	0.39	0.62	0.89
NERC (1975) adjusted	0.44	0.67	0.91

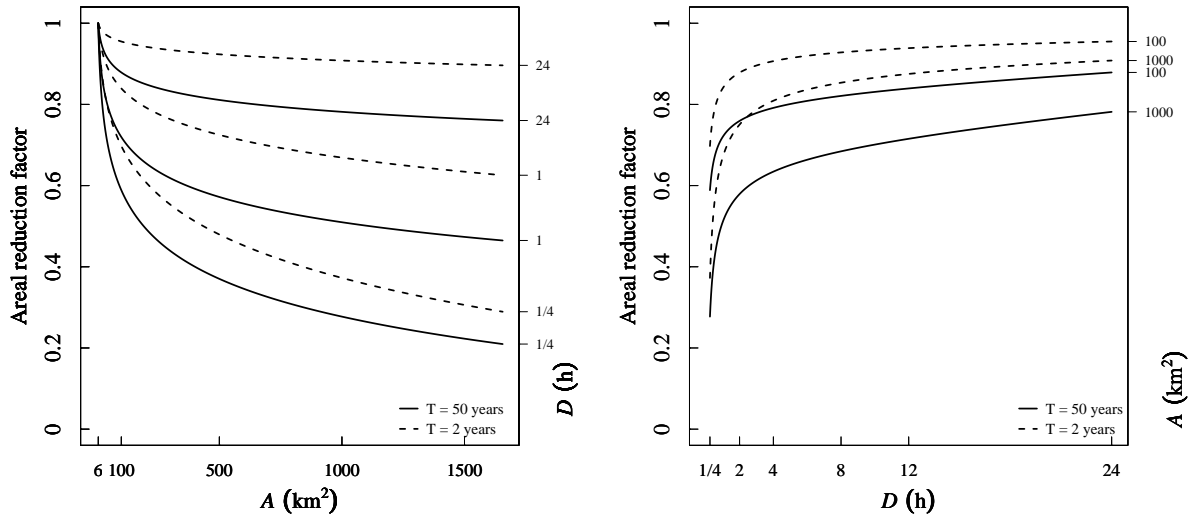


**Figure 5.5:** Radar-based areal reduction factors plotted against duration for  $A = 100$  and  $1000 \text{ km}^2$  (left) and plotted against area size for  $D = 15 \text{ min}$ ,  $60 \text{ min}$  and  $24 \text{ h}$  (right) for  $T = 2$  and  $50$  years.

This chapter presents a novel approach in the estimation of extreme areal rainfall by modeling GEV parameters as a function of both duration and area size employing weather radar data. Areal rainfall DDF curves are obtained by substituting these semi-empirical models into the quantile function of the GEV distribution. For each duration the annual maximum precipitation depths follow a GEV distribution. Goodness of fit tests show that the GEV distributions provide an adequate fit. The GEV distribution generally no longer holds if each DDF curve would have been obtained from a relationship that models the desired quantile as a function of specifically chosen durations. To the authors' knowledge this chapter is the first to show that rainfall DDF curves and their uncertainties for different area sizes can be derived from weather radar.

Although radar data have proven to be valuable in the estimation of extreme areal rainfall depths, some issues remain. First, in Chapter 4 it was found that for short durations radar-based rainfall quantiles, obtained by fitting a GEV distribution to the annual maximum rainfalls at the radar pixels, are systematically smaller than those based on rain gauge data for the same period. This is probably due to remaining errors in the radar rainfall data and can to some extent be attributed to an areal reduction effect as well. The problem is that only few rain gauge measurements with a high temporal resolution are available to adjust radar data. If long time series of volumetric radar data become available, new possibilities arise to address this underestimation for short durations, for instance, by developing a vertical profile of reflectivity correction. Second, as a result of the limited length of the time series of annual maxima and the reduction of the number of nonoverlapping regions with

growing area size, the uncertainty of the GEV shape parameter is large for large area sizes. Further, the confidence bands about the DDF curves become rather wide for long durations. On the other hand, the density of rain gauge networks is usually too low to obtain reliable estimates of extreme areal rainfall for subdaily durations.

The estimated uncertainties in GEV parameters and areal DDF curves do only represent uncertainties due to sampling variability. Uncertainties due to the choice of the distribution or those caused by measurement or retrieval errors were not taken into account.

For  $D = 24$  h, it has been shown that the ARFs based on radar data agree well with those obtained from rain gauges. For subdaily data, it makes a difference whether ARFs are calculated with respect to a radar pixel or a point, as was already discussed by Frederick et al. (1977). Therefore, an adjustment factor was applied to the gauge-based ARFs, resulting in similar values of the ARFs as those based on radar data. A remaining problem is that the adjustment of radar rainfall depths using rain gauge data results in a decline in the effective area size a radar pixel is representative of, which complicates the selection of an appropriate adjustment factor. This problem becomes less pronounced if radar data with the regularly used 1-km spatial resolution are available. Further, X-band radars, such as the recently developed high-resolution drizzle radar (Figueras i Ventura and Russchenberg, 2009), hold a promise in studying extreme areal rainfall at very small spatial scales.

Weather radars are suitable to model extreme areal rainfall, which can be used for design purposes in water management and verification of weather and climate models. The presented methodology is applicable to other radar data sets as well. With the long radar data sets that become available and the large coverage of weather radar networks in, for instance, the United States and Europe, radar has the potential to become an important tool in the estimation of extreme areal rainfall depths for given return periods.

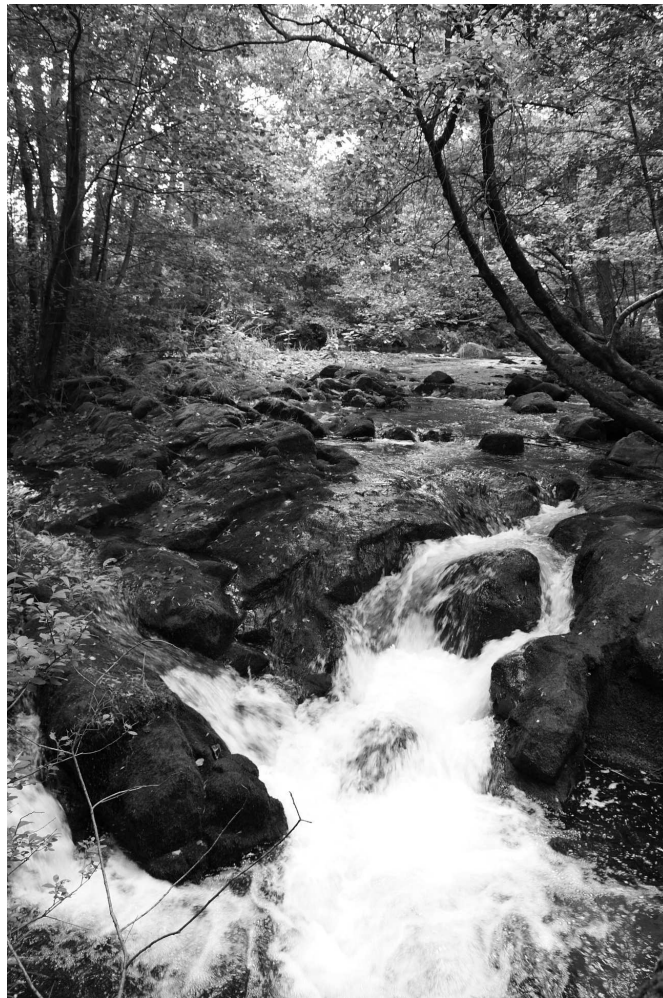
## Acknowledgements

We thank Rudolf van Westrhenen (KNMI) for archiving more than five years of radar data in the period 1998-2003.

## Chapter 6

---

### Conclusions and outlook



## 6.1 Summary

Extreme rainfall climatologies were obtained from rain gauges and weather radar for the Netherlands. In Chapter 2 a methodology was developed to obtain rainfall depth-duration-frequency (DDF) curves and their uncertainties based on rain gauge data. The Generalized Extreme Value (GEV) distribution was used to model annual rainfall maxima. An equation was derived which describes the rainfall depth for durations between 1 and 24 h for given return periods. Subsequently, a high-quality climatological radar rainfall data set was obtained in Chapter 3 by adjusting the radar data with rain gauges. In Chapter 4, GEV distributions were fitted to annual radar rainfall maxima for durations of 15 min to 24 h and an area size of 6 km<sup>2</sup> (a radar pixel) to obtain rainfall DDF curves. In addition, the regional variability in extreme rainfall was studied. Finally, annual areal maxima were abstracted in Chapter 5 for area sizes of one radar pixel to  $1.7 \times 10^3$  km<sup>2</sup> to derive areal rainfall DDF curves.

## 6.2 Conclusions

- *How to quantify the uncertainty in rainfall depth-duration-frequency (DDF) curves?*

The bootstrap method was used in Chapters 2, 4 and 5 to estimate the uncertainty in DDF curves due to sampling variability, which is an important part of the total uncertainty. Confidence bands for the DDF curves were obtained by re-estimating the relationships which describe the GEV parameters as a function of duration. Although probability plots (Chapters 2 and 4) and the Anderson-Darling test (Chapter 5) indicate that the GEV distribution fits well, there remains an uncertainty about the choice of the distribution, which is hard to estimate and which was not incorporated. In addition, measurement errors will give a further increase in the uncertainties of DDF curves. These errors are also difficult to quantify. This implies that the total uncertainty of a DDF curve will be larger than the obtained uncertainties in Chapters 2, 4 and 5.

Because 514 annual maxima were concatenated into one record in Chapter 2, the uncertainties in estimated rainfall depths are smaller compared to Smits et al. (2004), who used a 98-year record. The large number of radar pixels in space compensates for the relatively small number of years, leading to a data set with an effective length of the order of 80 years for a duration of 24 h in Chapter 4. For short durations the effective length is even much larger due to the lower spatial correlation. As a consequence, the uncertainties in the radar-based DDF curves are small for short durations but become rather large for long durations. This holds both for rainfall at a radar pixel and rainfall over larger regions.

- *How reliable are the rainfall depths for given return periods based on weather radar?*

A comparison of radar-based GEV parameters with those based on rain gauges reveals that for short durations the GEV location parameter is underestimated. This is probably due to remaining errors in the radar data for subdaily durations, such as changes in the vertical profile of reflectivity and attenuation. A spatial adjustment with a high temporal resolution

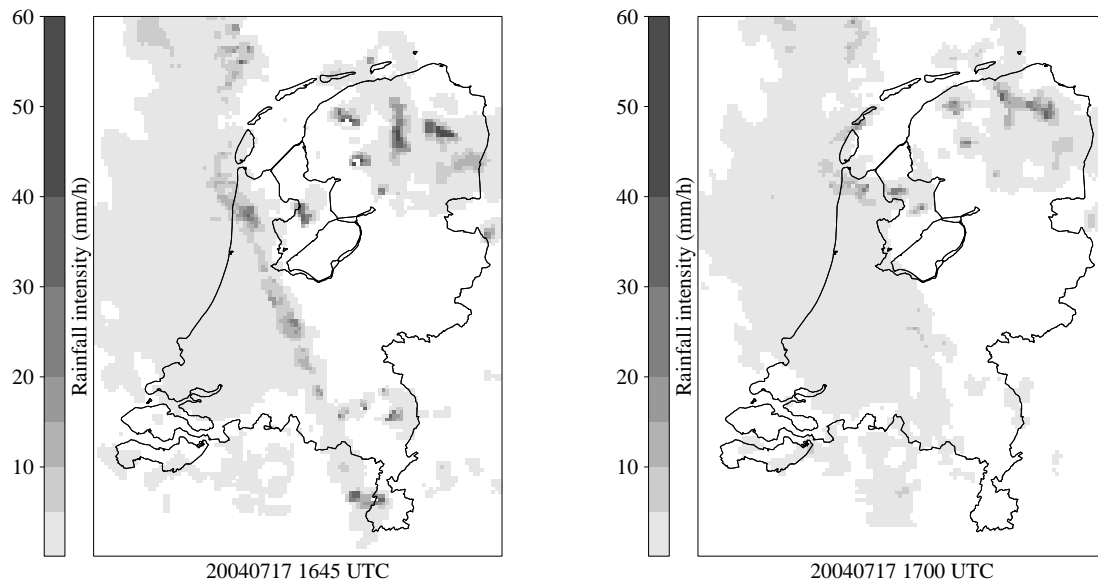


**Figure 6.1:** Maps showing radar rainfall intensities from two successive time steps. A squall line moves from southwest to northeast and severely attenuates the radar signals in the second time step (right).

may reduce these errors. This requires, however, a considerable increase in the density of the automatic rain gauge network, which will be quite expensive. An extreme case of attenuation is displayed in Figure 6.1. A squall line with high rainfall intensities moves in northeasterly direction across the Netherlands (left) and 15 minutes later the squall line has almost completely disappeared (right). Usually, one radar can compensate for the other radar, however, in this case the squall line is exactly between the two radars, so that the transmitted radiation of both radars is attenuated severely.

To account for regional differences in the annual maximum distributions, it was assumed that the shape parameter and dispersion coefficient were constant over the Netherlands but that the location parameter varies over the radar pixels (index flood assumption). The parameters were estimated by a maximum likelihood procedure that was stopped after one iteration. A small simulation study showed that further maximization of the likelihood function did not result in better parameter estimates if the length of the available records is as short as 11 years. An average DDF curve for the Netherlands was obtained by averaging the estimated location parameters. When rainfall DDF curves are derived for each radar pixel, using the index flood method, this results in too large uncertainties in the estimated quantiles of rainfall depths because of the large uncertainty of the location parameter. As a compromise, local DDF curves were obtained by assuming that this parameter is constant over a number of adjacent pixels.

From 1998 to January 2001, the radar rainfall depths were based on the De Bilt radar only, because of an elevation bias in the Den Helder data. It is to be expected that incorporating the Den Helder data will lead to an improved quality of rainfall observations at locations far from De Bilt, but relatively close to Den Helder. However, it may influence the extreme-value distributions over a large part of the country. To investigate this, mean-field bias and spatially (MFBS) adjusted daily and clock-hour rainfall depths were derived based on the De Bilt radar only (1998-2008). Subsequently, annual maxima were abstracted and the GEV parameters were estimated. The values of the GEV parameters hardly differ from those based on the data from the De Bilt (1998-2008) and the Den Helder (2001-2008) radar together. This also holds for the maps showing the regional differences in the location parameter (Figure 4.9). From this verification it is to be expected that the addition of the Den Helder radar from 2001 will only have a small influence on the results of the extreme rainfall analysis. This implies that only one radar is needed to derive a climatology of extreme rainfall within a radius of 190 km from the radar. This is valid for a flat country and if the radar data are adjusted using a spatial adjustment on daily rainfall depths (gauge density of 1 per 100 km<sup>2</sup>) and a mean-field bias adjustment on hourly rainfall depths (gauge density of 1000 km<sup>2</sup>).

- *Are regional differences in extreme rainfall significant for durations of 15 min to 24 h?*

Using 12 automatic rain gauges, in most cases no geographical variation in extreme rainfall could be found in Chapter 2. This may be attributed to the relatively short period of 29 years, which causes the uncertainty in the estimated GEV parameters to become rather large, or to the relatively small number of locations. Significant regional differences in extreme rainfall may be found if longer and more digitized time series of rainfall become available for subdaily durations. Buishand et al. (2009) found significant regional differences in the location parameter of the GEV distribution for daily rainfall depths obtained from 141 manual gauges in the Netherlands, which could only partially be attributed to differences in mean annual rainfall. Chapter 4 reveals that radar is a promising alternative for studying regional variability in extreme rainfall. For most durations from 15 min to 24 h, regional variability in the location parameter in the Netherlands is statistically significant. An important part of the differences can be attributed to randomness, being relatively large for an 11-year data set. Nevertheless, patterns of regional differences in the location parameter are comparable with those obtained from long rain gauge records for 24-h rainfalls (Buishand et al., 2009).

- *What is the value of weather radar to obtain areal DDF curves?*

A single equation was obtained from which rainfall depths for a chosen return period, and area size can be calculated for different durations: the areal DDF curve. Areal reduction factors (ARFs) were also derived. Comparison of these ARFs with those based on rain gauge data, reveals a good agreement. The ARFs were found to decrease with increasing return period, as was also reported by Bell (1976) and Witter (1984). A problem is that the uncertainty of the shape parameter is very large for large area sizes. This parameter is relevant if long return periods (> 50 years) are of interest. Another problem is that the effective area the ad-



justed radar rainfall depths from a radar pixel are representative of might be smaller than 6 km<sup>2</sup>, its exact value being unknown. This problem will become less pronounced when radar data with a 1-km horizontal resolution are available. Further, regional variability in extreme areal rainfall was not studied. Despite these limitations, the obtained extreme rainfall climatology already has proven to be useful, because the density of rain gauge networks is usually too low to obtain reliable estimates of extreme areal rainfall for subdaily durations.

- *Main conclusion*

Only some attempts have been undertaken to obtain extreme rainfall statistics using weather radar and, specifically, regional variability in extreme rainfall as well as the derivation of rainfall DDF curves have not been described before. In this thesis a high-quality re-processed radar data set was obtained, one of the longest described in the literature. Specific attention was given to the estimation of the uncertainty in rainfall DDF curves. The main result of this thesis is that weather radar technology has matured and can be used to derive a climatology of extreme (areal) rainfall including the uncertainties and can be used to study regional differences in extreme rainfall. Therefore, it is to be expected that the radar-based extreme rainfall statistics will gradually replace those derived from rain gauges. Note, however, that for the time being, rain gauges remain necessary to obtain high-quality radar rainfall depths. In addition, in some parts of the world weather radars are not operational.

## 6.3 Outlook

### 6.3.1 The future of QPE

Chapter 4 showed that extreme radar rainfall depths are smaller than those obtained from rain gauges for short durations. If long time series of volumetric radar data are available, these can be used to improve radar rainfall depths, so that they become less prone to changes in the volumetric profile of reflectivity at short durations. Moreover, although the obtained climatologies of extreme rainfall based on weather radar are already useful, clearly longer records are needed to reduce the uncertainty in extreme rainfall depths. An additional 10 years of data would make the derivation of DDF curves for a radar pixel more feasible and would result in a more reliable study of regional differences in extreme rainfall.

An interesting development is the installation of radars with dual-polarization capability in several European countries, such as Germany, France and the United Kingdom. Moreover, the 171 NEXRAD radars covering the United States are being upgraded to dual-polarization radars the coming years. This type of radar holds a promise for correction for attenuation and determination of the precipitation type (Bringi and Chandrasekar, 2001). This will lead to a better discrimination between rain, hail, ground clutter and other spurious echoes, resulting in a better retrieval of rainfall intensities from radar reflectivities. Dual-polarization radars of the X-band type are specifically suited for urban areas, because of their high spatial resolution, with radar pixels smaller than 1 km<sup>2</sup>. These radars have a range of typically 50 km and the lower cost per unit compared to radars of the C-band type makes it feasible

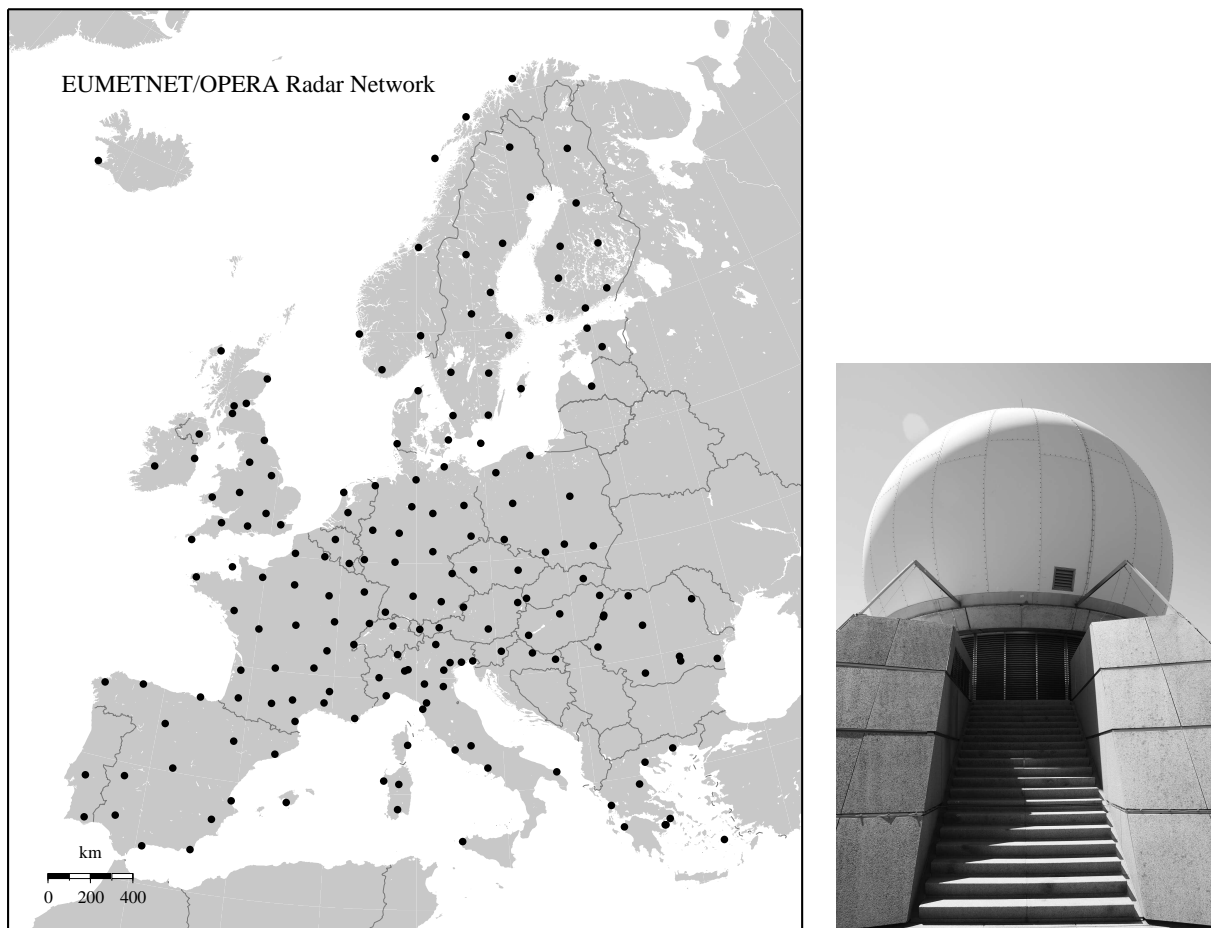


**Figure 6.2:** Map of Europe showing the locations of the 180 operational weather radars (left) and a photograph of one of these radars, operated by Météo France, and located on Le Grand Ballon, the highest summit of the Vosges mountains (1424 m), France (right).

to install a network of X-band radars. Such a network would be interesting for orographic areas to overcome shielding errors and to be able to issue flash flood warnings. It remains to be seen whether technological improvement of weather radar systems and new adjustment procedures using volumetric radar data will be sufficient to reduce the need for adjustment methods using rain gauges.

A promising new measurement technique of rainfall are cellular communication microwave links (Leijnse, 2007). The attenuation of the signal transmitted from one link to another can be converted to a path-averaged rainfall intensity close to the earth's surface. The vast network of commercial microwave links at the earth's surface gives new opportunities to obtain rainfall intensities with a temporal resolution of typically 15 min and with a high spatial resolution in urban areas. Such information could also be used to adjust instantaneous radar rainfall intensities. Microwave links also hold a promise for measuring rainfall in areas where few or no weather radars or rain gauges are available (Uijlenhoet, 2008; Delrieu et al., 2009).

QPE from satellites is performed using microwave remote sensing techniques, primarily by employing radiometers to retrieve cloud optical properties and radar. The Tropical Rainfall Measuring Mission (TRMM) is a successful example of QPE using satellites covering the globe from 35° S to 35° N with a revisit time up to several days. The Global Precipitation Measurement (GPM) Mission is envisaged to perform measurements including the mid-latitudes with a revisit time of 3 h and a horizontal resolution of 4-5 km and will even be able to obtain 3-D global precipitation maps with a vertical resolution of 250 m (Uijlenhoet, 2008). Strangeways (2007) expects that the future of precipitation measurement mainly consists of combining rain gauge data with satellite data. This will certainly be the case for global precipitation estimation, since radars are more sparse than rain gauges. However, note that over large parts of the oceans the only source of precipitation measurements comes from satellites. In addition, the author of this thesis expects that ground-based weather radars will become dominant in QPE in the developed countries, which contain many of the world's densely populated areas. For the time being, a multi-sensor approach using weather radar and rain gauges is to be recommended.

The SEVIRI instrument on board of the Meteosat Second Generation (MSG) satellites scans the complete disk of the earth every 15 minutes. The short revisit time is an advantage over the TRMM and GPM satellites, however, the MSG does not carry an active precipitation radar, leading in general to less accurate precipitation estimates. Roebeling and Holleman (2009) show that rainfall intensities retrieved from MSG during daytime agree reasonably well with those based on unadjusted weather radar data for an area in the Netherlands. This holds a promise for using the MSG satellites for QPE during daytime over areas for which no precipitation observations are available.

The use of radar rainfall data as input for hydrological models is increasing. For example, Germann et al. (2009) express the uncertainty in radar rainfall depths by creating an ensemble of radar precipitation fields, which are used as input for an hydrological model to obtain an ensemble of hourly runoff for a 44-km<sup>2</sup> Alpine subcatchment. In addition, they show that runoffs based on deterministic radar data are comparable with those based on gauge data. Schuurmans and Bierkens (2007) study the influence of spatial variability of daily rainfall and hydrological variables on, for instance, discharge using a distributed hydrological model. They show that operational radar rainfall products are suitable for use in hydrological models. Usually only data from one or a few rain gauges are available in a catchment, which makes radar an interesting alternative.

### 6.3.2 Applications of climatological radar rainfall data sets

It has been shown that the climatological radar data set, developed in Chapters 3 and 4, has a high-quality<sup>1</sup>. Because the data set has a high temporal and spatial resolution and covers an entire country, it could also be used:

---

<sup>1</sup>The climatological radar data set of 1-hour rainfall depths from Chapter 3 is available at KNMI's Climate Services division.

- for parameterization of precipitation in weather and climate models
- for verification of the representation of extreme rainfall by climate models
- for verification of precipitation estimates from satellites
- for simulations for satellites which are to be launched
- as input for hydrological or ground water models
- for research on fog formation, air pollution, phenology or traffic density

The presented adjustment methods can be used on radar data sets from other countries as well. Many meteorological services will operate rain gauge networks with a comparable or higher density. However, for several European countries more difficulties will be encountered in constructing a high-quality radar data set of rainfall depths. For example, Nordic countries suffer from errors related to their cold climate (Koistinen et al., 2004) and in mountainous countries, such as Switzerland, (partial) shielding and ground clutter can be a severe problem (Germann and Joss, 2004). Further, constructing such long radar data sets over large areas requires some careful choices to be made, because it is computationally demanding, specifically because of the large i/o times due to file processing. Because of this, the use of long time series of volumetric data provides an additional challenge. Further, comparison of the quality of climatological radar data sets from the literature is difficult, because of different climates, the use of other measures of fit and different selection criteria.

Other countries generally exhibit larger spatial differences in extreme rainfall than the Netherlands. A computationally more intensive likelihood procedure is then needed to estimate the parameters of the GEV distribution under the index flood assumption than the one-step maximization used in Chapter 4. There might be even regional differences in the dispersion coefficient and the shape parameter, so that the index flood method is not appropriate anymore. A possible approach is to link these GEV parameters to mean annual rainfall, see, e.g., Brath et al. (2003). This may result in rather complex expressions for the DDF curves, in particular in the case of areal rainfall.

The changing climate could lead to an increase in the severity of extreme rainfall events (Frei et al., 2006; Lenderink and Van Meijgaard, 2008). Radar holds a promise to frequently update extreme rainfall statistics for short durations. Ten years of radar data are sufficient to obtain extreme rainfall statistics with a reasonable accuracy.

In Europe, more than 180 weather radars are operational, covering a large part of the continent (Figure 6.2). In the framework of the EUMETNET programme OPERA (Holleman et al., 2008), its European members are working on a new operational data centre where high-quality composites are derived from radar volume data. This enables the use of radar data for assimilation in numerical weather prediction models and as input for hydrological

models, which may lead to improved meteorological and hydrological forecasts. In addition, this opens the way to obtain a long-term radar data set over Europe, which can be employed to improve our understanding of the climate system (Collier, 1993) and of extreme rainfall events.





# Bibliography

- Ahmad, M. I., C. D. Sinclair, and B. D. Spurr, 1988: Assessment of flood frequency models using empirical distribution function statistics. *Water Resources Research*, **24**, 1323–1328.
- Alila, Y., 1999: A hierarchical approach for the regionalization of precipitation annual maxima in Canada. *Journal of Geophysical Research*, **104 (D24)**, 31 645–31 655.
- Allen, R. J. and A. T. DeGaetano, 2005a: Areal reduction factors for two eastern United States regions with high rain-gauge density. *Journal of Hydrologic Engineering*, **10**, 327–335, doi:10.1061/(ASCE)1084-0699(2005)10:4(327).
- , 2005b: Considerations for the use of radar-derived precipitation estimates in determining return intervals for extreme areal precipitation amounts. *Journal of Hydrology*, **315**, 203–219, doi:10.1016/j.jhydrol.2005.03.028.
- Ancona-Navarrete, M. A. and J. A. Tawn, 2002: Diagnostics for pairwise extremal dependence in spatial processes. *Extremes*, **5**, 271–285.
- Anderson, T. W. and D. A. Darling, 1952: Asymptotic theory of certain "goodness of fit" criteria based on stochastic processes. *The Annals of Mathematical Statistics*, **23**, 193–212.
- Atlas, D. and C. W. Ulbrich, 1977: Path- and area-integrated rainfall measurement by microwave attenuation in the 1-3 cm band. *Journal of Applied Meteorology*, **16**, 1322–1331.
- Baeck, M. L. and J. A. Smith, 1995: Climatological analysis of manually digitized radar data for the United States east of the Rocky Mountains. *Water Resources Research*, **31**, 3033–3049.
- Barnes, S. L., 1964: A technique for maximizing details in numerical weather map analysis. *Journal of Applied Meteorology*, **3**, 396–409.
- Bell, F. C., 1976: *The Areal Reduction Factor in Rainfall Frequency Estimation*. Report no. 35, Institute of Hydrology, Wallingford.
- Borga, M., F. Tonelli, R. J. Moore, and H. Andrieu, 2002: Long-term assessment of bias adjustment in radar rainfall estimation. *Water Resources Research*, **38**, 1226, doi:10.1029/2001WR000 555.

- Borga, M., C. Vezzani, and G. D. Fontana, 2005: Regional rainfall depth-duration-frequency equations for an Alpine region. *Natural Hazards*, **36**, 221–235.
- Brandes, E. A., 1975: Optimizing rainfall estimates with the aid of radar. *Journal of Applied Meteorology*, **14**, 1339–1345.
- Brath, A., A. Castellarin, and A. Montanari, 2003: Assessing the reliability of regional depth-duration-frequency equations for gaged and ungaged sites. *Water Resources Research*, **39**, 1367, doi:10.1029/2003WR002399.
- Bringi, V. N. and V. Chandrasekar, 2001: *Polarimetric Doppler Weather Radar: Principles and Applications*. Cambridge University Press, Cambridge.
- Buishand, T. A., 1984: Bivariate extreme-value data and the station-year method. *Journal of Hydrology*, **69**, 77–95.
- , 1989: Statistics of extremes in climatology. *Statistica Neerlandica*, **43**, 1–30, doi:10.1111/j.1467-9574.1989.tb01244.x.
- , 1991: Extreme rainfall estimation by combining data from several sites. *Hydrological Sciences Journal*, **36**, 345–365.
- , 1993: Rainfall depth-duration-frequency curves; a problem of dependent extremes. *Statistics for the Environment*, Barnett, V. and K. F. Turkman, Eds., Wiley, Chichester, 183–197.
- Buishand, T. A., L. De Haan, and C. Zhou, 2008: On spatial extremes: with application to a rainfall problem. *The Annals of Applied Statistics*, **2**, 624–642, doi:10.1214/08-AOAS159.
- Buishand, T. A., R. Jilderda, and J. B. Wijngaard, 2009: *Regionale verschillen in extreme neerslag*. Scientific report WR-2009-01, KNMI, De Bilt, available via [www.knmi.nl/bibliotheek/knmipubWR/WR2009-01.pdf](http://www.knmi.nl/bibliotheek/knmipubWR/WR2009-01.pdf) (in Dutch).
- Buishand, T. A., J. B. M. Van Acker, and H. Van Luijtelaar, 1991: Analyse van kwartiersommen van de neerslag. *H<sub>2</sub>O*, **24**, 294–299 (in Dutch).
- Buishand, T. A. and C. A. Velds, 1980: *Neerslag en Verdamping*. KNMI, De Bilt (in Dutch).
- Buishand, T. A. and J. B. Wijngaard, 2007: *Statistiek van extreme neerslag voor korte neerslagduren*. Technical report TR-295, KNMI, De Bilt, available via [www.knmi.nl/publications/fulltexts/tr295.pdf](http://www.knmi.nl/publications/fulltexts/tr295.pdf) (in Dutch).
- Burn, D. H., 2003: The use of resampling for estimating confidence intervals for single site and pooled frequency analysis. *Hydrological Sciences Journal*, **48**, 25–38.



- Carbone, R. and J. D. Tuttle, 2008: Rainfall occurrence in the U.S. warm season: the diurnal cycle. *Journal of Climate*, **21**, 4132–4146, doi:10.1175/2008JCLI2275.1.
- Ciach, G. J. and W. F. Krajewski, 1999: On the estimation of radar rainfall error variance. *Advances in Water Resources*, **22**, 585–595.
- , 2006: Analysis and modeling of spatial correlation structure in small-scale rainfall in Central Oklahoma. *Advances in Water Resources*, **29**, 1450–1463, doi:10.1016/j.advwatres.2005.11.003.
- Cleveland, W. S., 1979: Robust locally weighted regression and smoothing scatterplots. *Journal of the American Statistical Association*, **74**, 829–836.
- Coles, S., 2001: *An Introduction to Statistical Modeling of Extreme Values*. Springer, London.
- Coles, S. G., 1993: Regional modelling of extreme storms via max-stable processes. *Journal of the Royal Statistical Society, Series B*, **55**, 797–816.
- Coles, S. G. and M. J. Dixon, 1999: Likelihood-based inference for extreme value models. *Extremes*, **2**, 5–23.
- Coles, S. G. and J. A. Tawn, 1996: Modelling extremes of the areal rainfall process. *Journal of the Royal Statistical Society, Series B*, **58**, 329–347.
- Collier, C. G., 1989: *Applications of Weather Radar Systems: a Guide to Uses of Radar Data in Meteorology and Hydrology*. Ellis Horwood Limited, Chichester, England.
- , 1993: The application of a continental-scale radar database to hydrological process parametrization within Atmospheric General Circulation Models. *Journal of Hydrology*, **142**, 301–318.
- Croft, P. J. and M. D. Shulman, 1989: A five-year radar climatology of convective precipitation for New Jersey. *International Journal of Climatology*, **9**, 581–600.
- Dekker, A., H. Van Gasteren, W. Bouten, J. Shamoun-Baranes, A. Borst, I. Holleman, A. Dokter, A. Ginati, and G. Garofalo, 2008: The European Space Agency's Flysafe project, looking at the bird strike problem from another perspective. *Proceedings of the 28th meeting of the International Bird Strike Committee*, International Bird Strike Committee, s.l., available via <http://dare.uva.nl/record/295060>.
- Delbeke, L., 2000: *Extreme Neerslag in Vlaanderen; nieuwe IDF-curve gebaseerd op langdurige meetreeksen van neerslag*. Koninklijk Meteorologisch Instituut, Ukkel (in Dutch).
- Delrieu, G., I. Braud, A. Berne, M. Borga, B. Boudevillain, F. Fabry, J. Freer, E. Gaume, E. Nakakita, A. Seed, P. Tabary, and R. Uijlenhoet, 2009: Weather radar and hydrology. *Advances in Water Resources*, **32**, 969–974, doi:10.1016/j.advwatres.2009.03.006.

- Diaconis, P. and B. Efron, 1983: Computer-intensive methods in statistics. *Scientific American*, **248**, 96 – 108.
- Doviak, R. J. and D. S. Zrnić, 1993: *Doppler Radar and Weather Observations*. 2d ed., Dover Publications, Inc., Mineola, New York.
- Durrans, S. R., L. T. Julian, and M. Yekta, 2002: Estimation of depth-area relationships using radar-rainfall data. *Journal of Hydrologic Engineering*, **7**, 356 – 367, doi:10.1061/(ASCE)1084-0699(2002)7:5(356).
- Efron, B. and R. J. Tibshirani, 1993: *An Introduction to the Bootstrap*. Chapman & Hall, New York.
- Faulkner, D. S. and D. A. Jones, 1999: The FORGEX method of rainfall growth estimation III: Examples and confidence intervals. *Hydrology and Earth System Sciences*, **3**, 205–212.
- Figueras i Ventura, J. and H. W. J. Russchenberg, 2009: Towards a better understanding of the impact of anthropogenic aerosols in the hydrological cycle: IDRA, IRCTR drizzle radar. *Physics and Chemistry of the Earth, Parts A/B/C*, **34**, 88–92, doi:10.1016/j.pce.2008.02.038.
- Fowler, H. J. and C. G. Kilsby, 2003: A regional frequency analysis of United Kingdom extreme rainfall from 1961 to 2000. *International Journal of Climatology*, **23**, 1313–1334.
- Frederick, R. H., V. A. Myers, and E. P. Auciello, 1977: Storm depth-area relations from digitized radar returns. *Water Resources Research*, **13**, 675–679.
- Frei, C., R. Schöll, S. Fukutome, J. Schmidli, and P. Vidale, 2006: Future change of precipitation extremes in Europe: Intercomparison of scenarios from regional climate models. *Journal of Geophysical Research*, **111**, D06 105.
- Gabella, M., J. Joss, G. Perona, and G. Galli, 2001: Accuracy of rainfall estimates by two radars in the same Alpine environment using gage adjustment. *Journal of Geophysical Research*, **106(D6)**, 5139–5150.
- Gellens, D., 2002: Combining regional approach and data extension procedure for assessing GEV distribution of extreme precipitation in Belgium. *Journal of Hydrology*, **268**, 113–126.
- , 2003: *Etude des précipitations extrêmes: Etablissement des fractiles et des périodes de retour d'événements pluviométriques*. Thèse de doctorat. Université Libre de Bruxelles (in French).
- Germann, U., M. Berenguer, D. Sempere-Torres, and M. Zappa, 2009: REAL - Ensemble radar precipitation estimation for hydrology in a mountainous region. *Quarterly Journal of the Royal Meteorological Society*, **135**, 445–456, doi:10.1002/qj.375.

- Germann, U., G. Galli, M. Boscacci, and M. Bolliger, 2006: Radar precipitation measurement in a mountainous region. *Quarterly Journal of the Royal Meteorological Society*, **132**, 1669–1692, doi:10.1256/qj.05.190.
- Germann, U. and J. Joss, 2002: Mesobeta profiles to extrapolate radar precipitation measurements above the Alps to the ground level. *Journal of Applied Meteorology*, **41**, 542–557.
- , 2004: Operational measurement of precipitation in mountainous terrain. *Weather Radar: Principles and Advanced Applications*, Meischner, P., Ed., Springer-Verlag, Berlin Heidelberg, 52–77.
- GREHYS, 1996: Inter-comparison of regional flood frequency procedures for Canadian rivers. *Journal of Hydrology*, **186**, 85–103.
- Gringorten, I. I., 1963: A plotting rule for extreme probability paper. *Journal of Geophysical Research*, **68**, 813–814.
- Hand, W. H., 1996: An object-oriented technique for nowcasting heavy showers and thunderstorms. *Meteorological Applications*, **3**, 31–41.
- Hershfield, D. M., 1961: *Rainfall Frequency Atlas of the United States: For Durations from 30 Minutes to 24 Hours and Return Periods from 1 to 100 Years*. Technical Paper No. 40, U.S. Department of Commerce, Weather Bureau, Washington D.C.
- Holleman, I., 2007: Bias adjustment and long-term verification of radar-based precipitation estimates. *Meteorological Applications*, **14**, 195–203, doi:10.1002/met.22.
- Holleman, I. and H. Beekhuis, 2005: *Review of the KNMI Clutter Removal Scheme*. Technical report TR-284, KNMI, De Bilt, available via [http://www.knmi.nl/publications/fulltexts/tr\\_clutter.pdf](http://www.knmi.nl/publications/fulltexts/tr_clutter.pdf).
- Holleman, I., L. Delobbe, and A. Zgonc, 2008: Update on the European weather radar network (opera). *Fifth European Conference on Radar in Meteorology and Hydrology*, 30 June - 4 July 2008, Helsinki, Finland.
- Hosking, J. R. M. and J. R. Wallis, 1997: *Regional Frequency Analysis: an Approach Based on L-moments*. Cambridge University Press, Cambridge.
- Hosking, J. R. M., J. R. Wallis, and E. F. Wood, 1985: Estimation of the generalized extreme-value distribution by the method of probability-weighted moments. *Technometrics*, **27**, 251–261.
- Jenkinson, A. F., 1955: The frequency distribution of the annual maximum (or minimum) values of meteorological elements. *Quarterly Journal of the Royal Meteorological Society*, **81**, 158–171.

- Joss, J. and R. Lee, 1995: The application of radar-gauge comparisons to operational precipitation profile corrections. *Journal of Applied Meteorology*, **34**, 2612–2630.
- Joss, J. and A. Waldvogel, 1990: Precipitation measurement and hydrology. *Radar in Meteorology*, Battan, L. J. and D. Atlas, Eds., American Meteorological Society, Boston, 577–606.
- Kitchen, M. and R. M. Blackall, 1992: Representativeness errors in comparisons between radar and gauge measurements of rainfall. *Journal of Hydrology*, **134**, 13–33.
- KNMI, 2000: *Handbook for the Meteorological Observation*. KNMI, 91-110 pp., available via <http://www.knmi.nl/samenw/hawa/download.html>.
- Koistinen, J., D. B. Michelson, H. Hohti, and M. Peura, 2004: Operational measurement of precipitation in cold climates. *Weather Radar: Principles and Advanced Applications*, Meischner, P., Ed., Springer-Verlag, Berlin Heidelberg, 78–114.
- Koistinen, J., H. Pohjola, and H. Hohti, 2003: Vertical reflectivity profile classification and correction in radar composites in Finland. *31st Conference on Radar Meteorology (Volume I)*, American Meteorological Society, Boston, 534–537.
- Koistinen, J. and T. Puhakka, 1981: An improved spatial gauge-radar adjustment technique. *Twentieth Conference on Radar Meteorology*, American Meteorological Society, Boston, 179–186, available via <http://ams.confex.com/ams/pdfpapers/64306.pdf>.
- Kok, C. J., B. G. J. W. Schreur, and D. H. P. Vogelesang, 2009: Meteorological support for anticipatory water management. *Atmospheric Research*, submitted.
- Koutsoyiannis, D., 2004: Statistics of extremes and estimation of extreme rainfall: II. Empirical investigation of long rainfall records. *Hydrological Sciences Journal*, **49**, 591–610.
- Koutsoyiannis, D. and G. Baloutsos, 2000: Analysis of a long record of annual maximum rainfall in Athens, Greece, and design rainfall inferences. *Natural Hazards*, **29**, 29–48.
- Koutsoyiannis, D., D. Kozonis, and A. Manetas, 1998: A mathematical framework for studying rainfall intensity-duration-frequency relationships. *Journal of Hydrology*, **206**, 118–135.
- Kysely, J. and J. Pícek, 2007: Regional growth curves and improved design value estimates of extreme precipitation events in the Czech Republic. *Climate Research*, **33**, 243–255.
- Leijnse, H., 2007: *Hydrometeorological Application of Microwave Links: Measurement of Evaporation and Precipitation*. PhD dissertation, Wageningen University, Wageningen, available via <http://library.wur.nl/wda/dissertations/dis4353.pdf>.
- Lenderink, G. and E. Van Meijgaard, 2008: Increase in hourly precipitation extremes beyond expectations from temperature changes. *Nature Geoscience*, **1**, 511 – 514, doi:10.1038/ngeo262.

- Lombardo, F., F. Napolitano, and F. Russo, 2006: On the use of radar reflectivity for estimation of the areal reduction factor. *Natural Hazards and Earth System Sciences*, **6**, 377–386.
- Madsen, H., P. S. Mikkelsen, D. Rosbjerg, and P. Harremoës, 2002: Regional estimation of rainfall intensity-duration-frequency curves using generalized least squares regression of partial duration series statistics. *Water Resources Research*, **38**, 1239, doi:10.1029/2001WR001125.
- Madsen, H., C. P. Pearson, and D. Rosbjerg, 1997a: Comparison of annual maximum series and partial duration series methods for modeling extreme hydrologic events. 2. Regional modeling. *Water Resources Research*, **33**, 759–769.
- Madsen, H., P. F. Rasmussen, and D. Rosbjerg, 1997b: Comparison of annual maximum series and partial duration series methods for modeling extreme hydrologic events. 1. At-site modeling. *Water Resources Research*, **33**, 747–757.
- Marshall, J. S., W. Hitschfeld, and K. L. S. Gunn, 1955: Advances in radar weather. *Advances in Geophysics*, Academic Press, New York, Vol. 2, 1–56.
- Marshall, J. S. and W. M. Palmer, 1948: The distribution of raindrops with size. *Journal of the Atmospheric Sciences*, **5**, 165–166.
- Martins, E. S. and J. R. Stedinger, 2000: Generalized maximum-likelihood generalized extreme-value quantile estimators for hydrologic data. *Water Resources Research*, **36**, 737–744.
- Menabde, M., A. Seed, and G. Pegram, 1999: A simple scaling model for extreme rainfall. *Water Resources Research*, **35**, 335–339.
- Michelson, D., T. Einfalt, I. Holleman, U. Gjertsen, K. Friedrich, G. Haase, M. Lindskog, and A. Jurczyk, (Eds.) , 2005a: *COST Action 717: Weather Radar Data Quality in Europe: Quality Control and Characterisation - Review*. EU Publications Office (Brussels), EUR 21955.
- Michelson, D. B., C. G. Jones, T. Landelius, C. G. Collier, G. Haase, and M. Heen, 2005b: ‘Down-to-Earth’ modelling of equivalent surface precipitation using multisource data and radar. *Quarterly Journal of the Royal Meteorological Society*, **131**, 1093–1112, doi:10.1256/qj.03.203.
- Michelson, D. B. and J. Koistinen, 2000: Gauge-radar network adjustment for the Baltic Sea Experiment. *Physics and Chemistry of the Earth, Part B: Hydrology, Oceans and Atmosphere*, **25**, 915–920.
- Mora, R. D., C. Bouvier, L. Neppel, and H. Niel, 2005: Regional approach for the estimation of low-frequency distribution of daily rainfall in the Languedoc-Roussillon region, France. *Hydrological Sciences Journal*, **50**, 17–29 (in French).

- Morrison, J. E. and J. A. Smith, 2002: Stochastic modeling of flood peaks using the generalized extreme value distribution. *Water Resources Research*, **38**, 1305, doi:10.1029/2001WR000502.
- Nelson, B. R., W. F. Krajewski, A. Kruger, J. A. Smith, and M. L. Baeck, 2003: Archival precipitation data set for the Mississippi River Basin: Algorithm development. *Journal of Geophysical Research*, **108**, No. D22, 8857, doi:10.1029/2002JD003158.
- NERC, 1975: *Flood Studies Report*. Natural Environment Research Council, London.
- Nicol, J. C. and G. L. Austin, 2003: Attenuation correction constraint for single-polarisation weather radar. *Meteorological Applications*, **10**, 345–354, doi:10.1017/S1350482703001051.
- Northrop, P. J., 2004: Likelihood-based approaches to flood frequency estimation. *Journal of Hydrology*, **292**, 96 – 113, doi:10.1016/j.jhydrol.2003.12.031.
- Nzeukou, A., H. Sauvageot, and L. F  ral, 2006: Rain rate and attenuation statistics along paths in a tropical coastal area from radar data. *Radio Science*, **41**, RS2005, doi:10.1029/2004RS003227.
- Omelayo, A. S., 1993: On the transposition of areal reduction factors for rainfall frequency estimation. *Journal of Hydrology*, **145**, 191–205.
- Press, W. H., S. A. Teukolsky, W. T. Vetterling, and B. P. Flannery, 1992: *Numerical Recipes in C: The Art of Scientific Computing*. 2d ed., Cambridge University Press.
- Probert-Jones, J. R., 1962: The radar equation in meteorology. *Quarterly Journal of the Royal Meteorological Society*, **88**, 485–495.
- Raghavan, S., 2003: *Radar Meteorology*. Kluwer Academic Publishers.
- Reed, D. W., D. S. Faulkner, and E. J. Stewart, 1999: The FORGEX method of rainfall growth estimation II: Description. *Hydrology and Earth System Sciences*, **3**, 197–203.
- Rinehart, R. E., 2004: *Radar for Meteorologists*. 4th ed., Rinehart Publications.
- Roebeling, R. and I. Holleman, 2009: SEVIRI rainfall retrieval and validation using weather radar observations. *Journal of Geophysical Research (Atmospheres)*, in press, doi:10.1029/2009JD012102.
- Rosenfeld, D. and E. Amitai, 1998: Comparison of WPMM versus regression for evaluating Z-R relationships. *Journal of Applied Meteorology*, **37**, 1241–1249.
- Rosenfeld, D., D. B. Wolff, and D. Atlas, 1993: General probability-matched relations between radar reflectivity and rain rate. *Journal of Applied Meteorology*, **32**, 50–72.

- Schaefer, M. G., 1990: Regional analyses of precipitation annual maxima in Washington State. *Water Resources Research*, **26**, 119–131.
- Schuurmans, J. M. and M. F. P. Bierkens, 2007: Effect of spatial distribution of daily rainfall on interior catchment response of a distributed hydrological model. *Hydrology and Earth System Sciences*, **11**, 677–693.
- Smith, W. H. F. and P. Wessel, 1990: Gridding with continuous curvature splines in tension. *Geophysics*, **55**, 293–305.
- Smits, I., J. B. Wijngaard, R. P. Versteeg, and M. Kok, 2004: *Statistiek van extreme neerslag in Nederland*. STOWA publicatie 2004-26, STOWA, Utrecht (*in Dutch*).
- Stedinger, J. R. and G. D. Tasker, 1985: Regional hydrologic analysis 1. Ordinary, weighted, and generalized least squares compared. *Water Resources Research*, **21**, 1421–1432.
- Steiner, M., J. A. Smith, S. J. Burges, C. V. Alonso, and R. W. Darden, 1999: Effect of bias adjustment and rain gauge data quality control on radar rainfall estimation. *Water Resources Research*, **35**, 2487–2503.
- Stewart, E. J., D. W. Reed, D. S. Faulkner, and N. S. Reynard, 1999: The FORGEX method of rainfall growth estimation I: Review of requirement. *Hydrology and Earth System Sciences*, **3**, 187–195.
- Strangeways, I., 2007: *Precipitation: Theory, Measurement and Distribution*. Cambridge University Press, Cambridge.
- Sveinsson, O. G. B., D. C. Boes, and J. D. Salas, 2001: Population index flood method for regional frequency analysis. *Water Resources Research*, **37**, 2733–2748.
- Uijlenhoet, R., 2008: Precipitation physics and rainfall observation. *Climate and the Hydrological Cycle*, Bierkens, M. F. P., A. J. Dolman, and P. A. Troch, Eds., IAHS Special Publication 8, International Association of Hydrological Sciences, Wallingford, 59–97.
- Uijlenhoet, R. and J. N. M. Stricker, 1999: A consistent rainfall parameterization based on the exponential raindrop size distribution. *Journal of Hydrology*, **218**, 101–127.
- U.S. Weather Bureau, 1964: *Two- to ten-day Precipitation for Return Periods of 2 to 100 Years in the Contiguous United States*. Technical Paper No. 49, U.S. Department of Commerce, Weather Bureau, Washington D.C.
- Van Luijtelea, H., 2006: *Stedelijke wateropgave: Vergelijking normen voor water op straat en inundatie*. Stichting RIONED, Ede, available via <http://www.riool.net/riool/shopping/products/overview.do> (*in Dutch*).

- Van Montfort, M. A. J. and J. V. Witter, 1986: The Generalized Pareto distribution applied to rainfall depths. *Hydrological Sciences Journal*, **31**, 151–162.
- Vignal, B., G. Galli, J. Joss, and U. Germann, 2000: Three methods to determine profiles of reflectivity from volumetric radar data to correct precipitation estimates. *Journal of Applied Meteorology*, **39**, 1715–1726.
- Vignal, B. and W. F. Krajewski, 2001: Large-sample evaluation of two methods to correct range-dependent error for WSR-88D rainfall estimates. *Journal of Hydrometeorology*, **2**, 490–504.
- Wauben, W., 2006: *KNMI Contribution to the WMO Laboratory Intercomparison of Rainfall Intensity Gauges*. Technical report TR-287, KNMI, De Bilt, available via <http://www.knmi.nl/~wauben>.
- Wessels, H. R. A. and J. H. Beekhuis, 1995: Stepwise procedure for suppression of anomalous ground clutter. *COST 75 Weather Radar Systems, International Seminar*, EUR 16013 EN, Luxembourg, 270–277.
- Willems, P., 2000: Compound intensity/duration/frequency-relationships of extreme precipitation for two seasons and two storm types. *Journal of Hydrology*, **233**, 189–205.
- Witter, J. V., 1984: *Heterogeneity of Dutch rainfall*. PhD dissertation, Wageningen University, Wageningen.
- WMO, 1981: *Guide to Hydrological Practices, Volume I - Data Acquisition and Processing*. WMO-No. 168, Section 4.2.1.2.2.
- Xie, H., X. Zhou, J. M. H. Hendrickx, E. R. Vivoni, H. Guan, Y. Q. Tian, and E. E. Small, 2006: Evaluation of NEXRAD stage III precipitation data over a semiarid region. *Journal of the American Water Resources Association*, **42**, 237–256.
- Young, C. B., A. A. Bradley, W. F. Krajewski, and A. Kruger, 2000: Evaluating NEXRAD multisensor precipitation estimates for operational hydrologic forecasting. *Journal of Hydrometeorology*, **1**, 241–254.
- Zondervan, J. G., 1978: *Modelling Urban Run-off; a Quasilinear Approach*. PhD dissertation, Centre for Agricultural Publishing and Documentation, Wageningen.
- Zucchini, W. and P. T. Adamson, 1989: Bootstrap confidence intervals for design storms from exceedance series. *Hydrological Sciences Journal*, **34**, 41–48.



# Appendix A

---

## Bootstrap algorithm for estimating standard deviations and correlation coefficients of estimated GEV parameters

The bootstrap is applied to the running and sliding annual maximum rainfalls. Because the sliding annual maxima are only available for De Bilt, the annual maxima from De Bilt and the other stations are sampled separately. The two bootstrap samples are then concatenated to form a bootstrap sample of 514 years with the same layout as the original sample of annual maximum rainfalls. This procedure is similar to the regional bootstrap in GREHYS (1996). A precise description of the bootstrap algorithm is presented below. Steps 3 and 4 are illustrated in Table A.1.

1. Split the annual maxima series of 514 years into a series of 84 years with year numbers 1, 2, ..., 84, belonging to De Bilt 1906-1990, and a series of 430 years with year numbers 85, 86, ..., 514.
2. Draw for each of the two series of year numbers a random sample with replacement (bootstrap sample).
3. Select the running annual maxima for the sampled year numbers for  $D = 1, 2, 4, 8, 12, 24$  h. This leads to one bootstrap sample of 84 years of running annual maxima and one bootstrap sample of 430 years of running annual maxima for each  $D$ . For  $D = 1, 2$  h also a bootstrap sample of 84 sliding annual maxima is constructed using the same year numbers as for the 84 running annual maxima.
4. Construct bootstrap samples of 514 years by adding the 84-year to the 430-year running annual maxima.

5. Fit a GEV distribution to the bootstrap sample of 514 years for each of the durations of 1, 2, 4, 8, 12 and 24 h.
6. Fit a GEV distribution to the bootstrap sample of 84 years for durations of 1 and 2 h individually. Do this separately for the bootstrap samples of running and sliding maxima.
7. Apply Eqs. (2.18)-(2.20) for  $D = 1, 2$  h.
8. Repeat this  $10^4$  times, so that  $10^4$  bootstrap samples are drawn and  $10^4$  GEV parameters are estimated for each duration.
9. Determine the standard deviation of each estimated GEV parameter as the sample standard deviation of that parameter estimate in the  $10^4$  bootstrap samples.
10. Determine the correlation between estimated GEV parameters by calculating the correlation between these parameter estimates in the  $10^4$  bootstrap samples.

**Table A.1:** Application of the bootstrap.

Year number	Running annual maximum (mm)	Sliding annual maximum (mm)	Drawn bootstrap samples
1	13.2	17.3	84 running and 84 sliding maxima De Bilt
2	9.2	9.2	
.	..	..	
84	9.1	10.0	
85	17.4	not available	430 running maxima 514 running maxima <sup>+</sup>
86	15.3	not available	
.	..	not available	
514	16.9	not available	

# Appendix B

---

## Maximum likelihood versus L-moments

A number of simulation experiments have been conducted by Sveinsson et al. (2001) to compare maximum likelihood estimation with L-moments methods under the index flood assumption. These experiments were restricted to a small number of sites. This appendix discusses a simulation experiment in which there are 200 sites, each having a record of only 11 annual maxima. It is assumed that the  $200 \times 11$  annual maxima are independent. The maxima are generated from a GEV distribution with  $\gamma = 0.245$  and  $\kappa = -0.170$ . The average  $\mu$  is 34.75 mm: for 160 sites a 5% smaller value and for 40 sites a 20% larger value of  $\mu$  is used in the simulation, which roughly corresponds to the regional differences of  $\mu$  for  $D = 24$  h in the Netherlands. The simulations are repeated 600 times.

Two L-moments methods and three maximum likelihood methods are considered. The first L-moments method is that used in the UK Flood Estimation Handbook (FEH) as described by Fowler and Kilsby (2003). For each site annual maxima are scaled with their median value and the L-moments ratios L-CV and L-SKEW are calculated. Subsequently, these L-moments ratios from the 200 sites are averaged and the GEV parameters are estimated from the average L-moments ratios and the at-site median. In the second L-moments method the average is used as the index flood instead of the median (Hosking and Wallis, 1997). The maximum likelihood procedure used in Chapter 4, in which the iteration is stopped after one step, is compared with two alternatives, the full maximization of the likelihood under the index flood assumption and the full maximization with only two regional location parameters. In the latter case one value of  $\mu$  is estimated for the 40 sites with a relatively large value of this parameter and one value for the other 160 sites.

For the five estimation procedures, Table B.1 shows the means of the estimated GEV parameters, and the resulting 50-year rainfall depth,  $\hat{x}(50)$ , in the 600 simulations. The estimates of the location parameter and the 50-year rainfall depth have been averaged over the 200 sites. The standard deviations of the estimated GEV parameters and  $\hat{x}(50)$  were also derived from

the 600 simulations.

The table shows that both L-moments methods result in a large bias of  $\hat{\kappa}$ . Though the standard errors of the L-moments estimates of  $\mu$ ,  $\gamma$  and  $\kappa$  are generally larger than those of the maximum likelihood estimates, this does not lead to a larger standard error of  $\hat{x}(50)$ . Something similar was also observed by Morrison and Smith (2002) who compared L-moments estimates with mixed maximum likelihood L-moments estimates. The one-step maximum likelihood procedure results in a somewhat larger bias in  $\hat{\gamma}$  than the L-moments methods, but there is no bias in  $\hat{\kappa}$ . The full maximum likelihood procedure under the index flood assumption does not provide better estimates. In particular, it leads to a considerable bias of  $\hat{\kappa}$  and an increase of the standard error of this parameter estimate. Obviously, the large uncertainty of the 200 at-site estimates of  $\mu$  deteriorates the quality of the estimate of the common  $\kappa$ . Similar results were obtained in the case of 500 sites. Full maximization with two regional values of  $\mu$  gives almost unbiased estimates of the common parameters. In this case the standard errors of the estimated location parameters are much smaller than those for the index flood method (not shown in Table B.1).

The bottom rows of Table B.1 give the results for a simulation experiment in which the number of annual maxima was increased to 50 per site. For this sample size the full maximum

**Table B.1:** Means and standard deviations (between brackets) of estimated GEV parameters and estimated 50-year rainfall depth  $\hat{x}(50)$  in two simulation experiments. FEH indicates the method used in the UK Flood Estimation Handbook and HW refers to the method employed in Hosking and Wallis (1997), and ML stands for maximum likelihood.

Method	$\hat{\mu}$ (mm)	$\hat{\gamma}$	$\hat{\kappa}$	$\hat{x}(50)$ (mm)
True values	34.75	0.245	-0.170	81.9
<i>Regional variability, 11 annual maxima</i>				
L-moments (FEH)	35.05 (0.24)	0.255 (0.005)	-0.113 (0.019)	78.7 (1.7)
L-moments (HW)	35.10 (0.22)	0.255 (0.005)	-0.113 (0.019)	78.8 (1.7)
ML, one step	35.31 (0.20)	0.260 (0.004)	-0.170 (0.017)	86.0 (2.1)
Full ML, index flood	34.84 (0.22)	0.228 (0.004)	-0.205 (0.025)	82.4 (2.3)
Full ML, regional $\mu$	34.77 (0.21)	0.245 (0.004)	-0.167 (0.017)	81.7 (1.8)
<i>Regional variability, 50 annual maxima</i>				
L-moments (FEH)	34.81 (0.11)	0.247 (0.002)	-0.156 (0.009)	81.1 (0.9)
L-moments (HW)	34.83 (0.10)	0.247 (0.002)	-0.156 (0.009)	81.1 (0.9)
ML, one step	35.01 (0.10)	0.260 (0.002)	-0.170 (0.008)	85.5 (1.0)
Full ML, index flood	34.78 (0.10)	0.242 (0.002)	-0.174 (0.008)	81.8 (0.9)
Full ML, regional $\mu$	34.75 (0.10)	0.245 (0.002)	-0.169 (0.008)	81.8 (0.9)

likelihood method under the index flood assumption performs well. In particular, the biases are smaller than in the case of L-moments estimation and the one-step maximum likelihood estimation. There is no longer a deteriorating effect of the estimated at-site location parameters on the estimates of the common dispersion coefficient and shape parameter.

Sveinsson et al. (2001) presented a number of alternative L-moments methods resulting in less bias of a large quantile of the distribution than the L-moments methods considered here, however, at the cost of an increase in the standard deviation of the estimated quantile.

The one-step maximum likelihood procedure breaks down if the regional differences in the location parameter are larger than in the Netherlands. A full maximization of the likelihood (with some regionalization of the location parameter in the case of very short records) is then needed, which is computationally more demanding.



# Appendix C

---

## Influence of missing data on estimated GEV parameters

As was noted in Section 4.4, the average radar data availability is approximately 90% in the period where most annual maxima occur. A part of the observed annual maximum rainfall depths will therefore be lower than the true annual maxima, which influences the parameters of the GEV distribution. This influence is quantified here theoretically for the case of a negative shape parameter  $\kappa$ .

The GEV distribution for annual maxima is related to the Generalized Pareto Distribution (GPD), which describes the distribution of the exceedances  $Y = X - u$  of a high threshold  $u$  in the associated peak-over-threshold model. The cumulative distribution of  $Y$  is given by:

$$H(y) = 1 - \left(1 - \frac{\kappa y}{\sigma}\right)^{1/\kappa} \text{ for } \kappa \neq 0. \quad (\text{C.1})$$

The number of exceedances of the threshold  $u$  in a year follows a Poisson distribution with mean  $\lambda(u)$ . The GEV parameters  $\mu$  and  $\alpha$  are related to  $\lambda(u)$  and the GPD parameters  $\sigma$  and  $\kappa$  (Buishand, 1989; Madsen et al., 1997b):

$$\mu = u + \sigma[1 - \lambda^{-\kappa}(u)]/\kappa \text{ for } \kappa \neq 0, \quad (\text{C.2})$$

$$\alpha = \sigma/\lambda^\kappa(u). \quad (\text{C.3})$$

The value of the GEV parameter  $\kappa$  is equal to the value of the GPD parameter  $\kappa$ . In case a fraction  $f$  of the exceedances is missing, the Poisson distribution still holds if the missing exceedances are randomly distributed in time. The average number of exceedances in a year then becomes  $\lambda^*(u) = (1 - f)\lambda(u)$ . Using this expression and Eq. (C.3), the new value of  $\alpha$  becomes:

$$\alpha^* = (1 - f)^{-\kappa}\alpha. \quad (\text{C.4})$$

Due to the change of  $\lambda(u)$ , Eq. (C.2) changes into

$$\mu^* = u + \sigma[1 - (1 - f)^{-\kappa} \lambda^{-\kappa}(u)]/\kappa \text{ for } \kappa \neq 0. \quad (\text{C.5})$$

Now, Eq. (C.2) is subtracted from Eq. (C.5), which results in:

$$\mu^* = \mu + \frac{\alpha}{\kappa}[1 - (1 - f)^{-\kappa}] \text{ for } \kappa \neq 0, \quad (\text{C.6})$$

using Eq. (C.3). The new value of the dispersion coefficient is given by:

$$\gamma^* = \frac{\alpha^*}{\mu^*} = \frac{(1 - f)^{-\kappa}}{1 + \gamma[1 - (1 - f)^{-\kappa}]/\kappa} \gamma \text{ for } \kappa \neq 0. \quad (\text{C.7})$$

Eqs. (C.6) and (C.7) are used to estimate the change in  $\mu$  and  $\gamma$  in case  $f = 0.1$ , which corresponds to a data availability of 90%. Note that the relative changes in these parameters only depend on  $\gamma$  and  $\kappa$ . For  $\gamma = 0.245$  and  $\kappa = -0.170$ , representative of annual maximum precipitation for  $D = 24$  h,  $\mu^*$  is 2.6% smaller than  $\mu$  and  $\gamma^*$  increases 0.8% with respect to  $\gamma$ . For  $D = 15$  min, realistic values of  $\gamma$  and  $\kappa$  are respectively 0.346 and -0.110 and  $\mu^*$  decreases 3.6% with respect to  $\mu$  and for  $\gamma^*$  an increase of 2.6% is found. This demonstrates that 10% missing data has little influence on the value of the estimated GEV parameters.



# List of Publications

## Peer-reviewed articles

- Van Vliet A.J.H., A. Overeem, R.S. De Groot, A.F.G. Jacobs, and F.T.M. Spijksma, 2002: The influence of temperature and climate change on the timing of pollen release in the Netherlands. *International Journal of Climatology*, **22**, 1757-1767, doi:10.1002/joc.820.
- Overeem, A., A. Buishand, and I. Holleman, 2008: Rainfall depth-duration-frequency curves and their uncertainties. *Journal of Hydrology*, **348**, 124-134, doi:10.1016/j.jhydrol.2007.09.044.
- Overeem, A., I. Holleman, and A. Buishand, 2009: Derivation of a 10-year radar-based climatology of rainfall. *Journal of Applied Meteorology and Climatology*, **48**, 1448-1463, doi:10.1175/2009JAMC1954.1.
- Overeem, A., A. Buishand and I. Holleman, 2009: Extreme rainfall analysis and estimation of depth-duration-frequency curves using weather radar. *Water Resources Research*, **45**, W10424, doi:10.1029/2009WR007869.
- Overeem, A., A. Buishand, I. Holleman, and R. Uijlenhoet, 2009: Extreme-value modeling of areal rainfall from weather radar. *Water Resources Research*, submitted.

## Popular scientific articles

- Overeem, A., A. J. H. van Vliet, and R. S. De Groot, 2003: Vervroeging van het hooikoortsseizoen in een warmer klimaat? *Meteorologica*, **12**(1), 18-23 (*in Dutch*).
- Overeem, A., I. Holleman, and A. Buishand, 2009: Neerslagklimatologie uit weerradar. *H<sub>2</sub>O*, **42**(8), 31-33 (*in Dutch*).

## Other publications

- Overeem, A., 2002: *Verification of clear-air turbulence forecasts*. Technical report TR-244, KNMI, De Bilt.
- Overeem, A., I. Holleman, and A. Buishand, 2008: A 10-year radar-based climatology of rainfall. *Fifth European Conference on Radar in Meteorology and Hydrology*, 30 June - 4 July 2008, Helsinki, Finland.



# Curriculum Vitae

Aart Overeem werd op 25 maart 1979 geboren te Utrecht. Het vwo-diploma behaalde hij in 1997 aan het Ichthus College te Veenendaal. Hierna begon hij aan de opleiding Bodem, Water en Atmosfeer aan de toenmalige Landbouwuniversiteit Wageningen. In november 2002 studeerde hij af in de specialisatie Meteorologie aan de Wageningen Universiteit. Na ruim een half jaar administratief uitzendwerk begon hij in september 2003 aan de Masteropleiding Hydrologie en Waterkwaliteit, specialisatie Hydrologie en Kwantitatief Waterbeheer, welke hij afrondde in juni 2005. Van september 2005 tot en met augustus 2009 werkte hij als onderzoeker in opleiding bij het Koninklijk Nederlands Meteorologisch Instituut (KNMI) in De Bilt bij de afdeling Weer Onderzoek. Sinds 1 oktober 2009 werkt hij als postdoc bij de Leerstoelgroep Hydrologie en Kwantitatief Waterbeheer van Wageningen Universiteit.

In het kader van dit promotieonderzoek werd het diploma van de SENSE onderzoekschool behaald, met als belangrijkste activiteiten:

- Writing in English for publication level B2/C1
- Programming in C - Master it Training
- NCR-days 2005, 3-4 November 2005, Zwijndrecht, The Netherlands (oral presentation)
- European Geosciences Union General Assembly, 16-20 April 2007, Vienna, Austria (oral presentation)
- Autumn Symposium, Buys Ballot Research School, 31 October - 2 November 2007, Dalfsen, The Netherlands (oral presentation)
- European Geosciences Union General Assembly, 20-24 April 2009, Vienna, Austria (oral presentation)

Daarnaast werden twee radarconferenties bezocht:

- Fourth European Conference on Radar in Meteorology and Hydrology, 18-22 September 2006, Barcelona, Spain
- Fifth European Conference on Radar in Meteorology and Hydrology, 30 June - 4 July 2008, Helsinki, Finland (poster presentation)

This research has been performed at the Royal Netherlands Meteorological Institute (KNMI). The Secretary of State of the Ministry of Transport, Public Works and Water Management is gratefully acknowledged for offering this PhD position on occasion of the 150-year jubilee of KNMI.

Financial support from Wageningen University and KNMI for printing this thesis is gratefully acknowledged.